

AD-A240 391



2

PHOTOREFLECTANCE AND  $H_2O$  ADSORPTION ON GaAs(100)

BY

WILLIAM FRANK BUECHTER

B.S., United States Military Academy, 1981

DTIC  
ELECTE  
SEP 12 1991  
S B D

THESIS

Submitted in partial fulfillment of the requirements  
for the degree of Master of Science in Chemical Engineering  
in the Graduate College of the  
University of Illinois at Urbana-Champaign, 1991

**DISTRIBUTION STATEMENT A**

Approved for public release;  
Distribution Unlimited

Urbana, Illinois

91-07945



PHOTOREFLECTANCE AND H<sub>2</sub>O ADSORPTION ON GaAs(100)

BY

WILLIAM FRANK BUECHTER

B.S., United States Military Academy, 1981

THESIS

Submitted in partial fulfillment of the requirements  
for the degree of Master of Science in Chemical Engineering  
in the Graduate College of the  
University of Illinois at Urbana-Champaign, 1991

Urbana, Illinois

## Acknowledgement

I would especially like to thank my advisor, Professor Edmond G. Seebauer, for his detailed technical assistance and overall professional guidance during the period of my thesis research.

Many thanks also to Mike Mendicino and Kurt Schultz, who often lended technical assistance, and greatly assisting in my basic understanding of surface sciences.

A word of gratitude goes to Kim Johnson for her computer assistance in helping this document look like a professional manuscript.

To my Mother-In-Law, Soledad Baquilod, thanks for assisting Ofelia and I, and for helping take care of our children.

Lastly, this acknowledgement would not be complete without a heartfelt and loving thanks to my adorable wife, Ofelia, and my four sons: Kevin, Kenneth, William Jr., and Christopher. I owe them a great debt of gratitude for their love, patience and understanding.



Statement A per telecon  
Maj. Jill Whisker /TAPC-OPB-D  
Alexandria, VA 22332-0411

NWW 9/10/91

Accession For	
NTIS GRA&I	<input checked="" type="checkbox"/>
DTIC TAB	<input type="checkbox"/>
Unannounced	<input type="checkbox"/>
Justification	
By <i>per telecon</i>	
Distribution/	
Availability Codes	
Dist	Avail and/or Special
<i>A-1</i>	

## Table of Contents

1. Introduction .....	1
2. Literature Review .....	4
2.1 Photorefectance applications .....	4
2.2 Photorefectance adsorption studies .....	8
2.3 Substrate surface preparation .....	10
3. Photorefectance Theory .....	12
3.1 Early photorefectance analysis .....	12
3.2 The physics of photorefectance .....	13
3.3 Importance of the dielectric function .....	20
3.4 Optics of photorefectance .....	22
3.5 Electric field effects on $\epsilon$ .....	23
3.5.1 Low field limit .....	27
3.5.2 Intermediate field range .....	28
3.6 Investigation of experimental results .....	31
3.6.1 Subsidiary oscillation determination .....	31
3.6.2 Three point technique .....	32
3.6.3 Least-squares fitting method .....	34
3.6.4 Doping level effects .....	34
3.6.5 Photorefectance adsorption measurements .....	35

<b>4. Experimental</b>	<b>37</b>
<b>5. Results and Discussion</b>	<b>51</b>
<b>5.1 PR sample characterization</b>	<b>51</b>
<b>5.1.1 PR on sample A</b>	<b>51</b>
<b>5.1.2 PR of sample B</b>	<b>54</b>
<b>5.1.3 PR of sample C</b>	<b>63</b>
<b>5.1.4 PR of sample D</b>	<b>81</b>
<b>5.2 Sample comparison</b>	<b>105</b>
<b>6. Conclusions</b>	<b>112</b>
<b>References</b>	<b>113</b>
<b>Appendix 1: Program 1 listing</b>	<b>117</b>
<b>Appendix 2: Program 2 listing</b>	<b>120</b>

# 1 Introduction

Compound semiconductors possess the essential characteristics for the next technologically advanced generation of the semiconductor industry. Gallium arsenide (GaAs) in particular demonstrates considerable promise in the development of twenty-first century ultrahigh-speed computers, microwave generation and optical transmission. The unique properties of GaAs in comparison to silicon, the current mainstay of the electronic industry, are its enhanced optical properties and considerably higher electron velocity, which provide intrinsically higher speeds, greater operating frequencies, lower power requirements, higher resistance to high-energy radiation and dramatic optoelectronic capabilities[1]. The enhanced performance of GaAs makes it an essential component for certain aspects of future commercial and military electronic systems. However, as with any new material, manufacturing technologies for compound semiconductors are still in their early stages of development. Consequently, equipment and processes suitable for low-cost, high-yield fabrication of GaAs devices is lacking. Essential to the startup of any mass production for GaAs components is the theoretical modeling, development of analysis techniques, and economical quality control procedures.

Several methods are being developed to manufacture thin films of GaAs, including molecular beam epitaxy (MBE), metal-organic chemical vapor deposition (MOCVD) and gas phase molecular beam epitaxy (GPMBE). All of these processes involve the heterogeneous reaction between a gas phase species and the growing surface. An

understanding of the surface chemistry, including adsorption, surface diffusion and desorption, is still in its infancy. Yet this understanding is vital to the fabrication of high technology devices[2]. For example, the adsorption of gases like  $O_2$ ,  $H_2O$ ,  $CO$ , etc. with a clean GaAs surface affects the surface state distribution[3]. With this focus, the adsorption processes involving  $H_2O$  on GaAs were the primary effort of the present work.

Modulation spectroscopy provides a valuable characterization tool for analyzing compound semiconductors. Numerous spectroscopies exist, but most have limitations. For example, electroreflectance requires either the physical attachment of metal electrodes to the surface or immersion of the sample in electrolyte. Such methods preclude the observation of important surface chemistry. Other surface characterization techniques such as photoluminescence and resonant Raman spectroscopies require measurement at cryogenic temperatures (typically 4.2K), while Hall and capacitance-voltage (C-V) measurements use electrical contacts. Infrared absorption requires that a window be etched through the sample substrate[4]. Photoreflectance (PR) alone has the unique ability to evaluate semiconductor properties both in situ and after processing[5].

The PR technique is contactless and nondestructive, and is easily performed at various temperatures and pressures. Only recently has the importance of PR been demonstrated with its sensitivity to adsorption-induced changes in the surface states at the gas-solid interface. This responsiveness to surface treatment makes PR one of the most valuable tools in the quantitative analysis of surface phenomena. As a result, the

technique of PR is ideally suited for the current studies.

In PR the surface reflectance is periodically perturbed by a light beam with a photon energy greater than the fundamental bandgap energy  $E_g$  of the sample substrate. In this manner, the built-in surface electric field is periodically modulated by the injection of electron-hole pairs[6]. The photogenerated minority carriers recombine with charge in the surface states, thereby reducing the surface potential. Sharp spectra are observed at energies corresponding to critical points in the bulk band structure. These energies are set by the fulfillment of the condition  $\nabla_k E_c - \nabla_k E_v = 0$ , where  $\nabla_k$  is the derivative operator with respect to the wave vector. Analysis of these spectra yield considerable insight into the electronic structure of the bulk semiconductor.

There are notable similarities between electroreflectance (ER) and PR. In fact, both result from the modulation of the surface electric field. As both ER and PR methods perturb the sample in a related manner, PR spectra can be conveniently interpreted using the theoretical basis already developed for ER.

In this thesis, PR has been used to characterize various procedures for cleaning GaAs surfaces. In addition, PR has been used to characterize some aspects of the kinetics and thermodynamics of  $H_2O$  adsorption of GaAs.  $H_2O$  adsorption was used as a model system for PR studies. This work is a prelude to studying the more complex adsorption systems associated with CVD and MBE.



## 2 Literature Review

### 2.1 Photoreflectance applications

Photoreflectance has been developed relatively recently as a diagnostic tool for the characterization of semiconductors. Wang et al.[6] first utilized basic PR about two decades ago in the quest to develop a nondestructive method to evaluate the energy band structure in solids. The PR method was employed by Shay[7] to study doping effects in the ultrapure epitaxial layers of GaAs. He found that the built-in surface electric field decreases as the doping decreases, and the PR lineshape narrows in qualitative agreement with Franz-Keldysh theory predictions[8]. Shay[7] was able to derive a more accurate value for the bandgap of GaAs due to a narrower lineshape than provided by other modulation techniques. Peters et al.[4] utilized PR to determine the doping level in GaAs. Very accurate PR spectra displayed shifts of the band edge in GaAs, which were correlated to Franz-Keldysh line shapes, thereby yielding the doping concentration. Bottka et al.[9] developed a relationship between the built-in surface potential and the energy period of the Franz-Keldysh oscillations (FKO) to determine carrier concentration. Both these studies were limited to higher carrier concentrations ( $3 \times 10^{15} - 8 \times 10^{17} \text{ cm}^{-3}$ ), so Sydor et al.[10] examined the PR properties in undoped and lightly doped samples. Additionally, unintentional impurity concentrations in undoped GaAs was studied. The lightly doped samples ( $5 \times 10^{15} \text{ cm}^{-3}$ ) produced greatly enhanced FKO peaks that made doping measurements more credible. Undoped MBE material displayed large PR

amplitude with and intercept  $E_g$  near 1.423 eV. Features at energies below 1.415 eV generally signified the presence of impurities. A further study was done by Sydor et al.[11] at varying temperatures on  $Al_xGa_{1-x}As$  coated semi-insulating material. They reported that doping concentration appeared insensitive to temperature changes between 200K and 400K.

The understanding of temperature effects on semiconductors during processing is important to ensure consistent, uniform growth. The position of the fundamental band gap energy  $E_g$ , in PR spectra, gives scientists a valuable method for calculating accurate sample temperatures[12]. Shay[7] noticed that as the temperature is decreased from room temperature to 77K, the spacing between adjacent energy peaks in the PR spectrum decreases by about a factor of two, indicating a decrease in the surface electric field. He explained this temperature dependence by a simple model for the surface consisting of a large density of electron traps located a fixed energy below the conduction band edge. As the temperature is lowered, the electron traps are raised higher above the Fermi level resulting in less charges trapped at equilibrium. This means the band bending lowers at lower temperatures. Nahory and Shay[13] confirmed the shift of the spectral lineshapes to lower energies at reduced temperatures as did Hamakawa et al.[14] using ER on Ge. These authors, however, suggested that the shift to lower energies was due to exciton effects. The reduction of line widths was also observed by Shen et al.[15] as they determined the direct gaps ( $E_g$ ) of GaAs from 77K to 600°C. Their ability to measure  $E_g$

at these high temperatures is crucial since it corresponds to the temperature of growth conditions for MBE, MOCVD, and other fabrication techniques.

The impact of the intensity of the pump beam on the sample yields insight as to the mechanism of PR. With one exception, Shay[7] determined that the intensity of the modulating beam did not affect the lineshape of the PR spectra, whereas the amplitude increased approximately as the cube root of the laser intensity. The purest sample ( $1.65 \times 10^{13} \text{ cm}^{-3}$ ) displayed both lineshape and amplitude changes for the highest laser intensity ( $0.1 \text{ W/cm}^2$ ). Nahory[13] further tested both n-type and p-type GaAs samples in the range of  $10^{15}$  to  $10^{16} \text{ cm}^{-3}$ . He determined lineshape was independent of laser intensity, and confirmed amplitudes varied approximately as the cube root of the laser intensity.

An interesting phenomena was reported by Sydor et al.[11] regarding temperature and epilayer thickness. At temperatures between 200K and 400K, the band-edge signal from thin GaAs epilayers contained a contribution from the epilayer-substrate interface. The interface effect was found to depend on doping, epilayer thickness, and carrier mobility. The effect broadened the band edge PR by 5-10 meV and artificially lowered estimates for  $E_g$ .

Polarization of the modulating beam was found by Cerdeira and Cardona[15] to cause amplitude variations in the PR spectra of silicon. A substantial increase in the intensity of the peaks was noticed when the external field was in a direction such that the band bending increased. This was the case at both 77K and room temperature. A Si(110)

sample displayed a larger PR spectra for incoming light polarized parallel to the (100) direction than for the (110) direction. At 77K the PR spectra splits into two components, one at 3.46 eV, and another at 3.37 eV. The larger peak reflected room temperature results, but the smaller peak displayed the opposite effect.

In recent years much emphasis has been placed on thin film technology for the fabrication of various microstructures. PR is utilized to examine multiple quantum wells (MQW), high-electron-mobility transistors (HEMT) composed of modulation-doped heterojunctions, etc.[16]. Examples of these structures are GaAs/AiGaAs superlattices[17], modulation-doped heterojunctions[18], InGaAs/GaAs strained superlattices[19], and GaAs quantum wells grown on Si[20]. Glembocki et al.[18] applied the PR method to characterize the interband transitions in GaAs/AiGaAs MQW and modulation-doped heterojunctions. The minority carrier lifetime was determined by Shen et al.[21] on GaAs doping superlattices. These are but a few examples of the ongoing work with superlattices.

Many other semiconductor materials are analyzed with PR. Amirtharaj et al.[22] characterized  $\text{Hg}_{1-x}\text{Cd}_x\text{Te}$ , the leading infrared detector material. It was noted that this material responds similarly to GaAs as the spectra narrows with decreasing temperature. Other work performed by Amirtharaj et al.[23] on  $\text{Hg}_{1-x}\text{Cd}_x\text{Te}$  and  $\text{Hg}_{1-y}\text{Zn}_y\text{Te}$  revealed a dependence of the spectral intensity on the modulation frequency. This dependence was explained by slow surface traps with characteristic time constants of the order of 1 ms.

Boron ion-implanted CdTe(100) was studied by Amirtharaj et al.[24] since it is the principal element used in electrooptic devices such as infrared detectors and solar cells. Ion damaged, partially recovered, and undamaged or fully recovered regions were identified using PR spectra, and the respective volume fraction of each phase was estimated. Studies of silicon films on sapphire (SOS) were performed by Giordana et al.[25] to measure strain in SOS films and crystalline quality of the silicon layer. SOS films have become prevalent recently for their use in three dimensional structures, and the short optical penetration depth of PR ( $100\text{\AA}$ ) allows investigation of these thin films. Pollak and Shen[26] recently used PR to measure the direct gap of InP up to  $600^\circ\text{C}$ , strains in Si at the  $\text{SiO}_2$  interface, changes in the surface fermi level of GaAs caused by photowashing as well as other superlattice effects.

## **2.2 Photoreflectance adsorption studies**

The sensitivity of PR to adsorption was first noticed by Wang et al.[6] when the effects of dry  $\text{O}_2$ , wet  $\text{O}_2$ , and air, adsorbed on CdS were observed. Significant differences in line shape and amplitude were noted but little attempt was made to explain the effects. Buchel and Luth[3] first used ultraviolet photoemission spectroscopy (UPS) to investigate the adsorption of water and methanol on GaAs. For  $\text{H}_2\text{O}$ , two molecularly adsorbed phases were distinguished at 300K. At low coverage,  $\text{H}_2\text{O}$  is chemisorbed by its oxygen lone-pair orbital to the surface, whereas for higher exposures, a less perturbed species which resembles a condensed  $\text{H}_2\text{O}$  layer was found. At 180K, only the less perturbed

species was found. Methanol was found to be chemisorbed molecularly at lower coverage with its oxygen end to the GaAs surface. For higher exposures, two additional emission bands were observed which were interpreted from a partial decomposition of  $\text{CH}_3\text{OH}$  into the methoxy radical  $\text{CH}_3\text{O}$ .

When compared to PR, UPS is quite complicated to perform. Also, since interactions between semiconductor surfaces and many gases are often quite weak or involve activated adsorption, relatively high ambient pressures ( $10^{-3}$  to  $10^3$  Torr) are necessary to produce significant surface coverage[27]. At these pressures, traditional electron or ion based spectroscopies such as UPS, low energy electron diffraction or Auger spectroscopy cannot be used. Other optical methods such as infrared spectroscopy and ellipsometry only reveal a limited quantity of surface characteristics. As a result, the importance of PR as a diagnostic tool for adsorption studies emerged.

The first use of PR for quantitative adsorption measurements was recently performed by Seebauer[28]. The adsorption of  $\text{CO}$ ,  $\text{O}_2$  and  $\text{H}_2\text{O}$  on GaAs(100) were used to validate the sensitivity of PR to adsorption despite a very weak interaction of  $\text{CO}$  with GaAs. Sticking coefficients ( $S$ ) were found at low coverage to increase in the order  $\text{CO} < \text{O}_2 < \text{H}_2\text{O}$ . Saturation caused  $S$  to decrease by at least four orders of magnitude. Additional studies were conducted by Seebauer[29] using the PR technique as a measure of surface treatment. The PR spectra of air-oxidized and annealed GaAs(100) were shown to be substantially different from those of the clean surface.

### 2.3 Substrate surface preparation

Surface cleaning of the semiconductor wafer prior to film growth is a critical first step in device technology. Numerous methods are being intensively studied to ensure the substrate surface is free of all carbon and oxygen contamination to allow proper epitaxial growth[30-42]. Any partial contamination of the substrate surface is known to adversely effect the electrical properties of the material and deteriorates the crystallinity of the epitaxial layer[30].

Cleaning the substrate surface is considerably more complicated than it first may appear, since carbon and oxygen contamination removal is normally not accomplished by the same method. For instance thermal cleaning by annealing to 600°C removes the oxygen oxide from the substrate, but carbon remains. Further annealing would cause dissociation of the substrate. The carbon can be removed by hydrogen molecular ( $H_2$ ) beam-irradiation, but the oxygen oxide remains. Ion bombardment cleans the contaminates, but usually damages the substrate surface beyond repair[37]. Chemical etching cleans the substrate but recontamination occurs before obtaining UHV. Further studies concluded a combination of the various techniques appears to yield the best results. A method developed by Massies et al.[32,34,35] and used by Seebauer[29] yielded a clean Ga-rich surface. Basically, the sample was degreased in trichloroethylene and then rinsed with acetone and methanol. Subsequently, a short acid etch was performed of  $H_2SO_4:H_2O_2:H_2O$ , followed by rinsing with deionized water and drying with

a stream of dry nitrogen. The sample was promptly installed in a UHV chamber. Annealing at UHV then removed the thin oxide that had been generated between the etching and bringing the sample to UHV. Another noteworthy method developed by Chang et al.[39] was conducted by etching the surface of the semiconductor materials by using a hydrogen plasma to form active hydrogen atoms. These reacted with the contaminants to form volatile hydride compounds, thereby cleaning the surface. The Ga/As concentration ratio at the surface was found to be nearly the same as air cleaved GaAs.



### 3 Photoreflectance Theory

#### 3.1 Early photoreflectance analysis

The first PR experiments conducted by Wang et. al[6] resulted in a flurry of activity to explain the physical mechanisms involved. They suggested that the built-in surface field, modulated by an intense light beam with energy greater than the band gap energy ( $h\nu \geq E_g$ ), resulted in the generation of electron-hole pairs, which served to lower the surface potential, thereby changing the sample reflectivity. Gay and Klauder[43] suggested that PR resulted from a change in the population of the conduction and valence bands (a Burstein effect). Still others attempted to explain PR through either thermal modulation[44], or the screening of excitons by free carriers[45]. The Burstein effect was quickly disproven by Nahory and Shay[13] due to the observed  $\Omega$  transitions in GaAs, which were impossible for the Burstein effect. Thermoreflectance effects were discounted by Shay[7] due to the noted decrease in band bending with decreasing temperature. At lower temperatures the lineshape narrowed, implying a decrease in the built-in electric field. This would be just the opposite of what thermal effects would have predicted. Exciton effects are believed to impact PR spectra given the proper conditions. Shay and Nahory[46] reported a two-hundredfold increase in the PR spectra when cooling GaAs from 77K to 2K, which along with lineshape changes, supports the idea of a bound exciton. In another experiment[13], their finding of lower energy values in the PR spectra of GaAs than expected by a band-to-band Franz-Keldysh effect, were reportedly due to

excitonic effects. Their results compared favorably with Hamakawa et. al[14] who also concluded that exciton effects helped explain the peak spacing in their data. Shay[7] and Vrehen[47] attributed peaks in their respective PR and ER data to free excitons. The electric field theory proposed by Wang et. al[6] was further supported by Aspnes[48] in his study of Ge, and by Cerdeira and Cardona[15] in their study on Si. Subsequent work by Aspnes to interpret PR and ER spectra in terms of Franz-Keldysh theory has put the quantitative physical description of the electric field effects on a sound theoretical basis. It is now accepted that PR is an electric field phenomenon, affected by excitons under the right conditions. The current studies have focused on minimizing excitonic effects by operating in moderate temperatures (100K - 525K), and by using high carrier concentrations. In the following section a more detailed description of the physics of PR is outlined.

### 3.2 The physics of photoreflectance

A beam of light incident on an interface with intensity  $I_0$  splits into three components. The incident light will be reflected, transmitted, or absorbed with intensities  $I$ ,  $I_1$ , and  $I_2$  respectively[49]. Following the law of energy conservation, the following relation holds:

$$I_0 = I + I_1 + I_2 \quad (1)$$

Of the three components, only the reflected light is pertinent to reflectance spectroscopy.

The ratio of the reflected light to the incident light yields the reflectance (R):

$$R = \frac{I}{I_o} \quad (2)$$

Reflectance is a function of the angle of incidence and polarization of the incoming light and of the refractive indices of the materials forming the interface. A typical spectrum for the GaAs-vacuum interface is shown in Figure 1(a). There is a doublet structure around 3eV and a large peak in the 5eV region. The potential for further analysis of the spectrum in terms of electronic structure is quite limited because of the very broad features. In general, reflectance spectra by themselves are unable to provide a complete picture of the band structures of semiconductors.

The lack of detail in R spectra resulted in the development of an optical characterization tool termed modulation spectroscopy. These methods elucidate much sharper structure at key "critical points" in a semiconductor's band structure. As an example, the band structure shown in Figure 2 depicts the main interband critical points of GaAs. In brief, these critical points occur where the bands are parallel in momentum space  $k$ , and their energies are determined by the spacing between the bands. Mathematically, a critical point is located where  $\nabla_k E_c - \nabla_k E_v = 0$ , where  $\nabla_k$  is the derivative operator with respect to the wave vector  $k$ . Critical points are generally labeled  $E_0$ ,  $E_0 + \Delta_0$ ,  $E_1$ , etc.  $E_0$  is the fundamental band gap energy required to achieve a transition from the valence band to the conduction band. In GaAs  $E_0 = E_g$  (since direct transitions are allowed), which accounts for one of its superior capabilities over nondirect

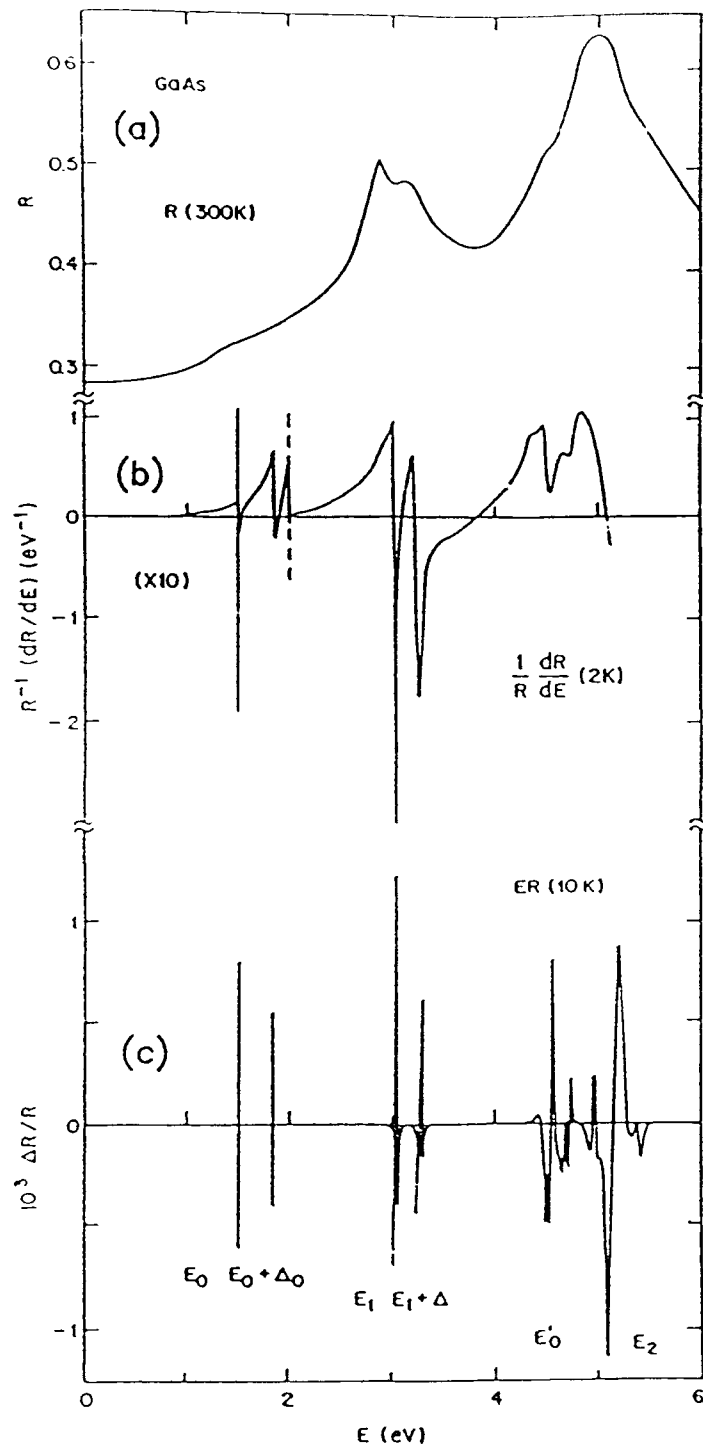


Figure 1. A comparison of three types of GaAs spectra: (a) reflectance  $R$ ; (b) energy-derivative reflectance; (c) low-field electroreflectance (Ref. [50]).

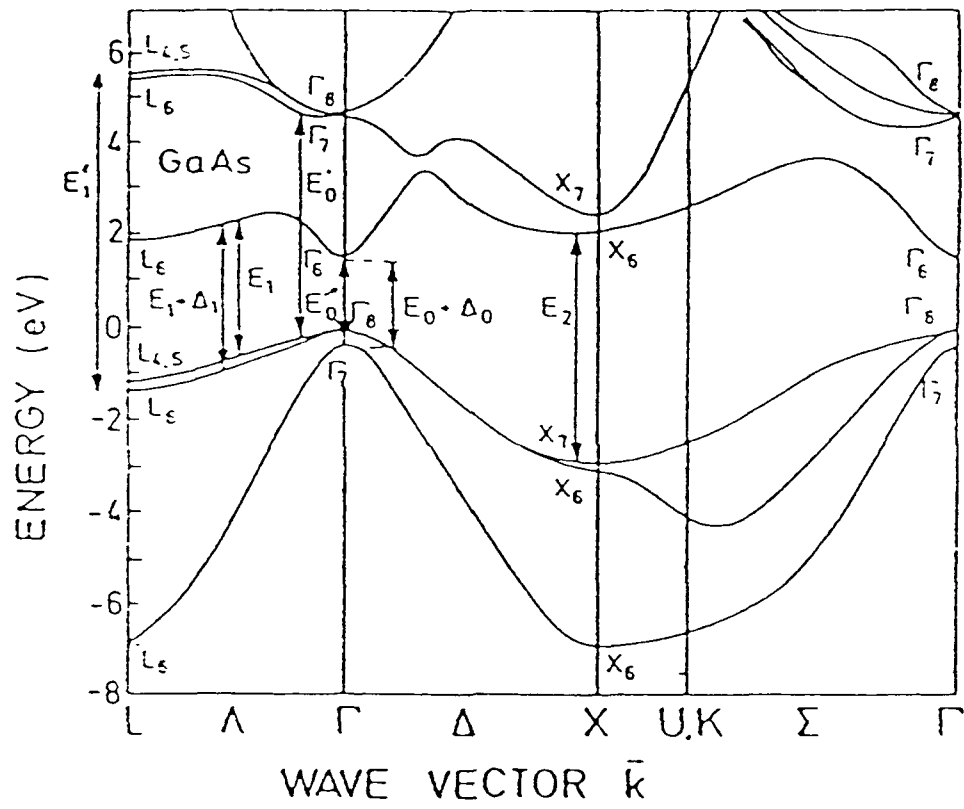


Figure 2. Band structure of GaAs showing the main critical points (Ref. [51]).

semiconductors such as silicon. Modulation spectra display sharp, well-defined peaks at the critical points.

Modulation spectroscopy encompasses a variety of techniques, the purpose of which is to obtain highly structured spectra that can be readily analyzed to determine the material properties being studied. In essence, modulation spectroscopy suppresses uninteresting background effects and emphasizes optical features near critical points, thereby resolving structure that would be weak in ordinary reflectance spectra. Several modulation techniques exist, such as thermoreflectance, piezoreflectance, electroreflectance, and photoreflectance. Each of these methods perturbs or modifies some parameter of a material, in order to produce a change in optical reflectance or transmittance of the sample. For example, thermoreflectance uses a heat pulse, piezoreflectance applies a uniaxial stress, while both electroreflectance (ER) and photoreflectance (PR) change the electric field,  $\xi$ . Figure 1(c) illustrates ER spectra and shows the sharp differential-like spectra where the critical points occur. The fundamental band edge ( $E_0$ ), which corresponds to a direct transition at the center of the Brillouin zone, only appears as a weak shoulder in the R spectra, and the spin-orbit split component ( $E_0 + \Delta_0$ ) is missing completely, yet very distinct values are shown in the ER spectra. The doublet in the R spectra is well resolved and the large peak displays a distinct set of structures in the ER spectra.

Electromodulation is the most widely used modulation spectroscopy since it yields

the sharpest structures. An example of this can be seen in Figure 1 where an energy-derivative reflectance spectra (b) is shown compared to an ER spectra (c). Both ER and PR are electromodulation methods since they arise from modulation of the surface electric field. Though PR is slightly less sensitive than ER, its contactless and nondestructive nature far outweighs the benefits of ER for studies of adsorption.

In PR, the surface electric field is modified by a low-power light source (usually a laser) that is separate from the probe beam monitoring the reflectance. Figure 3 displays physically what transpires when the sample is illuminated by the pumping laser. In Figure 3(a), the laser injects electron-hole pairs near the surface potential. A corresponding decrease in electric field occurs as is shown in Figure 3(b). The change in surface potential in turn results in a change in reflectance. The change in reflected light will correspond to the difference of the two reflected light values,

$$\Delta I = I(\text{laser on}) - I(\text{laser off}) \quad (3)$$

Substituting equation (2) into equation (3) yields:

$$\begin{aligned} \Delta I &= I_o(R(\text{laser on}) - R(\text{laser off})) \\ &= I_o \Delta R \end{aligned} \quad (4)$$

It is now important to normalize the change in reflectance ( $\Delta R$ ), as this will automatically correct for any fluctuations in the reflected intensity due to either changes in the incident light intensity or variations on the sample surface. It follows that:

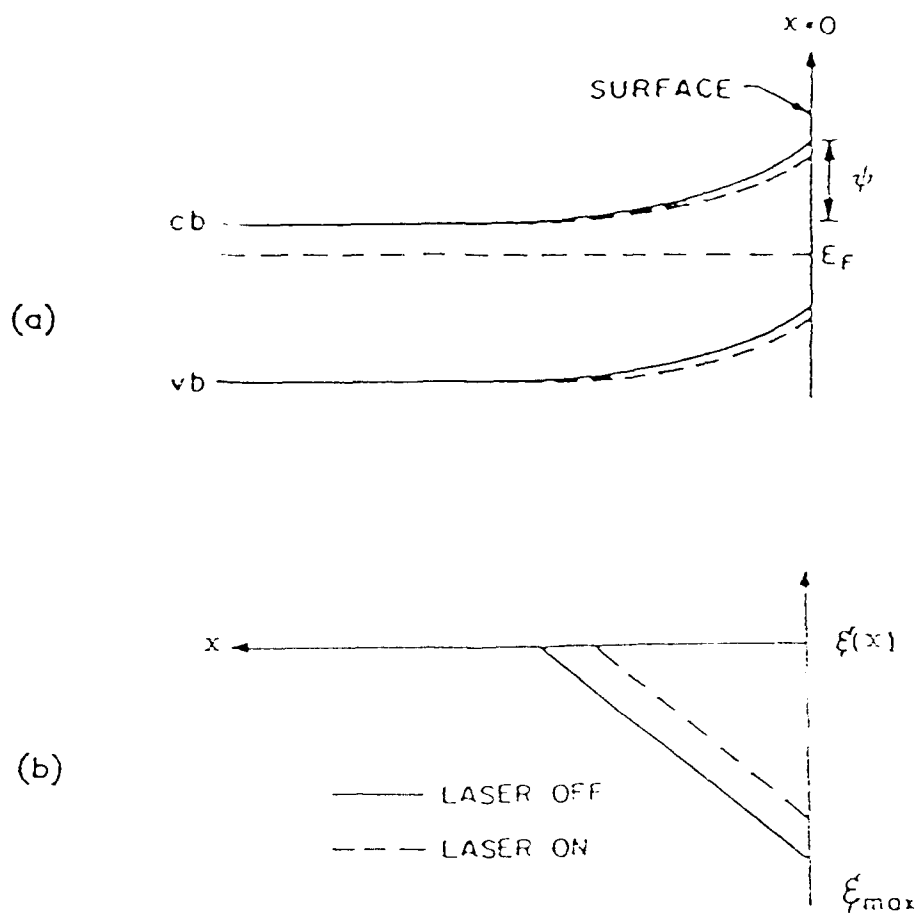


Figure 3. Depiction of the energy band (a), and the electric field (b), in the space charge region at a semiconductor surface when the laser is either off or on (Ref. [7]).



$$\frac{\Delta R}{R} = \frac{\Delta I}{I(laser\ off)} \quad (5)$$

This is the most useful quantity in determining semiconductor characteristics, however; due to its very small value ( $10^{-4}$  -  $10^{-6}$ ), phase sensitive detection must be employed. Normally a lock-in amplifier serves this purpose.

### 3.3 Importance of the dielectric function

Modulation spectroscopy uses a perturbation to change the dielectric properties of the unperturbed solid. In electromodulation the perturbed electric field accomplishes this. Of fundamental importance, is that unlike other forms of modulation spectroscopy, the perturbed electric field becomes nonlattice-periodic. In other words, the change in electric field destroys the translational invariance of the crystal. The one-electron Bloch functions of the unperturbed crystal become mixed[52]. Normally momentum is a good quantum number to within a reciprocal lattice vector and optical transitions will remain vertical as is shown with piezoreflectance in the upper part of Figure 4. The shifts in energy gaps or amplitudes are generally small, and the perturbation induced changes in the dielectric function  $\epsilon$  are of first order and approximated by first order lineshapes. In the case of PR where translational invariance is lost, the electron accelerates and momentum is no longer a good quantum number in the field direction. The sharp vertical transitions are spread out over a finite range of initial and final momenta as shown in the bottom of Figure 4. The mixed Bloch functions of the crystal then smear out structure in the unper-

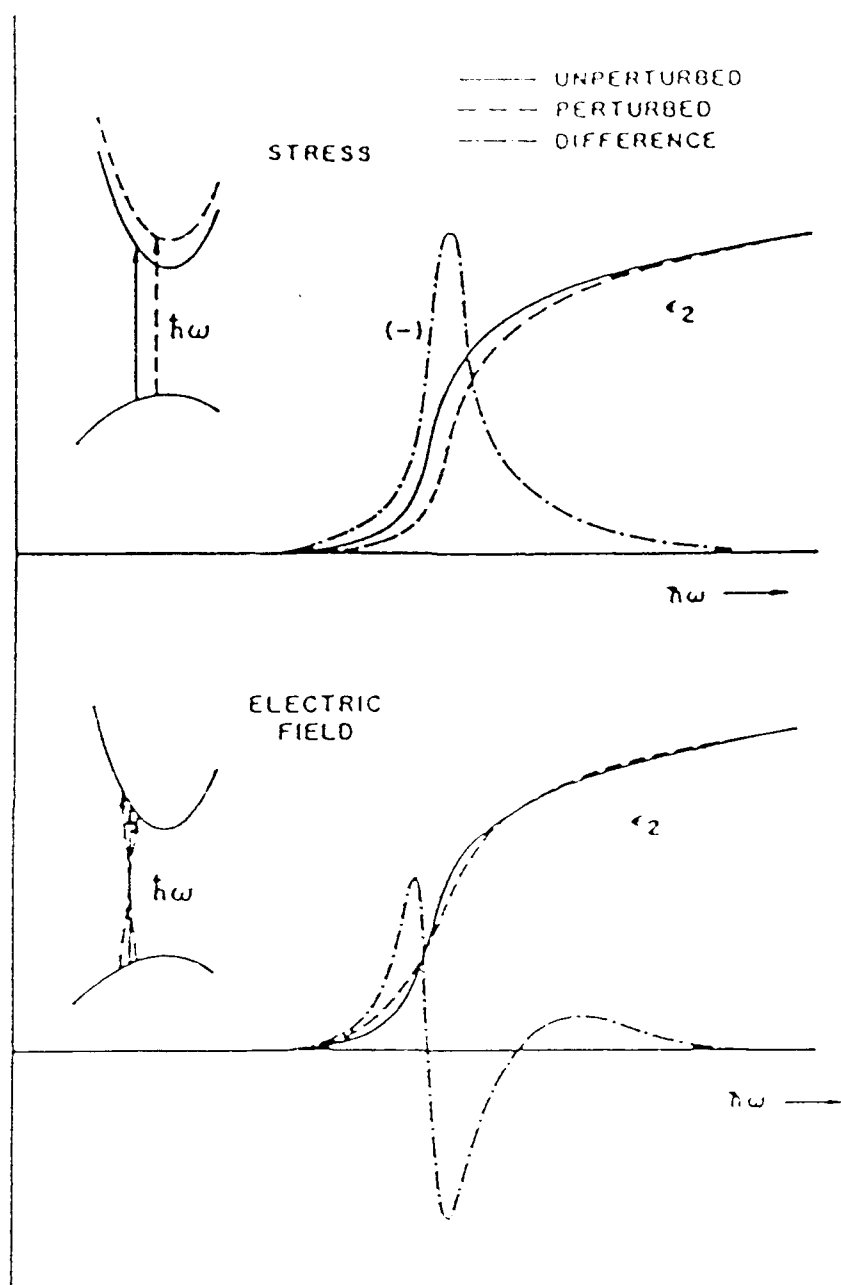


Figure 4. Schematic diagrams of: top, the first-derivative modulation process (prezoreflectance) where optical transitions remain vertical (inset) and the lattice periodicity is preserved; bottom, the third-derivative modulation process (PR) where optical transitions spread out (inset) and lattice periodicity is not preserved (Ref. [52]).

turbed dielectric function resulting in a complicated difference spectrum with changes in sign. This difference can only be approximated by the third derivative of the unperturbed dielectric function.

### 3.4 Optics of photoreflectance

Photoreflectance externally modulates the surface electric field of the material being analyzed. To properly interpret the externally modulated spectra, a link must be made between the optical parameters of the material and the observed experimental quantities. The optical response of the material is described by the complex dielectric function[50],

$$\epsilon(\omega) = \epsilon_1(\omega) + i\epsilon_2(\omega) \quad (6)$$

By assuming cubic symmetry,  $\epsilon(\omega)$  is a scalar. Furthermore, equation (5) must be expressed in terms of  $\Delta\epsilon(\omega)$ , the perturbation induced change in  $\epsilon(\omega)$ , to connect experiment and theory. For a two-phase (substrate-ambient) system with normally incident light on the surface, the Fresnel reflectance expression is

$$R = \left| \frac{n - n_a}{n + n_a} \right|^2 \quad (7)$$

$$n^2 = \epsilon, \quad n_a^2 = \epsilon_a \quad (8)$$

where  $n_a$  is the (real) refractive index of the ambient. Differentiation of equation (7) yields,

$$\frac{\Delta R}{R} = Re \left[ \frac{2n_a}{n(\epsilon - \epsilon_a)} \Delta\epsilon \right]$$

$$\begin{aligned}
&= \text{Re} [(\alpha - i\beta) \Delta\epsilon] \\
&= \alpha\Delta\epsilon_1 + \beta\Delta\epsilon_2
\end{aligned} \tag{9}$$

where  $\Delta\epsilon = \Delta\epsilon_1 + i\Delta\epsilon_2$  is the perturbation-induced change in  $\epsilon$ , and  $\alpha$  and  $\beta$  are Seraphin coefficients, which are functions of  $\epsilon_1$  and  $\epsilon_2$ [53]. A normalized change in reflectivity as measured in PR is now related to no more than the calculation of the change in the dielectric constant due to the perturbation. This  $\epsilon$  calculation will in turn reveal the characteristic PR lineshape.

### 3.5 Electric field effects on $\epsilon$

There are several parameters affecting the calculation of  $\epsilon$ . When an electric field is applied to a semiconductor, the resulting characteristic energy of a charged particle of mass  $\mu$  is[52]

$$\hbar\Omega = \left( \frac{e^2 \xi^2 \hbar^2}{8\mu} \right)^{1/3} \tag{10}$$

where  $\xi$  is the electric field strength,  $\hbar$  is Planck's constant divided by  $2\pi$ , and  $\mu$  is the interband reduced mass at the critical point in the Brillouin zone. This characteristic energy can fall into three ranges depending on whether the electric field is high, intermediate and low, as summarized in Table 1 below. The high field limit correlates to the breakdown of selection rules and Stark shifts of energy bands. It applies when the potential drop across the unit cell,  $e\xi a_0$ , is comparable to the bandgap energy  $E_g$ . Since most modulation techniques only slightly modify the surface electric field, the high field

limit is normally not achieved.

Table 1: Definition and experimentally identifying characteristics of the three ranges of ER spectra. (Taken from Ref. [52].)

	Perturbation energy	system energy
Range	Intraband	Interband
High	$\hbar\Omega \geq \Gamma$	$e\xi a_o \sim E_g$
Intermediate		$e\xi a_o \ll E_g$
Low	$\hbar\Omega \leq \Gamma/3$	

At lower fields it is useful to compare the perturbation energy  $\hbar\Omega$ , to the characteristic system parameter  $\Gamma$  which is the energy broadening parameter due to lifetime-induced uncertainty in the perturbed levels. Perturbation theory applies to this quantum mechanical system whenever the natural lifetime-induced uncertainty in the perturbed energy levels is large compared to the average energy gained per particle by acceleration in the field, i.e.  $\Gamma \gg \hbar\Omega$ . This inequality holds under low field conditions. At somewhat higher (intermediate) fields, the acceleration dominates the broadening, and perturbation theory no longer applies. A more complete quantum mechanical approach characterized by Franz-Keldysh oscillations and Airy functions is required.

A general expression for the dielectric constant in the one-electron approximation for a semiconductor can now be developed. The expression described by Bloch states

$\Psi_n(\mathbf{k}, \mathbf{r})$  with energy  $E_n(\mathbf{k})$  of band index  $n$  and wave vector  $\mathbf{k}$  is[50]

$$\varepsilon(E, \Gamma) = 1 + \frac{4\pi e^2 \hbar^2}{m^2 E^2} \sum_{\mathbf{k}, c, v} |\hat{\mathbf{e}} \cdot \mathbf{P}_{cv}(\mathbf{k})|^2 \left[ \frac{1}{E_{cv}(\mathbf{k}) - E - i\Gamma} + \frac{1}{E_{cv}(\mathbf{k}) + E + i\Gamma} \right] \quad (11)$$

where  $n = c, v$  denotes conduction (empty) and valence (filled) bands, respectively,  $\hat{\mathbf{e}}$  is the unit polarization vector and  $\mathbf{P}_{cv}(\mathbf{k})$  is the momentum matrix element. The interband energy is:

$$E_{cv}(\mathbf{k}) = E_c(\mathbf{k}) - E_v(\mathbf{k}) \quad (12)$$

and  $\Gamma$  is the phenomenological broadening parameter[50].

Equation (11) can be correlated to optical spectra by first converting the sum over  $\mathbf{k}$  into an integral:

$$\varepsilon(E, \Gamma) = 1 + \frac{e^2 \hbar^2}{\pi^2 m^2 E^2} \int_{BZ} d^3K |\hat{\mathbf{e}} \cdot \mathbf{P}_{cv}(\mathbf{k})|^2 \times \left[ \frac{1}{E_{cv}(\mathbf{k}) - E - i\Gamma} + \frac{1}{E_{cv}(\mathbf{k}) + E + i\Gamma} \right] \quad (13)$$

Then replace the independent integration variables by the energy  $E$ , and two variables  $k_1$  and  $k_2$  that locate a point on the constant-energy surface ( $s$ ) defined by  $E_{cv}(\mathbf{k}) = E$ . Because the Jacobian of the transformation is  $|\nabla E_{cv}(\mathbf{k})|_E^{-1}$ , the following expression can be obtained:

$$\begin{aligned} \epsilon(E, \Gamma) = 1 + \frac{e^2 \hbar^2}{\pi^2 m^2 E^2} \int dE \int_S dk_1 dk_2 \frac{|\hat{e} \cdot \mathbf{P}_{cv}(\mathbf{k})|^2}{|\nabla E_{cv}(\mathbf{k})|} \\ \times \left[ \frac{1}{E_{cv}(\mathbf{k}) - E - i\Gamma} + \frac{1}{E_{cv}(\mathbf{k}) + E + i\Gamma} \right] \end{aligned} \quad (14)$$

This expression shows that for a given band pair, "c,v" for which  $\nabla_{\mathbf{k}} E_{cv}(\mathbf{k}) = 0$ , there is a singularity at every  $\mathbf{k}$ . This is of extreme importance in modulation spectroscopy since the regions around these points lead to the structure in modulation spectra.

A fundamental derivation based on Bloch wavefunctions with only a single band pair of conduction (c) and valence (v) bands can be written[50]

$$\begin{aligned} \epsilon(E) = \frac{ie^2 \hbar^2}{\pi^2 m^2 E^2} \int_{BZ} d^3k |\hat{e} \cdot \mathbf{P}_{cv}(\mathbf{k})|^2 \\ \times \int_0^\infty dt \exp(-i[\omega_{cv}(\mathbf{k}) - \omega]t) \exp(-\Gamma t) \end{aligned} \quad (15)$$

where  $\hbar\omega = E$  and  $\hbar\omega_{cv}(\mathbf{k}) = E_{cv}(\mathbf{k})$ . Equation (15) is equivalent to the resonant term in equation (11) integrated over the first Brillouin zone.

To generate an expression of the form required in equation (9), the change in dielectric function  $\Delta\epsilon$  is needed. By applying an electric field below the high field limit and assuming the energy bands are simply parabolic, the field induced change in dielectric function can be calculated by[54]

$$\Delta\epsilon(E, \xi, \Gamma) = \epsilon(E, \xi, \Gamma) - \epsilon(E)$$

$$= \frac{ie^2\hbar^2}{\pi^2 m^2 E^2} \int_{BZ} d^3k |\hat{e} \cdot P_{cv}(k)|^2 \times \int_0^\infty dt \exp(-i[\omega_{cv}(k) - \omega - i\Gamma]t) \exp\left(-\frac{i\Omega^3 t^3}{3} - 1\right) \quad (16)$$

In photorefectance, only the low and intermediate field ranges apply. Separate expressions are developed for  $\Delta\epsilon$  in each case.

### 3.5.1 Low field limit

If a sufficiently small field is applied, the condition  $\hbar\Omega < \Gamma/3$  exists and

$$\exp\left(-i\frac{\Omega^3 t^3}{3}\right) \approx 1 - i\frac{\Omega^3}{3}t^3 \quad (17)$$

with the higher terms deleted. Substitution into equation (16) yields[52]

$$\Delta\epsilon = \frac{e^2\hbar^2}{3\pi^2 m^2 E^2} \int_{BZ} d^3k |\hat{e} \cdot P_{cv}(k)|^2 \Omega^3 \int_0^\infty dt t^3 \exp(-i[\omega_{cv}(k) - \omega - i\Gamma]t) \quad (18)$$

The third derivative relationship between the unperturbed dielectric function  $\epsilon$  and the field induced change  $\Delta\epsilon$  can be derived by substituting in equation (15). The result is:

$$\Delta\epsilon = \frac{(\hbar\Omega)^3}{3E^2} \frac{\partial^3}{\partial E^3} [E^2\epsilon(E)] \quad (19)$$

It is interesting to note that this expression quantitatively accounts for the loss of translational invariance discussed earlier. Furthermore, one sees that  $\Delta\epsilon$  is proportional



to the square of the electric field since  $\Delta\epsilon \sim (\hbar\Omega)^3 \sim \xi^2$ . Aspnes[55] takes this information and derives the lineshape for PR in the low field limit

$$\frac{\Delta R}{R} = \text{Re}[C e^{i\delta} (E - E_g + i\Gamma)^{-n}] \quad (20)$$

### 3.5.2 Intermediate field range

In the intermediate field case  $\Delta\epsilon$  is proportional to products of Airy functions and their derivatives. Equation (15) is reduced to the Airy convolution integral[8],

$$\begin{aligned} \Delta\epsilon(E, \xi, \Gamma) = & \frac{e^2 \hbar^2}{\pi m^2 (E + i\Gamma)^2} \left( \int_{BZ} d^3 k |\hat{e} \cdot \mathbf{P}_{cv}(k)|^2 \left[ \frac{1}{\hbar\Omega} \text{Gi}\left(\frac{E_{cv} - E - i\Gamma}{\hbar\Omega}\right) \right. \right. \\ & \left. \left. + \frac{i}{|\hbar\Omega|} \text{Ai}\left(\frac{E_{cv} - E - i\Gamma}{\hbar\Omega}\right) - \frac{1}{E_{cv} - E - i\Gamma} \right] \right) \end{aligned} \quad (21)$$

The  $\text{Ai}(x)$  and  $\text{Gi}(x)$  represent Airy functions of complex argument given by[56]

$$\text{Ai}(x) = \frac{1}{\pi} \int_0^\infty ds \cos\left(\frac{1}{3}s^3 + xs\right) \quad (22)$$

$$\text{Gi}(x) = \frac{1}{\pi} \int_0^\infty ds \sin\left(\frac{1}{3}s^3 + xs\right) \quad (23)$$

Airy's equation

$$\frac{d^2 \text{Ai}(x)}{dx^2} = x \text{Ai}(x) \quad (24)$$

has  $\text{Ai}(x)$  as the convergent solution and  $\text{Bi}(x)$  as a linearly independent divergent

solution. This form is not practical since Airy functions of complex argument must be computed numerically. The electrooptic functions  $F(\eta)$  and  $G(\eta)$  are therefore related to  $Ai(\eta)$  and  $Bi(\eta)$  by the expressions[50]

$$F(\eta) = \pi [(Ai'(\eta))^2 - \eta Ai^2(\eta)] - \sqrt{-\eta} u(-\eta) \quad (25)$$

$$G(\eta) = \pi [Ai'(\eta)Bi'(\eta) - \eta Ai(\eta)Bi(\eta)] + \sqrt{\eta} u(\eta) \quad (26)$$

The field induced change then becomes

$$\Delta\epsilon(E, \xi, \Gamma) = \frac{2e^2\hbar^2|\hat{e} \cdot \mathbf{P}_{cv}|^2}{m^2E^2} \left( \frac{2\mu}{\hbar^2} \right)^{3/2} (\hbar\theta)^{1/2} [G(\eta) + iF(\eta)] \quad (27)$$

where  $\eta = (E_g - E)/\hbar\theta$ ,  $u(n)$  is the unit step function, and

$$(\hbar\theta)^3 = e^2\xi^2\hbar^2/2\mu \quad (28)$$

This expression is related to equation (10) by:

$$(\hbar\theta)^3 = 4(\hbar\Omega)^3 \quad (29)$$

The Franz-Keldysh lineshapes  $F$  and  $G$  are plotted in Figure 5 at the fundamental band edge  $M_0$ . Once the threshold is exceeded, characteristic Franz-Keldysh oscillations appear. These expressions are related to PR spectra by[8],

$$\frac{\Delta R}{R} \sim (E - E_g)^{-\frac{(D+1)}{4}} \exp\left[-\frac{\Gamma(E - E_g)^{1/2}}{(\hbar\Omega)^{3/2}}\right] \cos\left[\frac{2}{3} \left(\frac{E - E_g}{\hbar\Omega}\right)^{3/2} - \frac{\pi}{4} (D - 1)\right] \quad (30)$$

where  $d$  is the dimensionality of the critical point.

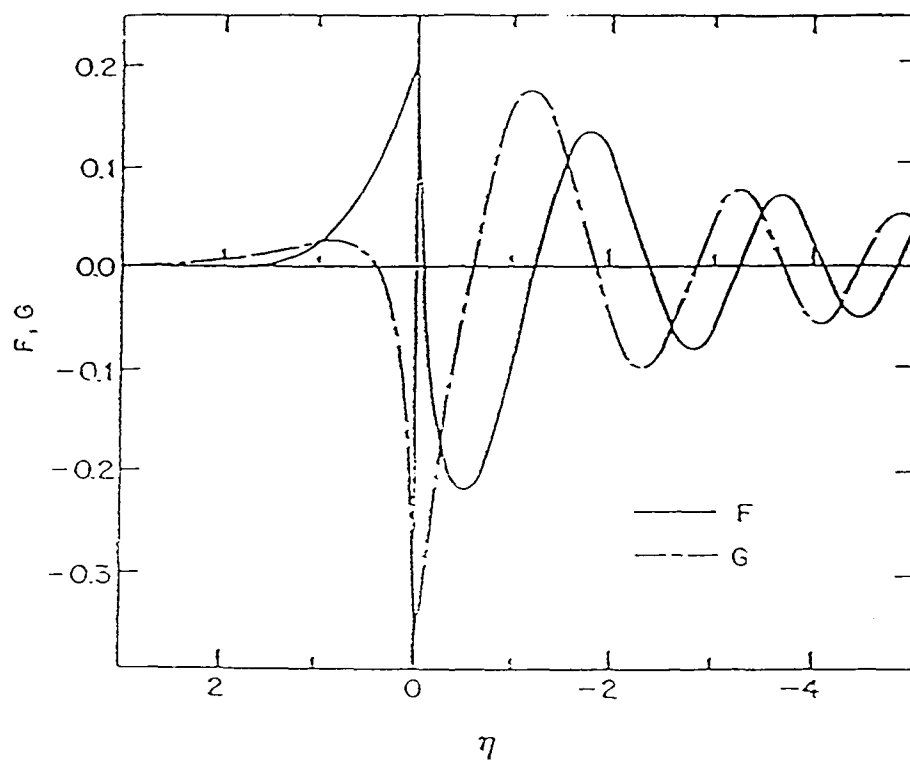


Figure 5. The Franz-Keldysh lineshapes F and G plotted with the x-axis reversed to simulate electric field modulation of  $\epsilon$  for an  $M_0$  critical point plotted against increasing energy (Ref. [50]).

## 3.6 Investigation of experimental results

### 3.6.1 Subsidiary oscillation determination

Modulation spectroscopy yields increased resolution of spectra, which enables subsidiary oscillations to be calculated accurately. Most importantly, it allows the calculation of the absolute magnitude of the electric field  $\xi$ , from the spacing of the Franz-Keldysh oscillations. In addition, the surface electric field  $\xi_s$ , and the broadening parameter  $\Gamma$ , can be derived. Aspnes and Studna[8] used the following equation to analyze their spectra:

$$\frac{\Delta R}{R} \approx (E - E_g)^{-1} \exp\left(-\frac{\Gamma(E - E_g)^{1/2}}{(\hbar\Omega)^{3/2}}\right) \cos\left[\delta + \frac{2}{3} \left(\frac{E - E_g}{\hbar\Omega}\right)^{3/2}\right] \quad (31)$$

where  $\delta$  is a phase factor. A summary of their method of determining  $\xi_s$  and  $\Gamma$  follows. If  $(\Delta R/R)_v$  and  $E_v$  represent the amplitude and energy position of the  $v^{\text{th}}$  extremum of the sequence of subsidiary oscillation, then it can be written:

$$v\pi = \delta + \frac{2}{3} \left[ \frac{(E - E_g)_v}{\hbar\Omega} \right]^{3/2} \quad (32)$$

Now the phase factor  $\delta$  and the characteristic energy  $\hbar\Omega$  can be obtained from the intercept and slope respectively, of a plot of  $(E - E_g)_v^{3/2}$  versus  $v$ . The resulting value of  $E$  is related to  $\xi_s$  by equation (10). By assuming a reduced mass, the surface electric field can be calculated. Through the attenuation of the peak amplitudes, a second condition is obtained. From equation (31),

$$\ln[(E - E_g)_v(\Delta R/R)_v] = - \frac{\Gamma[(E - E_g)^{1/2}]_v}{(\hbar\Omega)^{3/2}} \quad (33)$$

A relationship between  $\Gamma$  and  $\Omega$  can be generated from a plot of  $\ln[(E - E_g)_v(\Delta R/R)_v]$  vs  $[(E - E_g)^{1/2}]$ . The straight line slope then yields  $\Gamma$ .

### 3.6.2 Three point technique

The three point method is outlined by Aspnes and Rowe[57] in a simple manner with which to relate experimental data to theoretical lineshapes when working in low field regimes. It can be used when the spectra lineshape is relatively well isolated, exhibits at least one maximum and minimum peak and the Seraphin coefficients vary slowly over the central region extrema. The three points involved are the lower and higher extrema, A and B respectively, and the baseline, which is normally set at zero ( $\Delta R/R = 0$ ). Two values are used from each extremum, the energies  $E_A$  and  $E_B$ , and the reflectance values  $(\Delta R/R)_A$  and  $(\Delta R/R)_B$ . Since  $E_g$  is always at or between the two extrema, we can develop an equation for  $E_g$ ,  $\Gamma$  and a new parameter  $\rho$ [57].

$$E_g = E_A + (E_B - E_A)f(\rho) \quad (34)$$

$$\Gamma = (E_B - E_A)g(\rho) \quad (35)$$

$$\rho = -(\Delta R/R)_B/(\Delta R/R)_A > 0 \quad (36)$$

Figure 6 relates each of these parameters in graphical form including  $f(\rho)$  and  $g(\rho)$ , which in turn allows calculation of  $E_g$  and  $\Gamma$ . This technique is usually employed in the com-

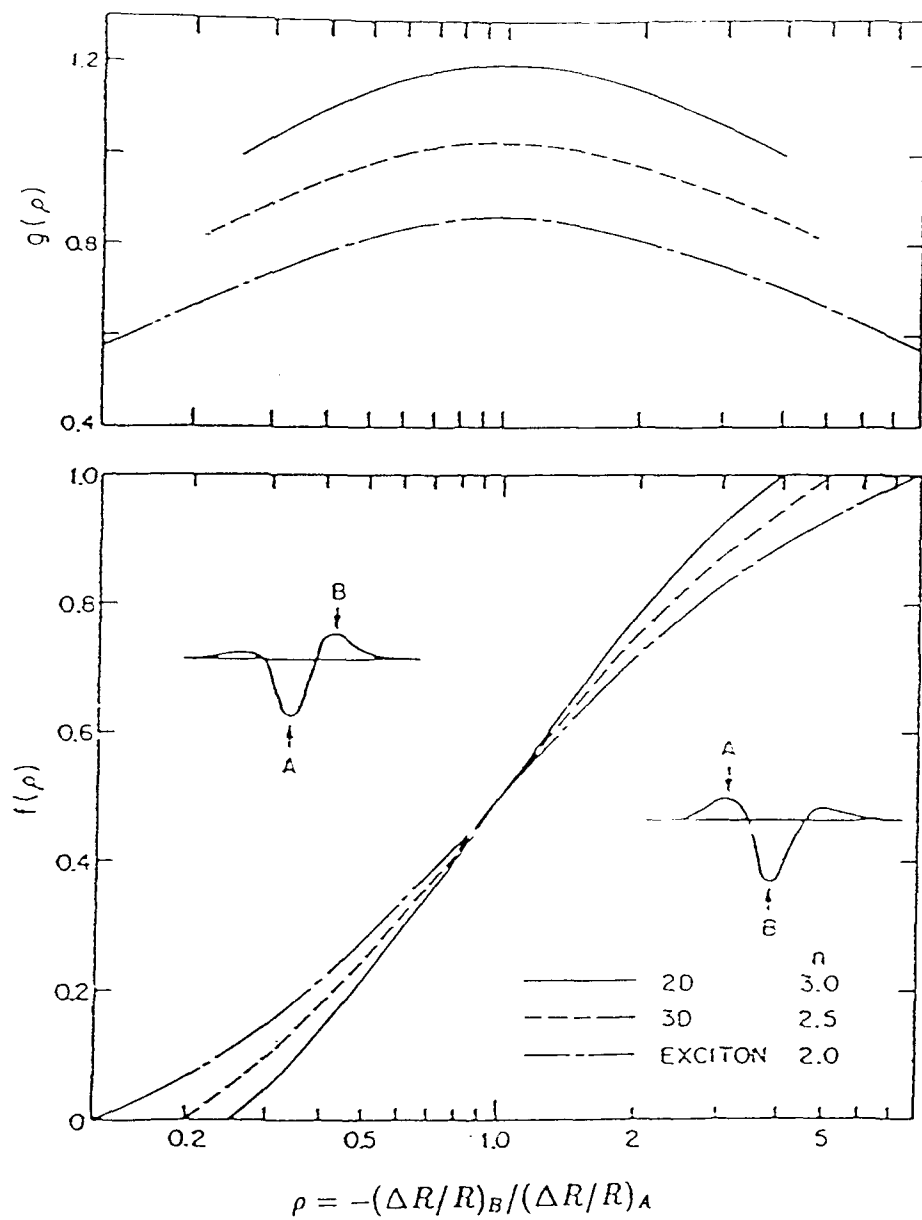


Figure 6. A graphical depiction of the functions  $f(\rho)$  and  $g(\rho)$  used in determining  $E_f$  and  $\Gamma$  (Ref. [57]).

positional analysis of new alloys. It works well because it is independent of phase and amplitude, however; since it is basically curve fitting it should not replace the more accurate least-square fitting if possible.

### 3.6.3 Least-squares fitting method

Another important method in determining the optical constants of new materials is the least-squares fitting procedure. For this method to be applicable, the spectra must be in the low field limit exhibiting one positive and one negative extremum for each critical point. The complex resonant lineshapes then take the form of equation (20) repeated here for clarity.

$$\frac{\Delta R}{R} = Re [Ce^{i\delta}(E - E_g + i\Gamma)^{-n}] \quad (20)$$

where  $C$  and  $\delta$  are the amplitude and phase factors, and nonnally  $n \geq 2$ . There are five unknowns:  $C$ ,  $E_g$ ,  $\Gamma$ ,  $\delta$  and  $n$ . The amplitude is readily calculated as it is only a scaling factor, and the desired critical point provides  $n$ . It should be noted however, that since  $C$  is only proportional to  $\xi^2$ , it cannot give its absolute magnitude. The band gap energy  $E_g$  and  $\Gamma$  are determined directly from the experimental lineshape, while the ratio of absolute magnitude of the two extrema determine  $\delta$ [52].

### 3.6.4 Doping level effects

The doping concentration greatly impacts the operating characteristics of the semiconductor device. Figure 3 shows how the electric field varies linearly with distance.

It will have a maximum value at the surface  $\xi_{\max}$  and a value of zero at a distance  $d$ .

Two equations utilized by Shay[7] to determine  $\xi_{\max}$  and  $d$  are,

$$\xi_{\max} = \left( \frac{2eN_d\psi}{\epsilon} \right)^{1/2} \quad (37)$$

$$d = \left( \frac{2\epsilon\psi}{eN_d} \right)^{1/2} \quad (38)$$

where  $\epsilon$  is the dielectric constant,  $N_d$  (or  $N_a$ ) is the doping density and  $\psi$  is the total amount of band bending. An increase in the carrier concentration results in an increase in  $\xi_{\max}$ , but lowers  $d$ . More specifically,  $\xi_{\max}$  increases as  $N_d^{1/2}$ . Since Franz-Keldysh peak spacing is proportional to the electric field as  $\xi^{2/3}$ , the peak spacing in the low limit should vary as  $N_d^{1/3}$ [7]. A contribution of neutral donors or compensated acceptors from below the Fermi level in the bulk, while not providing free carriers, do contribute to the effective  $N_d$ , resulting in a lower calculated value of  $N_d$ .

### 3.6.5 Photoreflectance adsorption measurements

PR is used to quantitatively study semiconductor surface adsorption effects. The basic method allows calculations of the heat of adsorption by assuming reversible adsorption, and to simplify analysis, assumes that the spectral amplitude is proportional to surface coverage. Point spectra are calculated at various temperatures and pressures when a given adsorbate achieves equilibrium. A temperature versus amplitude graph is then generated



for each pressure. Another graph can then be generated by removing the constant amplitude temperature and pressure points and plotting  $\ln P$  vs  $1/T$ . The slope of the lines then are related to the Clausius-Clapeyron equation,

$$\left. \frac{d(\ln P)}{d(1/T)} \right|_A = -\frac{\Delta H_A}{R} \quad (39)$$

A final plot of  $\Delta H_A$  vs signal amplitude reveals a qualitative step function describing the change in heat of adsorption.

## 4 Experimental

The apparatus was configured as shown in Figure 7 to perform PR on the  $E_0$  region of GaAs. The optical and detection components are typical of a system design for PR studies. The white light was provided by a 100 watt sealed, tungsten-halogen lamp, model PTI A1010 with a LPS200X power supply. It was chosen for use due to its very high light collection efficiency through an elliptical reflector, and its ability to produce a stable, uniform illumination of the sample surface area.

The white light was directed through a PTI 01-002 quarter-meter monochromator. The monochromator was outfitted with a stepper motor, allowing it to be either operated manually with a dial, or computer driven. The monochromator was calibrated by a krypton calibration lamp for decreasing wavelengths, and is equipped with two gratings: 750nm and 400nm, with 1200 lines/nm each. A calibration was performed at each grating yielding:

$$\text{Grating I: Blaze-400nm, } \lambda_{cal} = 1.00121\lambda_{dial} + 6.31(nm) \quad (40)$$

$$\text{Grating II: Blaze-750nm, } \lambda_{cal} = 1.00265\lambda_{dial} - 0.876(nm) \quad (41)$$

The calibrated wavelength is represented by  $\lambda_{cal}$ , while  $\lambda_{dial}$  refers to the dial nominal value. The second grating was used since the working range for  $E_0$  of GaAs is from 1125nm to 375nm. A color glass 495nm longpass filter was attached to the exit port of the monochromator to preclude any second-order violet light from being transmitted from

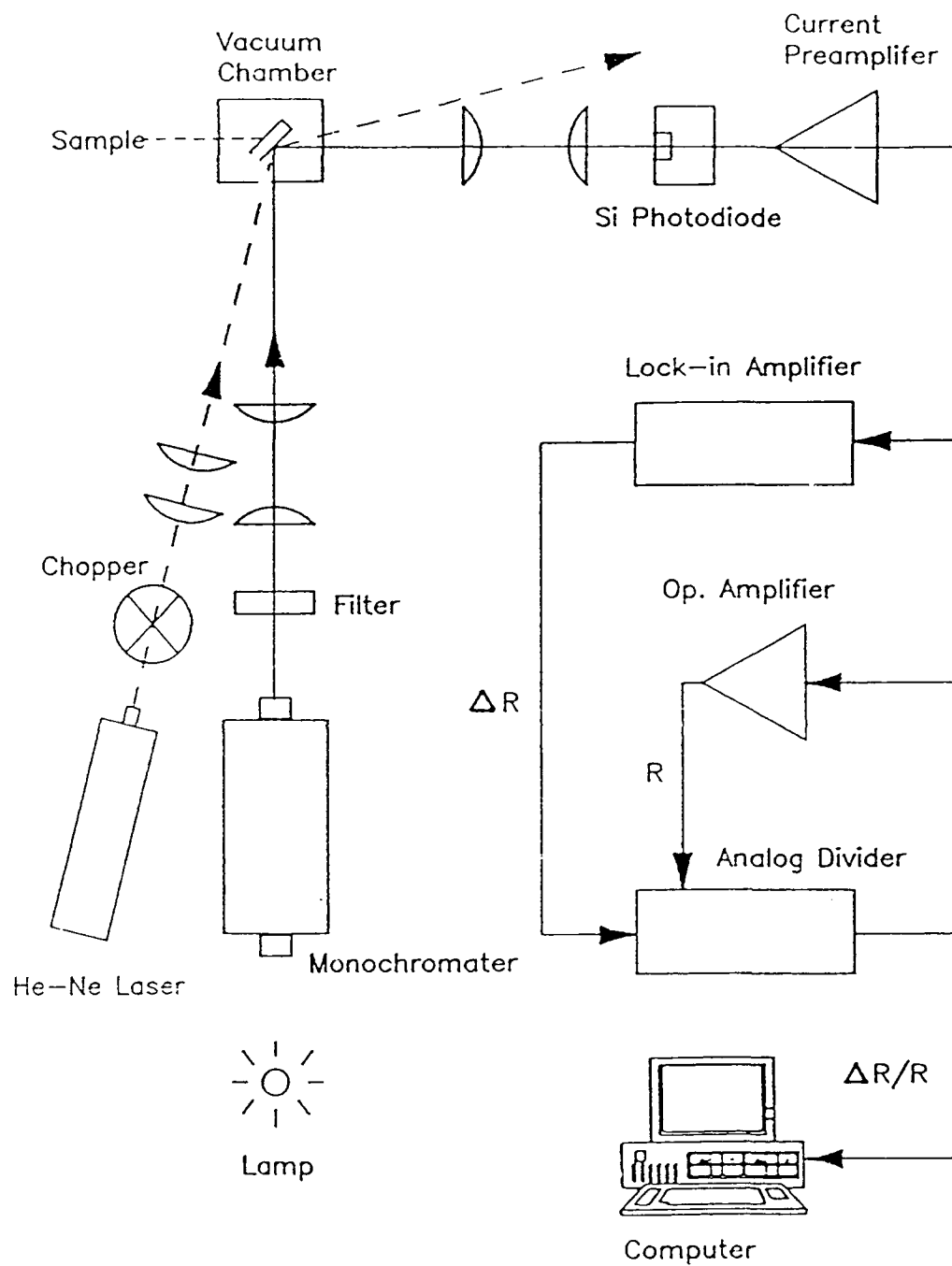


Figure 7. Schematic diagram of the photorefectance setup.

the monochromater. The monochromater had adjustable rectangular slits that were set to maximize the R signal (up to 10 volts), and still maintain high resolution. For example, a n-type sample with slit width setting of 1.35nm, yielded a R value of around 9 volts, and a resolution of 4.32nm.

The exiting filtered monochromatic light from the monochromater was directed through a set of plano-convex lenses to converge on the sample at a 45° angle. The illuminated spot on the sample was approximately 20mm × 1.35mm, the latter being dependent on the exit slit width setting, which ranged from 1.25mm to 1.5mm. The probe beam was reflected off the sample at 45° through a second set of plano-convex lenses converging on the photodiode, which served as a collector. A set of 715nm longpass filters was used before and after the second lens set to block stray laser radiation which could interfere with long wavelength measurements.

The perturbation beam was provided by a Uniphase 106-1, 10mW, HeNe laser. The laser produced a 632.8nm wavelength of light to provide  $h\nu \geq E_g$ . This corresponds to  $1.959\text{eV} \geq 1.424\text{eV}$  of GaAs at room temperature. Two cylindrical lenses were used to enlarge the laser beam to ensure the entire source light on the sample was being illuminated. This was necessary since the laser beam diameter was only 0.68mm. The lenses were mounted in a horizontal and vertical position to yield a rectangular beam of the required dimension. The laser was polarized in the (110) direction. A Stanford Research Systems SR 540 optical chopper was placed between the laser and the first

cylindrical lens to achieve the PR perturbation. It normally was set at 390Hz. A frequency study determined that operation at this frequency virtually eliminated background noise, yet allowed sufficient response time for the surface electric field to return to steady state, as noted by a square waveform signal on the oscilloscope.

The reflected signal from the sample was detected by a Hamamatsu S1336-44BK Si diode. The photodiode was connected to a current preamplifier to amplify current into voltage in the desired range ( $10^5$  to  $10^9$ ). The photodiode was encased in a lightproof box, along with the second set of lenses and third filter, to eliminate artificial light effects. The output voltage of the preamplifier was connected to a Princeton Applied Research JB-5 lock-in amplifier, and to the analog voltage divider. The lock-in amplifier was operated at the chopping frequency of the laser by setting the frequency knob equivalent to the input frequency of the optical chopper (usually 390Hz). It produced the  $\Delta R$  component of the signal and transmitted it to the analog divider. With the signals from the lock-in and the preamplifier, the desired ratio  $\Delta R/R$  was calculated by the divider. The analog divider was designed to incorporate an amplification factor to yield the quantity  $(10 \times \Delta R)/R$ . Otherwise, the small  $\Delta R$  signal would be too little causing computer induced discretization errors. Also, a slit width had to be used that would not give a small R value, otherwise overloading of the divider would occur. The analog voltage divider was connected to a data acquisition and control adaptor installed in a PC-Too 00286-8 computer.

The sample was mounted in a small ultrahigh vacuum (UHV) chamber pumped by a CTI-Cryogenics Cryo-Torr 100 high-vacuum pump, with a Model 8001 controller and Model 8300 compressor. The chamber setup is depicted in Figure 8. The high cryo-pumping speed of over 100 liters per second allowed rapid pumpdown to UHV pressures following sample cleaning procedures, which in turn minimized surface contamination effects. An Alcatel 1004AC mechanical pump was used to rough pump the chamber and to pump the gas handling system lines. The 1.5 liter chamber was cryo-pump supported, with the main component being the optical cube. Two ports of the cube contained pyrex windows for the light path to and from the sample. Other ports contained a leak valve and an ionization gauge, which was run by a series 271 ionization gauge controller from Granville-Phillips, to determine UHV pressures. Two right-angle valves were used to allow rough pumping of the chamber, and to segregate the cryo-pump from the remainder of the chamber allowing continued operation during cleaning procedures or adsorption studies. Two MKS Baratron capacitance manometers of the type 127A and 12211-01000AB from MKS Instruments were attached to the chamber to allow accurate pressure readings in the 1 torr and 1000 torr range respectively. Two electrical feedthroughs were used. One feedthrough was used to perform the hydrogen plasma cleaning. The other feedthrough contained two pins for sample heating (which were also used for sample mounting), and another two pins for thermocouple wire connections.

The sample was mounted as displayed in Figure 9. The two copper blocks were

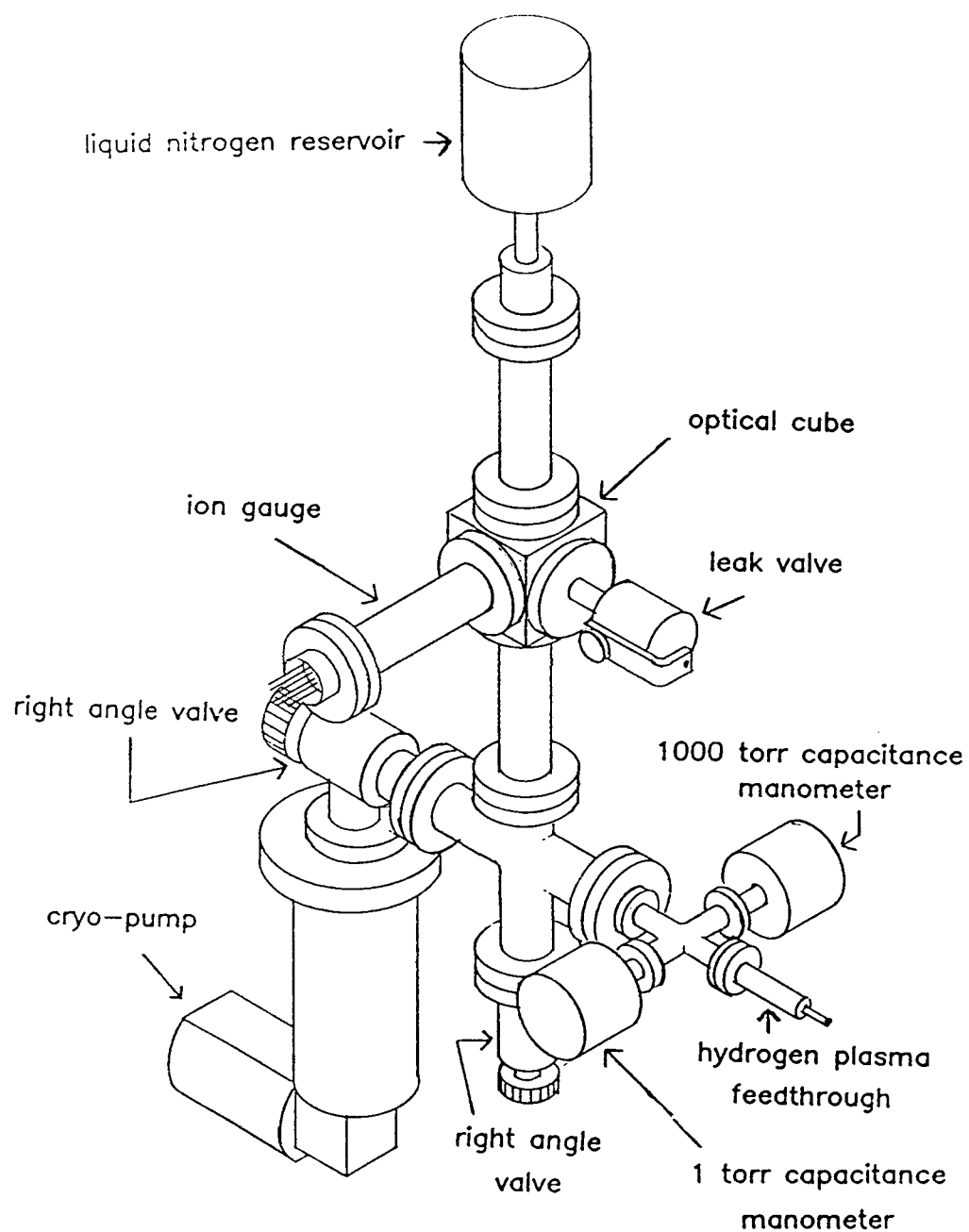


Figure 8. The vacuum chamber arrangement.

not connected, allowing the sample to be heated resistively by an Electronic Measurements ATR 250-1 power supply. The temperature was monitored by a chromel-alumel thermocouple, spring loaded to the back of the sample. An ice bath was used as a reference temperature. The thermocouple wires were threaded through a macor block, which was attached to one of the sample mount sides, to provide support for the spring loaded wire, and to keep the thermocouple wires from contacting the sample mount. A preamplifier was used to multiply the temperature reading by 100 in order to maintain a consistent temperature during PR scans. The sample was cooled through a liquid nitrogen cryostat.

There were two BASIC programs used by the computer to obtain the PR spectra. The first program was used to reproducibly start the monochromator at a desired wavelength. It is listed in Appendix 1[49], and a block diagram is shown in Figure 10. To meet calibration requirements, the scanning was always performed from a higher to a lower wavelength. The second program was the main program for taking PR data, and is listed in Appendix 2[49]. Its block diagram is depicted in Figure 11. The computer calculated the wavelength by knowing the starting wavelength ( $\lambda_s$ , set in Program 1), the scanning time (t), and the scanning speed (v). An equation representing an uninterrupted scan would be:

$$\lambda = \lambda_s - vt \quad (42)$$

It is necessary to limit the program to a consistent speed, so scanning time can be



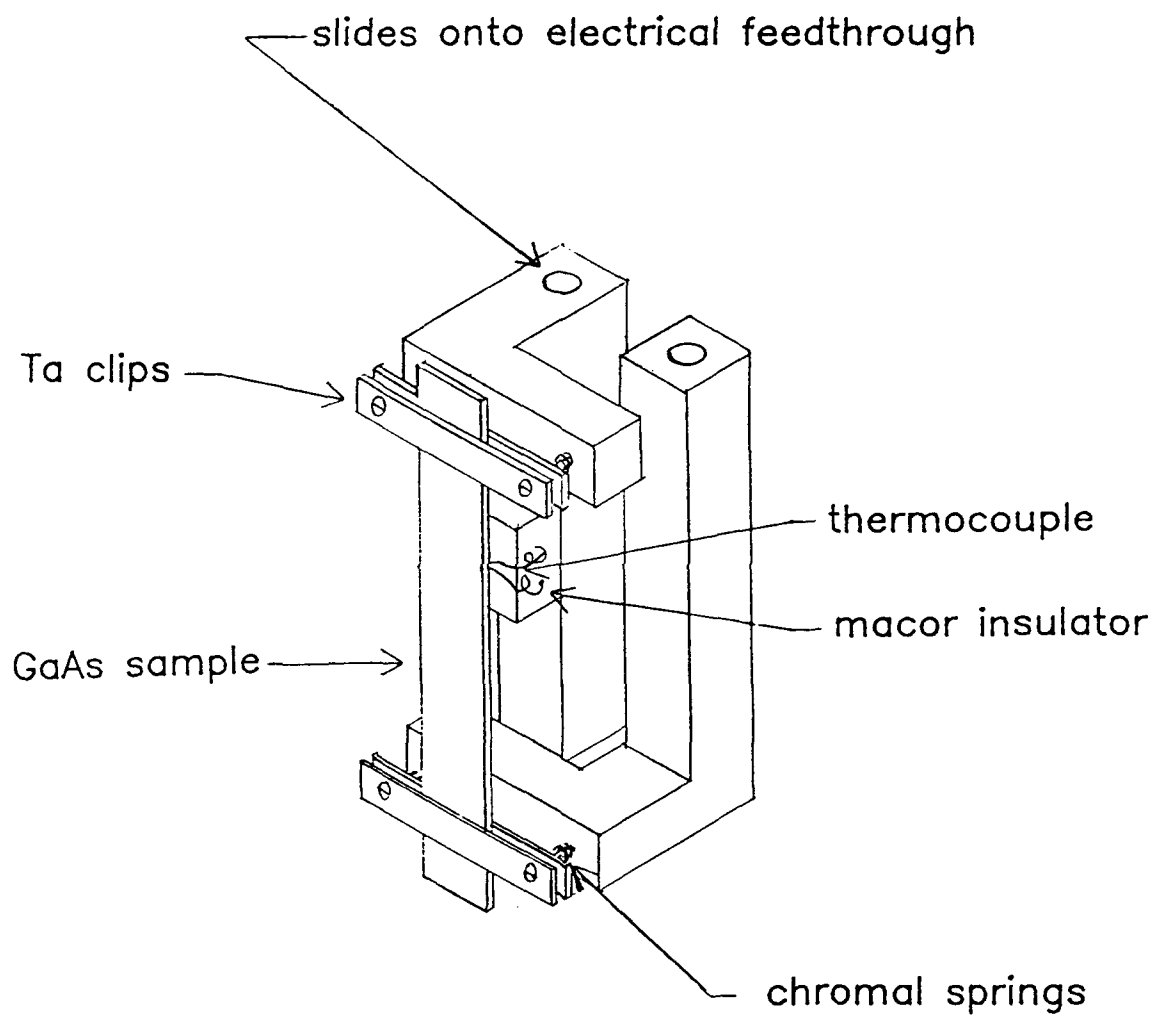


Figure 9. Schematic view of the sample mount.

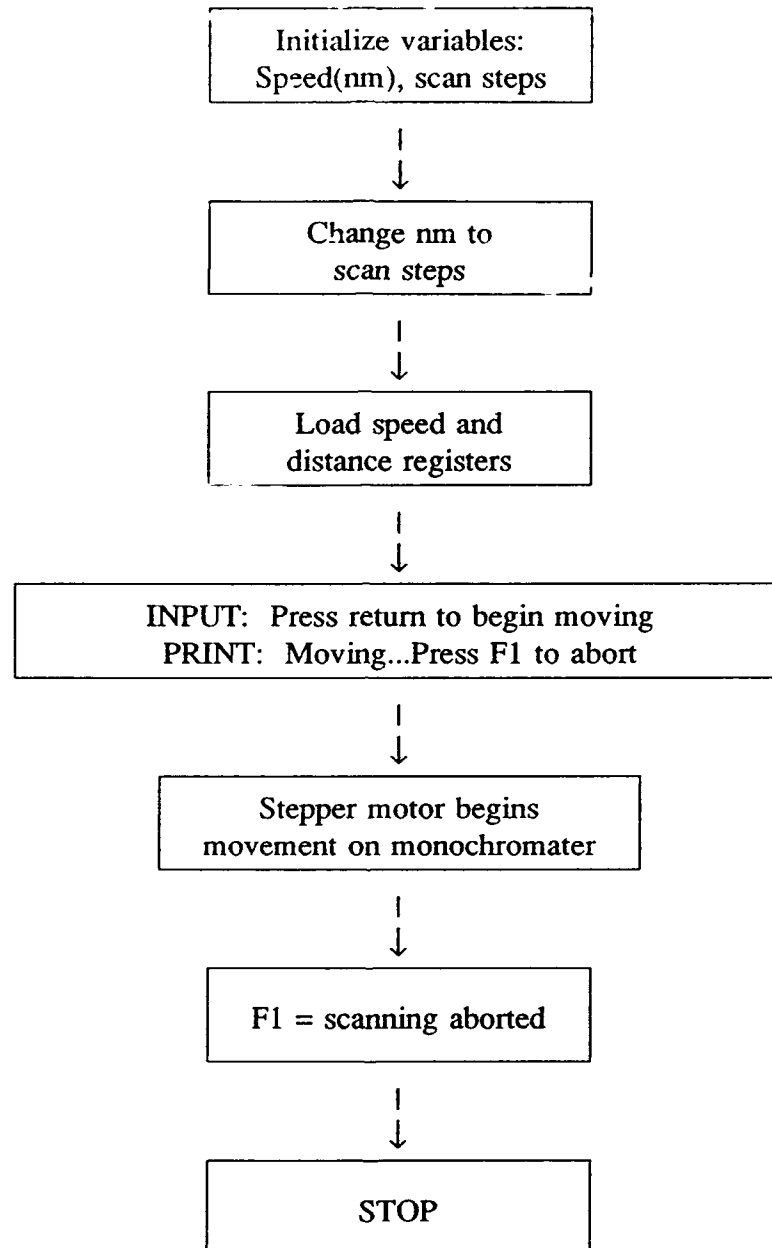


Figure 10. Block diagram of Program 1 used to reproducibly start the monochromater.

properly correlated to wavelength. Therefore, the monochromator could be set to run at full steps (2nm/sec) or half steps (1nm/sec). Half steps with a speed of 1nm/sec were normally used as they provided a more coherent spectrum with better delineated peaks. The number of data points per second affected the peak height and lineshape position. To maximize the peak height and minimize both the movement of the lineshape from its original position and the scan time, three data points per second were used.

Several signal levels had to be used on the lock-in amplifier, dependent on the size of the signal and the amplitude of the photoluminescence generated by the laser. The photoluminescence was zeroed out each time before a scan was taken. The sensitivity of the lock-in amplifier was calculated to be 0.16mV/V of output, and the lock-in had a  $\pm 5V$  output range at each signal level. The final  $\Delta R/R$  calculation was

$$\frac{\Delta R}{R} = \frac{V \times S_{LIA} \times A}{10 \times SL} \quad (43)$$

where  $S_{LIA} = 0.16mV$  is the lock-in amplifier sensitivity, SL is the lock-in amplifier signal level, and A is the amplification factor from the photodiode preamplifier. The V refers to the conversion of the digital value (x) back into the voltage, which can be represented by,

$$V = \frac{20}{4096} X - 10 \quad (44)$$

The adapter used a 12 bit converter, so it could express 4096 different voltage levels

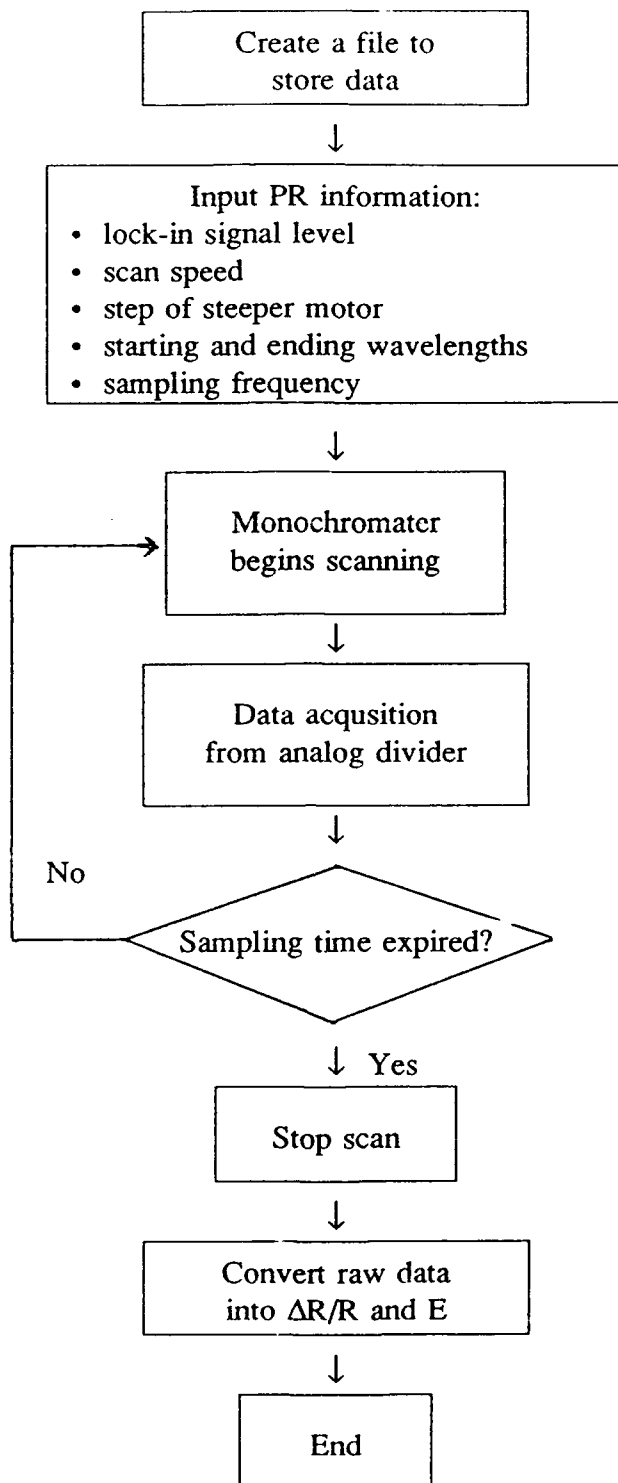


Figure 11. Block diagram of Program 2 used for PR data acquisition.

between  $\pm 5V$  range in the system. Switches were set in the data acquisition and control adapter as follows:

- Adapter number 0
- Analog input from channel 3
- Analog input range (A/D) -5V to +5V
- Interrupt-Request(IRQ) level 7[58]

These settings were necessary to ensure proper operation of the computer setup.

Four types of GaAs samples, obtained from Crystal Specialties International, were used in the PR experiments:

- n-type, Cr doped GaAs (100),  $1.6 \times 10^{17} \text{ cm}^{-3}$  (Sample A)
- n-type, Si doped GaAs (100),  $1.8 \times 10^{18} \text{ cm}^{-3}$  (Sample B)
- n-type, Si doped GaAs (100),  $4.6 \times 10^{17} \text{ cm}^{-3}$  (Sample C)
- p-type, Zn doped GaAs (100),  $2.1 \times 10^{18} \text{ cm}^{-3}$  (Sample D)

These samples had already been prepared for experimental use by polishing one surface and being misoriented  $2^\circ$  toward the (110). A scribe was used to cut the samples into rectangles approximately 25mm long  $\times$  5mm wide. Normally, samples were chemically etched before being mounting into the chamber. The procedure included degreasing the sample with trichloroethylene, rinsing with acetone and methanol, then performing an acid etch for 15 seconds with 15:1:1 mixture of  $\text{H}_2\text{SO}_4$ : $\text{H}_2\text{O}_2$ : $\text{H}_2\text{O}$ . The acid solution was rapidly diluted and rinsed away with running deionized water, then dried with a stream of dry nitrogen. This procedure seems to minimize the formation of excessively thick oxide layers[59]. The acid etch was performed using transistor grade chemicals. This

grade of chemicals was used since they were manufactured using a 0.2 micron filter (allowing very few particulates), thereby minimizing contamination of the sample surface. Analytically clean breakers and tools used with the sample were required, otherwise unintentional sample contamination resulted. Following mounting and placement in the chamber, the sample was promptly brought to UHV. UHV could be achieved within 20 minutes to the  $10^{-8}$  torr range, when the cryo-pump was not allowed to degas. To remove the carbon contaminants in the chamber, the system was baked for a period of 48 hours at 200°C. This allowed the system to achieve pressures in the  $10^{-9}$  torr region.

After the bakeout of the system, the sample was hydrogen plasma etched for five minutes at 400°C to remove any remaining carbon contaminants. This method was employed by Chang et al.[39] and found to leave the sample surface free of carbon. The hydrogen was leaked in through the leak valve to a pressure of 100 mTorr, then a plasma was started with a tesla-coil through the electrical feedthrough mounted on the lower part of the chamber setup (see Figure 8). The sample was then annealed to 550°C for five minutes to remove any oxide that had formed following the acid etch, yet before UHV was achieved, and to allow surface reconstruction. The combination of the acid etch, hydrogen plasma, and subsequent anneal was tested in a chamber capable of performing Auger spectroscopy, and found to yield a clean surface, free of noticeable contaminants. It should be noted that the hydrogen plasma could not be performed at too high a power, otherwise the copper mounts left a residual deposit inside the chamber skewing the PR results.

The photoluminescence from the sample was fairly large, often larger than the R

signal at higher temperatures. Initially a rectangular slit was employed in an attempt to limit the amount of photoluminescence, but this was unsuccessful as the slit could not be fine-tuned to match the slight changes in optical alignment that occurred, resulting in significant differences in PR amplitude. By adjusting the signal level on the lock-in amplifier, the slit was not necessary, and the photoluminescence could be zeroed out of the PR signal.

Water adsorption studies were accomplished by utilizing a two-inch diameter by four inch-long stainless steel bottle filled with deionized water. The water was purified by using a repetitive freeze-pump-thaw process. Water traveled through a gas handling system, entering the chamber through the chamber leak valve.

## 5 Results and Discussion

### 5.1 PR sample characterization

The significance of PR as a sample characterization tool has already been discussed. In the research presented here, PR was effectively used to analyze the various sample types, yielding results demonstrating the effectiveness of cleaning procedures and water adsorption effects. The sensitive nature of PR to changes in surface phenomena were clearly observed for  $\Delta R/R$  signals as small as  $1 \times 10^{-6}$ . Four sample types were studied, and each is presented sequentially, with a brief comparison at the end of the chapter.

#### 5.1.1 PR on sample A

The n-type, Cr doped GaAs(100), with a  $1.6 \times 10^{17} \text{ cm}^{-3}$  carrier concentration (Sample A), was the first sample studied. Sample A was primarily used to validate and improve the initial PR setup. The scans were very crude as usually neither an analog divider nor a liquid nitrogen cryostat was used. This meant that deviations in the absolute signal could not be accounted for, and that scans could only be performed at room temperature or above. The sample was not acid etched or  $\text{H}_2$  plasma etched to clean it, leaving both carbon contaminants and an oxygen oxide on the surface. A clean surface was not necessary since the sample was only being used to obtain a crude PR spectrum that would both display qualitative PR data and validate the PR setup. Also, no quantitative data were to be extracted, so usually only a chart recorder was used to record the scan. A typical PR signal for sample A at room temperature is shown in Figure 12 (a). Three



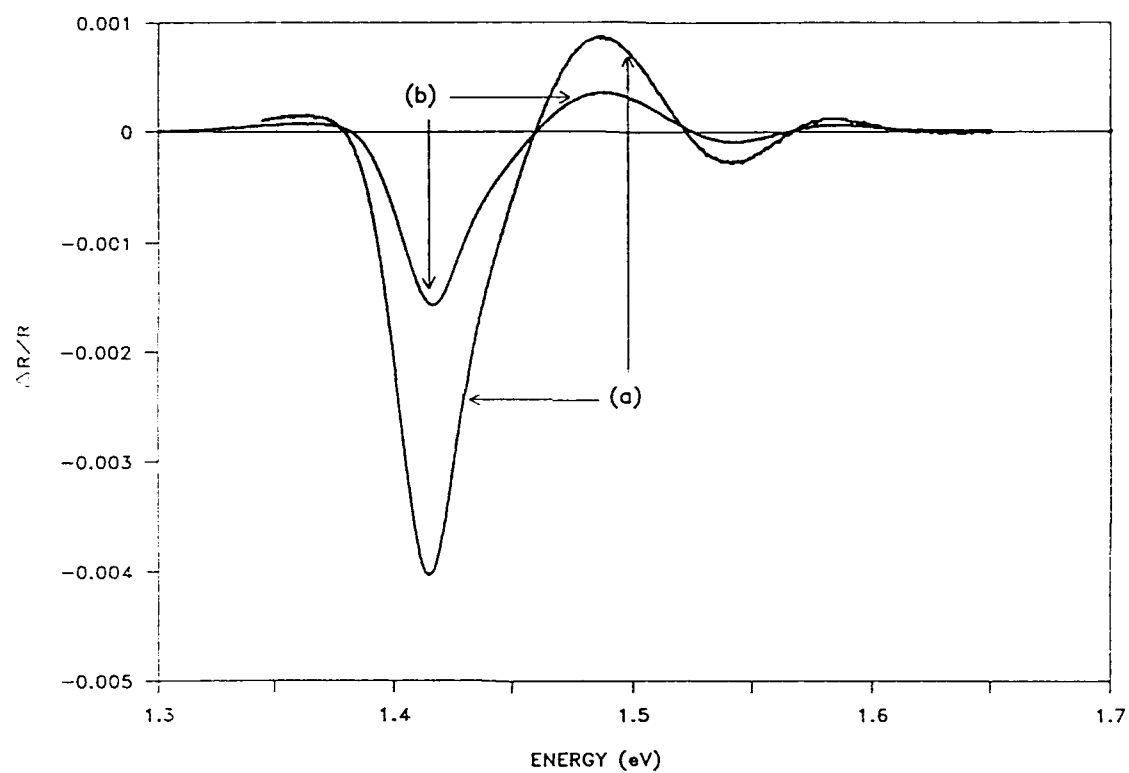


Figure 12. Sample A room temperature scan without slit (a), with slit (b).

main extrema are evident, which correlate to the  $E_0$  portion of the PR spectra of sample A, and the beginning of the Franz-Keldysh oscillations is observed at high energies. The photoluminescence was quite large, being about 80% of the maximum PR reading (1.56V vs. 1.90V respectively). A small rectangular slit was then installed in the laser beam to reduce the photoluminescence, by limiting the amount of sample surface being illuminated by the laser. This allowed a more accurate PR reading since a more sensitive scale could be used on the lock-in amplifier. The photoluminescence was reduced by almost a factor of two (0.80V) from its previous value. Figure 12 (b) depicts a PR spectrum with the rectangular slit installed. The PR signal was also reduced by approximately one-half, but part of the PR signal reduction was possibly due to the unobstructed laser beam not being completely coincident with the source light beam. Ensuring the two beams were coincident was extremely difficult, since a slight change in alignment required simultaneous adjustment of the slit. The setup was not capable of absorbing external vibrations, resulting in alignment fluctuations.

A temperature study was performed on sample A under the same conditions mentioned above, except that now the sample was annealed to 600°C for two minutes before each scan was taken. It was found that reproducible results could be achieved in this manner. Also, the anneal resulted in a PR signal with the slit being greater than the original scan without the slit, demonstrating a cleaner surface. Scans were taken at the following temperatures: 298K, 323K, 373K, and 423K. The results are shown in Figure

13. The PR signal amplitude decreased from its absolute maximum value at 298K of 1.90V to no observable signal at 423K. Each spectrum shifted toward higher wavelength, and the linewidth broadened slightly (spacing between peaks) with higher temperatures, in agreement with earlier studies[7,13,14].

### 5.1.2 PR of sample B

The second sample used in the PR studies, was a n-type, Si doped GaAs(100), with a  $1.8 \times 10^{18} \text{ cm}^{-3}$  carrier concentration. A typical air-oxidized spectrum is shown in Figure 14 (a). Sample B displayed two extrema, the first being a negative peak, which was approximately 130% larger than the positive peak (second extremum). The slit dimensions were narrowed to reduce the photoluminescence another 30% (1.15V to 0.79V). The PR signal was reduced to around half of its previous value ( $7.0 \times 10^{-4}$  vs.  $3.4 \times 10^{-4}$ ) by this action as is shown in Figure 14 (b). As a result of the complexity of aligning the slit with the main PR setup, and the associated reduction in  $\Delta R/R$  signal, the possible advantage in accuracy gained by the slit was not considered as an adequate tradeoff, and so was abandoned. Since photoluminescence was assumed to remain essentially constant at constant temperature, it was zeroed out on the lock-in amplifier prior to each scan.

Sample B was  $\text{H}_2$  plasma etched at 400°C and 100 mTorr for four minutes to remove the carbon contaminants from the sample surface. Figure 15 shows the spectra before (a) and after (b) the  $\text{H}_2$  plasma. An anneal to 600°C should allow the

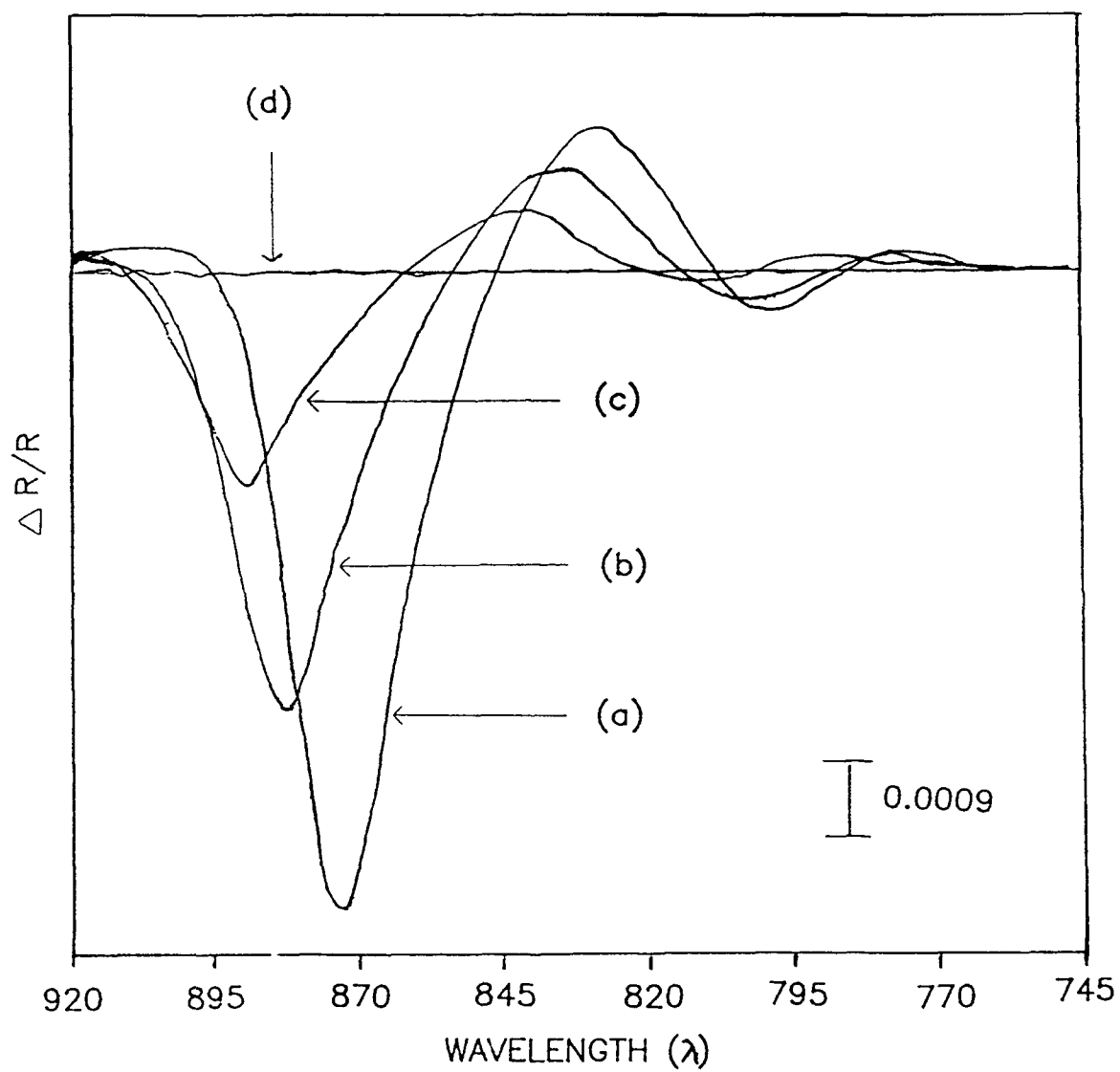


Figure 13. Sample A spectra at different temperatures: 298K (a), 323K (b), 373K (c), and 423K (d).

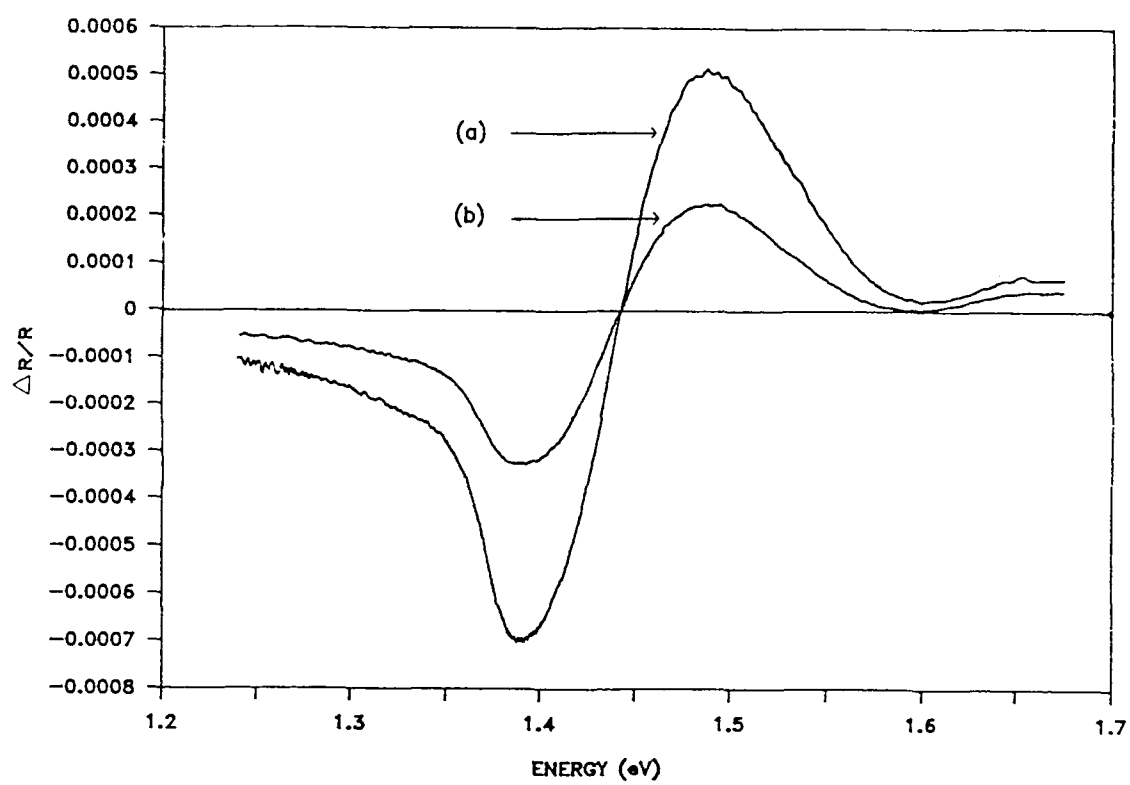


Figure 14. Sample B room temperature scan without slit (a), with slit (b).

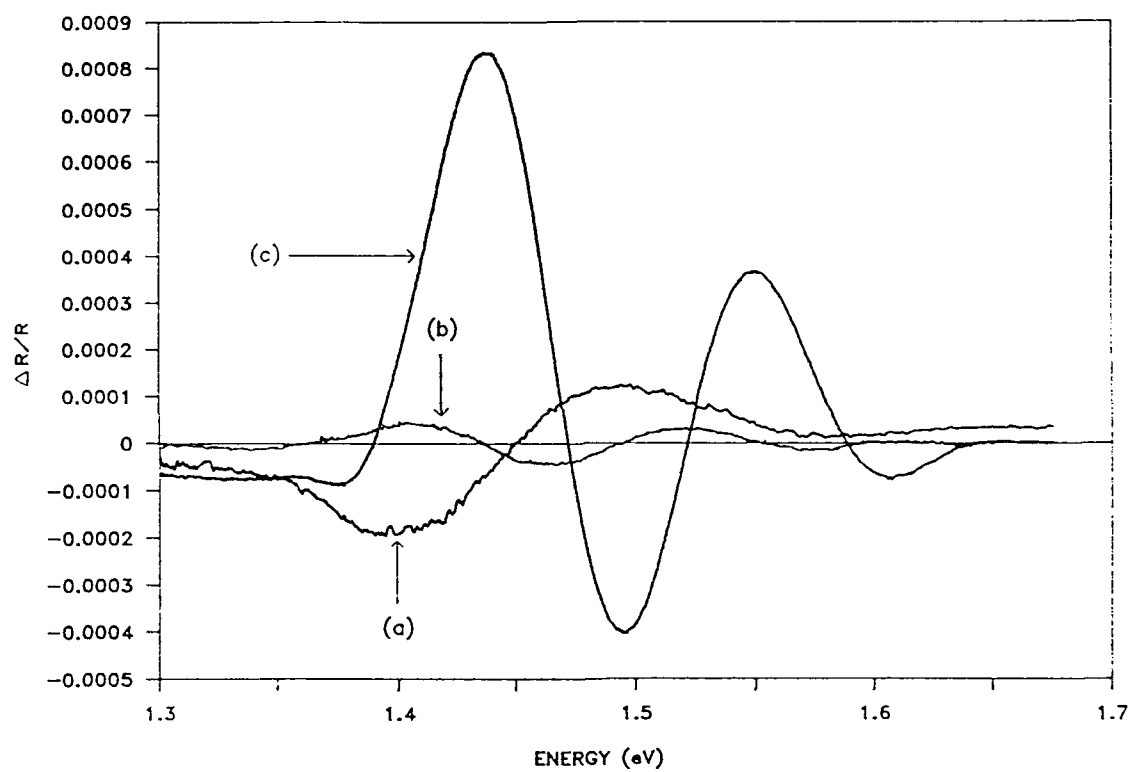


Figure 15. Sample B room temperature spectra before H<sub>2</sub> plasma (a), after H<sub>2</sub> plasma (b), and following a 600°C anneal (c).

reconstruction of the crystal surface plus remove any remaining oxidation. Figure 15 (c) shows this is the case. An interesting phenomenon which appears to never have been reported before, is the significant change in PR amplitude, lineshape and linewidth. Following the H<sub>2</sub> plasma, four peaks were obtained not including the previous first peak, which was not observable. The Franz-Keldysh oscillations became clearly evident. The spectrum narrowed considerably, with the peaks shifting over 0.5 eV in the direction of decreasing energy. Spacing between the peaks was reduced by about 25 percent. Peak amplitudes increased by as much as a factor of three. The photoluminescence also increased to a value of 1.4 V.

A typical temperature study conducted on sample B from 123K to 523K, resulted in the spectra seen in Figure 16. The gradual peak shift to lower energies at higher temperatures coincides with the previous results of Shay[7]. The linewidth narrows from the highest temperature reading (473) to the lowest temperature by just under a factor of two. The peak amplitude increases from 123K to 273K then decreases to 473K. No signal was observed at 523K, so it is not shown. The photoluminescence continually decreased with increasing temperature. This is expected since photoluminescence results from the recombination of excited carriers following photon absorption, and with increasing temperature, the energy level of the electron traps rises toward the conduction band, which allows less charges to be trapped and more recombination of the electron-hole pairs. Other temperature studies substantiated the findings discussed above.

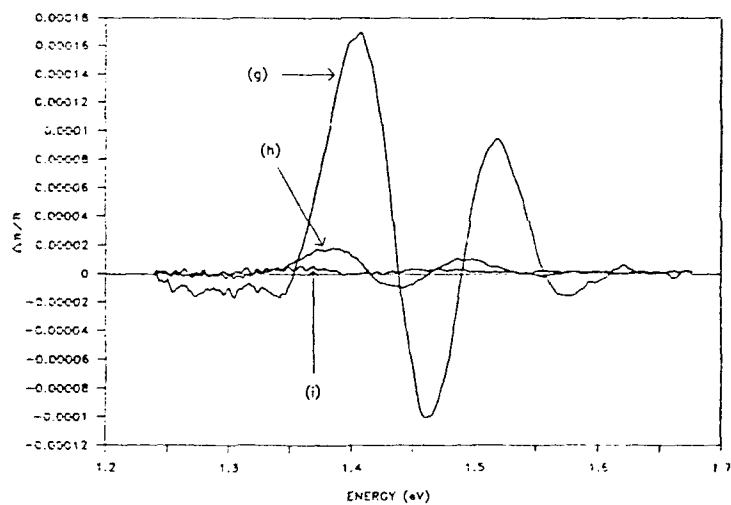
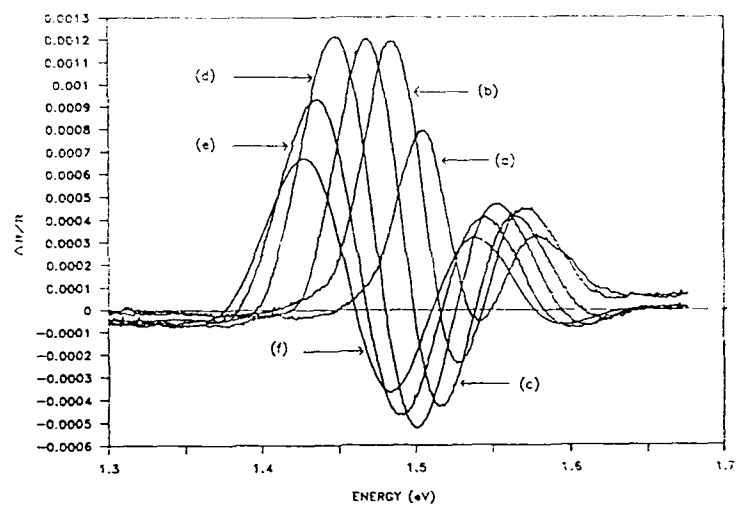


Figure 16. Sample B spectra at different temperatures: 123K (a), 173K (b), 223K (c), 273K (d), 298K (e), 323K (f), 373K (g), 423K (h), and 473K (i).



It should be noted that a reproducible spectrum could not be obtained following a series of  $H_2$  plasmas. Figure 17 typically depicts how the FKO continued to shift toward lower energy, and the linewidth narrowed following each  $H_2$  plasma. This might be explained by the fact that stronger intensity  $H_2$  plasmas damaged the surface more during ion bombardment, sometimes possibly beyond anneal reconstruction. Also the amount of linewidth narrowing and shift seemed dependent on the intensity of the plasma.

Following a  $H_2$  plasma/anneal sequence (one  $H_2$  plasma at 100 mTorr at 400°C for five minutes, immediately followed by an anneal to 550°C at UHV for five minutes),  $H_2O$  adsorption was performed on the sample at 298K and 200K. A reference scan was taken before adsorbing the  $H_2O$ . Water was initially leaked in at 10 mTorr for fifteen minutes at room temperature (298K), resulting in an approximate 10% increase in peak amplitude, and a slight linewidth broadening as shown in Figure 18 (a). An additional fifteen minutes of  $H_2O$  adsorption resulted in only a fractional increase in signal amplitude, indicating that steady-state had virtually been attained in the first fifteen minutes of  $H_2O$  adsorption. Water adsorption of 40 mTorr at 200K yielded slightly different results as the  $\Delta R/R$  signal only increased 5% as seen in Figure 18 (b). Steady-state equilibrium was achieved within thirty minutes, as a subsequent adsorption of 40 mTorr of water resulted in no change in the spectrum. Photoluminescence decreased from 2.0 volts before, to 1.5 volts after the 40 mTorr, 30 minute adsorption, indicating a degraded surface.

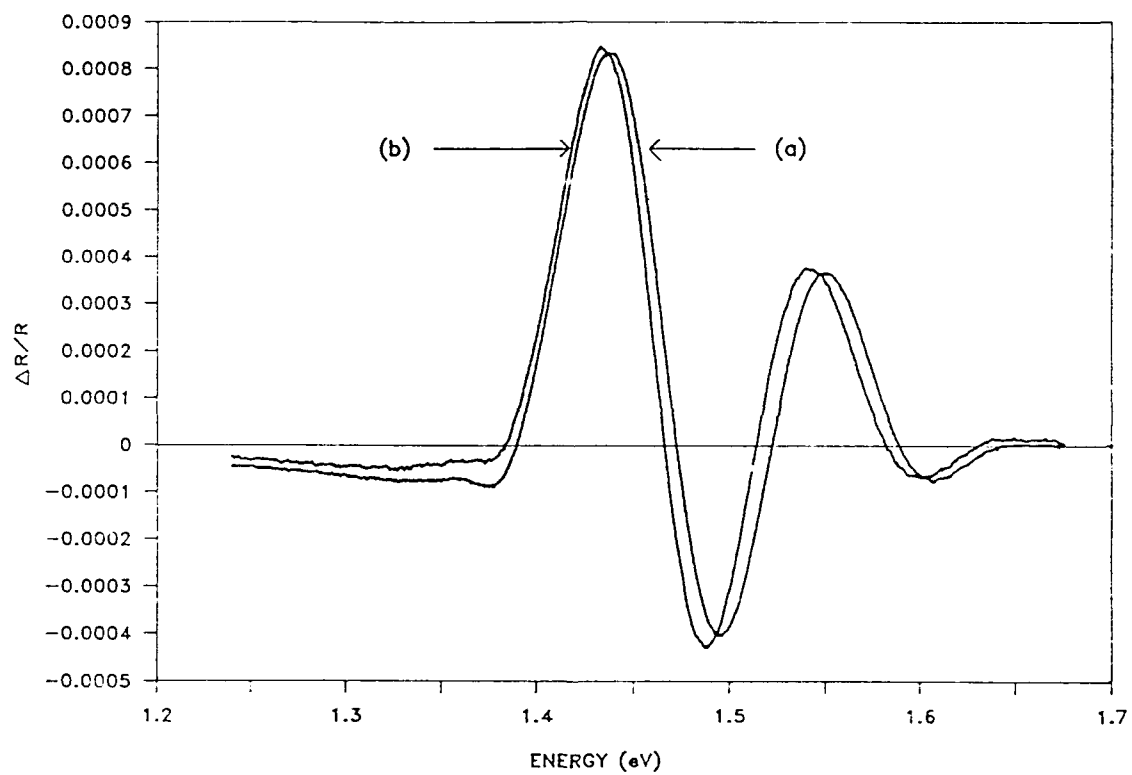


Figure 17. Demonstration of how the  $H_2$  plasma affected the room temperature spectra lineshape. Following  $H_2$  plasma #1 (a), and after  $H_2$  plasma #2 (b).

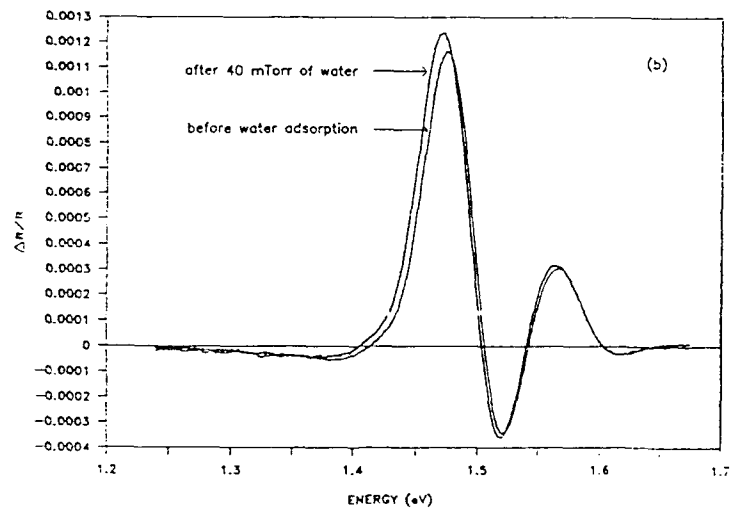
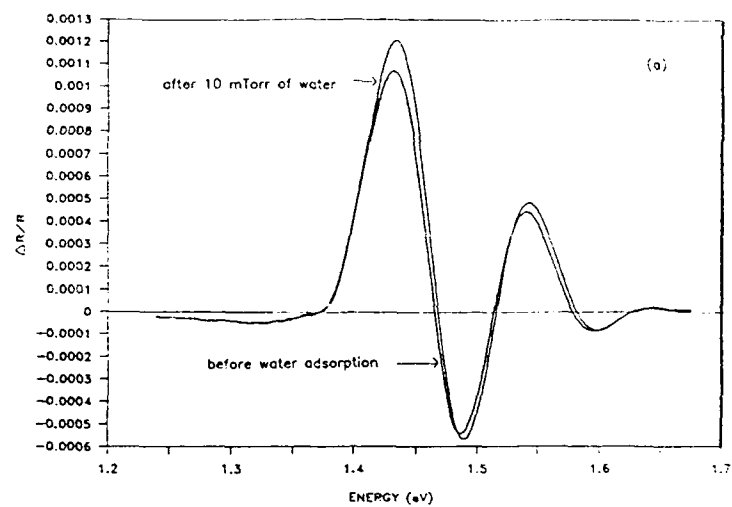


Figure 18. Water adsorption on sample B at 298K (a), and 200K (b).

### 5.1.3 PR of sample C

Sample C was initially used to refine the PR setup so that quantitative results could be obtained. It was necessary to calculate a consistent, optimum scan speed, determine the number of data points per second to be taken during the scan to maximize the quality of the PR signal, find an effective modulating frequency, and work out any anomalies detected in the PR system. Once these items were determined, the PR setup could be used to produce consistent, quality data.

The precise PR scan speed affects the position of the PR spectrum, the responsiveness of the PR system (which in turn affects the spectral peak amplitudes), and the length of time for each scan. A scan speed study performed on sample C yielded the spectra displayed in Figure 19. Sample C was a n-type, Si doped GaAs(100) with a  $4.6 \times 10^{17} \text{ cm}^{-3}$  carrier concentration, and four scan speeds were analyzed. These were: 0.5 nm/s, 1.0 nm/s, 2.0 nm/s, and 3.0 nm/s. The sample had not been annealed beyond 200°C achieved during bakeout, nor chemically or  $\text{H}_2$  plasma etched. The position of the spectra was found to be reproducible with a consistent scan speed. An optimum scan speed minimizes peak height reduction, yet completes the scan as quickly as possible to avoid undesirable effects such as surface recontamination during the scan. The 2.0 nm/s and the 3.0 nm/s scan speeds reduced the peak amplitudes by as much as 2% and 5% respectively. This was unacceptable during the current studies, since a peak reduction of more than 1% was considered unsatisfactory. So these speeds were eliminated. The 1.0

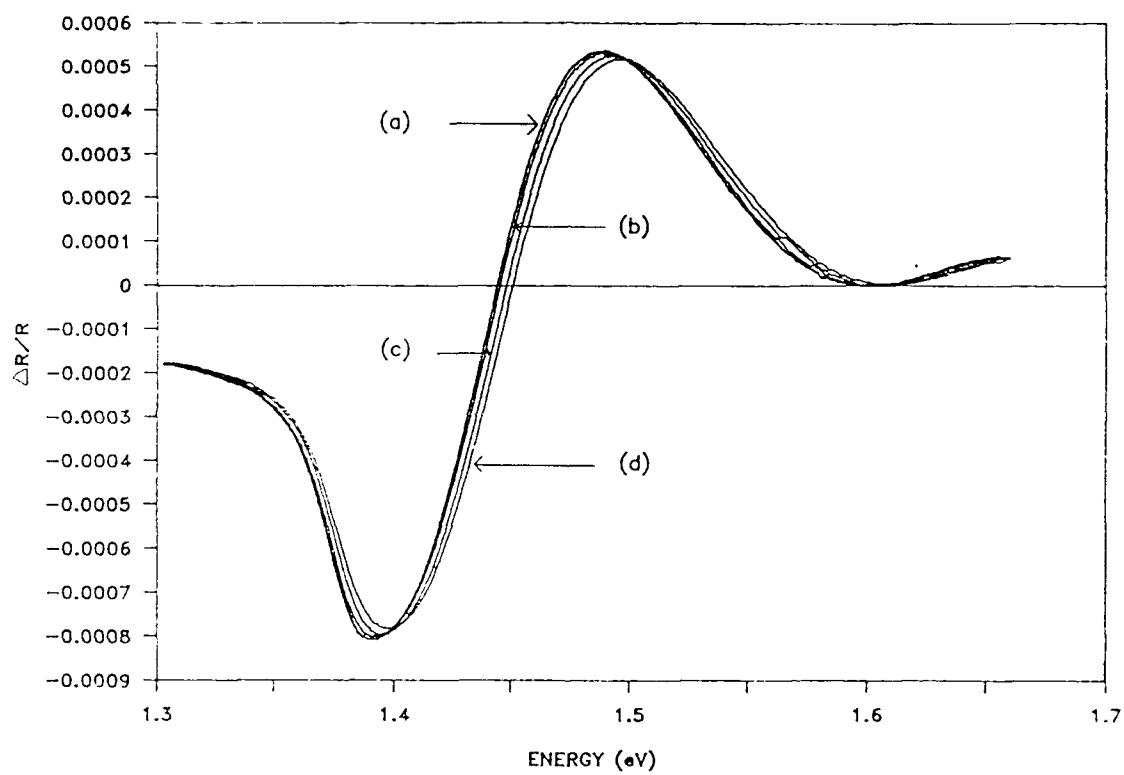


Figure 19. Room temperature scan speed study on sample C: 0.5 nm/s (a), 1.0 nm/s (b), 2.0 nm/s (c), and 3.0 nm/s (d).

nm/s scan speed cut the scan duration in half over the 0.5 nm/s scan speed, yet only reduced the spectra peaks by about 0.5%. This was an adequate tradeoff since the 1.0 nm/s scan speed maximized the PR signal while minimizing the scan time. So, the 1.0 nm/s scan speed was adopted for studies of samples C and D.

The importance of a clean sample surface for adsorption, free of surface contaminants, was discussed previously. Dependent upon how quickly the sample was brought to UHV, the PR signal of an acid etched sample increased as much as 5% to 10% over a non-etched one when brought to UHV within twenty minutes. The longer the sample took to reach UHV, the less the effect on PR signal. For instance, when the cryo-pump had to be regenerated, which meant the sample could take up to two hours to reach UHV, less than 5% increase in PR signal was observed over a non-etched sample.

The number of data points per second taken during a PR scan primarily affects the line quality of the final spectrum. Normally four to six data points per second gives the desired line quality. Using sample C, it was determined, however, that only three data points per second were required to achieve over 99.5% of the six data points per second PR signal. As a result, three data points per second were usually used.

To maximize the  $\Delta R/R$  signal, the lock-in amplifier had to be tuned in identically to both the frequency and phase of the modulating beam. Normally a lock-in amplifier "reads" the frequency being externally input, however; the lock-in amplifier used had to be adjusted manually to coincide with the chopping frequency. Deviations from the

modulating frequency resulted in an altered PR spectrum as shown in Figure 20 on a H<sub>2</sub> plasma etched sample at 250K. Additionally, the operating frequency produced different results at differing speeds since electrical noise and other factors affected it.

Several chopping frequencies were studied on sample C. These included 90Hz, 270Hz, 330Hz, 390Hz, and 2700Hz as displayed in Figure 21 on a wet acid etched, unannealed, nonhydrogen plasma etched sample at 298K. It is seen that the 390Hz  $\Delta R/R$  signal (used as the baseline) produced the largest amplitude with the least amount of electronic noise. The 270Hz spectrum was about 10% smaller in amplitude with around the same amount of clarity, while the 90Hz spectrum was 60% smaller, but was much noisier. This electrical noise was expected since the equipment operating frequency of the facility was 60Hz, and the slower modulating beam could account for the small signal. The 2700Hz signal only yields around 25% of the 390Hz one, possibly due to the fact that the speed of the chopped laser beam did not allow the electric field at the sample surface to return to its unperturbed state. The 330Hz PR spectrum is not shown. It was roughly the same amplitude as the 270Hz spectrum, but was very noisy due to the fact that the cryo-pump produced a vibration at 333 Hz. Other frequency studies conducted on acid etched, annealed, and H<sub>2</sub> plasma etched samples yielded similar results, with the 390Hz chopping frequency being determined to yield the best PR spectra.

The effect of annealing the sample to 550°C can be observed in Figure 22. Sample C was annealed for five minutes, resulting in an approximate 10% increase in PR

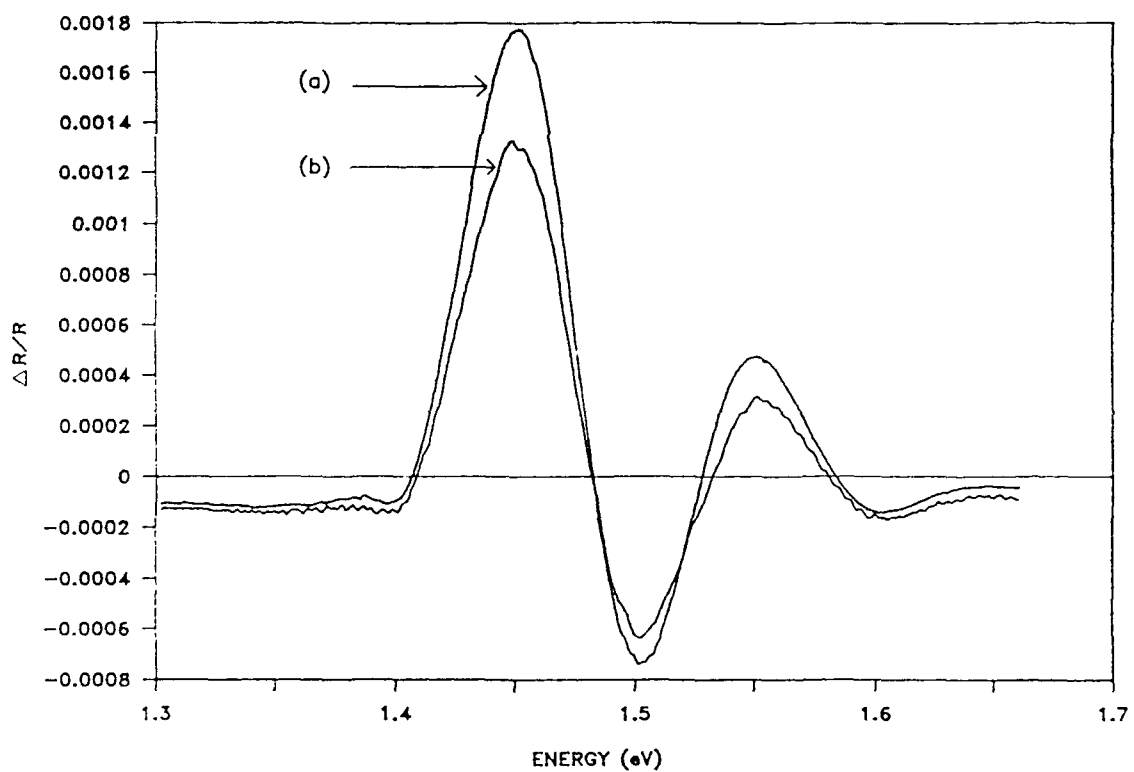


Figure 20. The effects of chopping frequency drift on sample C at 250K: normal spectrum (a), and altered spectrum (b).



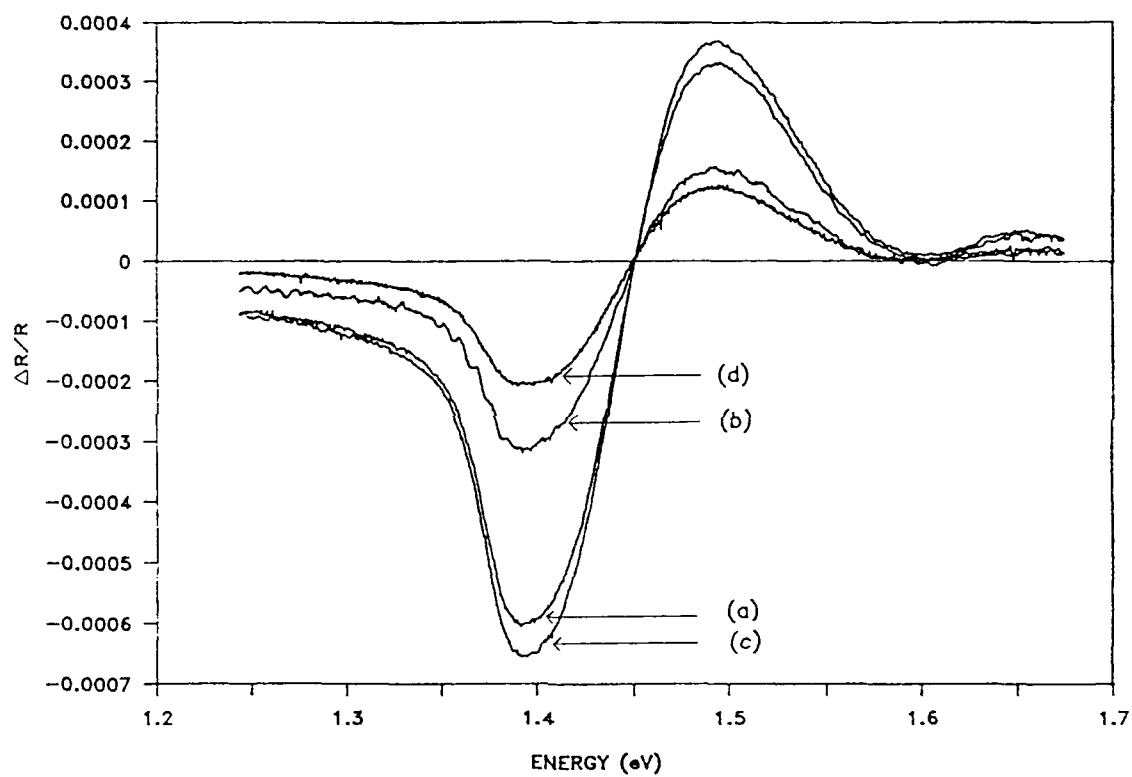


Figure 21. Modulating frequency study on sample C at 298K: 270 Hz (a), 90 Hz (b), 390 Hz (c), and 2700 Hz (d).

signal at 250K, as any remaining oxygen oxidation was removed from the surface. No changes in lineshape or linewidth were observable. Only a single anneal was required to achieve reproducible results, indicating that the oxide layer had been removed from the surface. Similar PR signals were obtained after annealing each new sample, with only the duration of the anneal being significantly impacted by whether the sample was acid etched, and by how long it took the sample to be brought under UHV. The end result following annealing of an acid etched vs. a non-etched sample was found to be less than 5%. A five minute anneal achieved a reproducible PR spectrum to within 2%, irregardless of the length of time before the sample was brought under UHV. It was not determined how the acid etch affected surface adsorption, since it was beyond the capability of the PR system.

Adsorption studies shown in Figure 23 were performed on sample C at 250K to see how the PR spectra was affected when no  $H_2$  plasma etching was conducted to remove the carbon contaminants. Following an anneal, 0.1 mTorr of  $H_2O$  was adsorbed for fifteen minutes resulting in an approximate 7% decrease in  $\Delta R/R$  signal amplitude. Adsorption of 1.0 mTorr of  $H_2O$  for two hours only yielded an approximate 5% decrease in signal. Water adsorption of 10 mTorr for thirty minutes produced no discernable effects. The lineshape and linewidth did not appear to change during any of the  $H_2O$  adsorption. These results were inconclusive and disagreed with those of Seebauer[28], possibly indicating that the surface was too contaminated to allow proper adsorption of

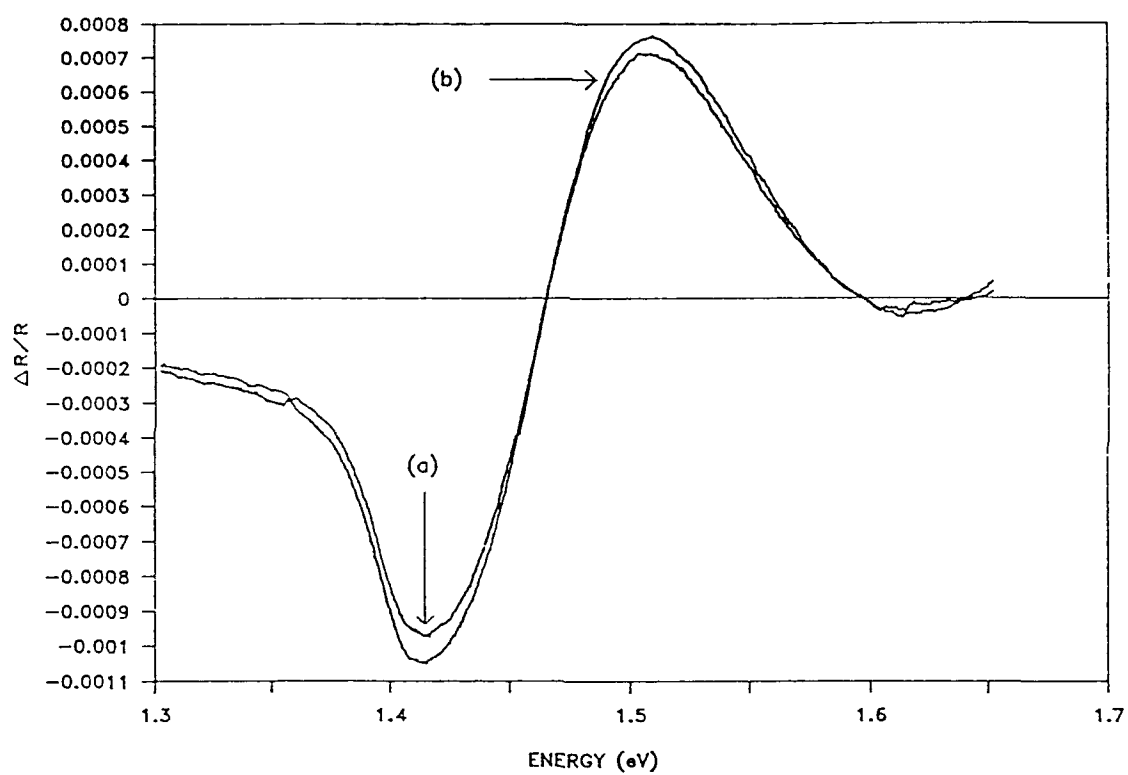


Figure 22. Sample C spectra at 250K: before anneal (a), and after anneal (b).

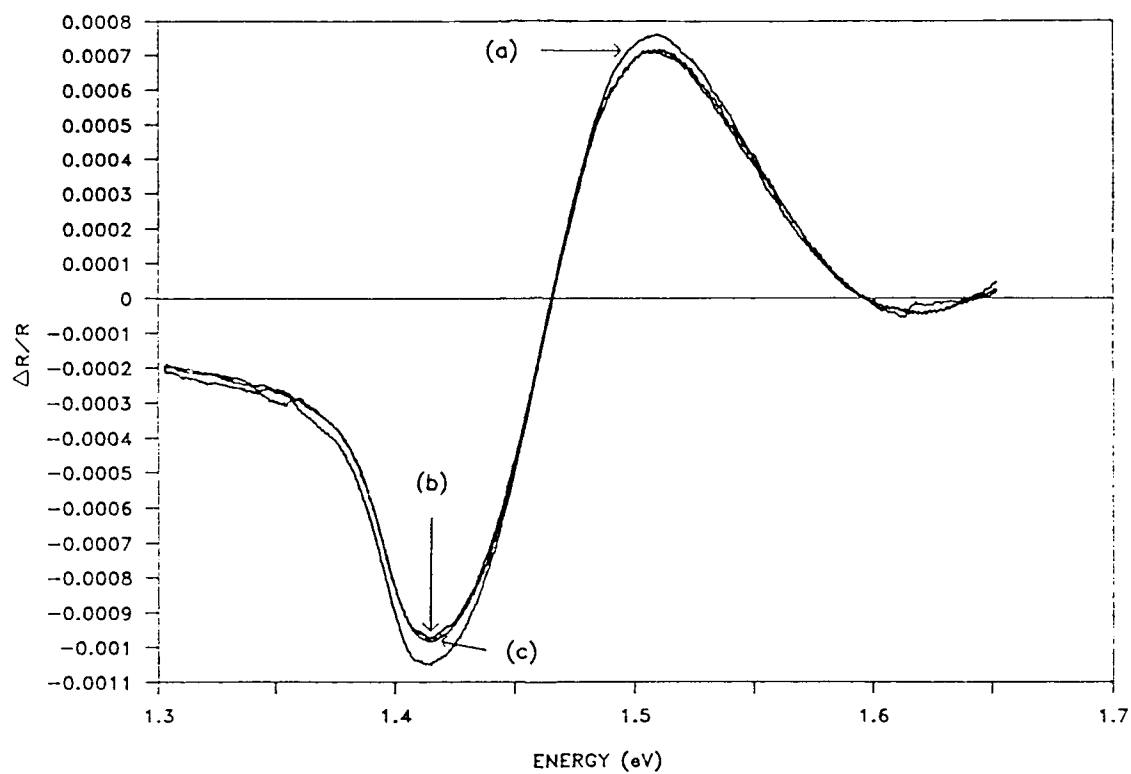


Figure 23. Water adsorption on sample C (annealed only) at 250K before adsorption (a), after 0.1 m Torr for 15 minutes (b), and following 1.0 m Torr for 2 hours (c).

the water.

The hydrogen ( $H_2$ ) plasma caused dramatic changes in the PR lineshape. Typical PR spectra of sample C at room temperature before and after a  $H_2$  plasma/anneal sequence are shown in Figure 24. Before the hydrogen plasma, the PR spectrum displayed two prominent extrema, one negative and one positive, and the possible shaping of a third one. Following the  $H_2$  plasma and subsequent anneal, four peaks are evident. The first extremum, which is the first negative peak, had degraded to the point where it is no longer considered as an extremum in the hydrogen plasmaed spectrum. The positive extremum has become huge for a PR signal, increasing to over three times its original size, well into the  $10^{-3}$  range, and the other peaks that entered the spectrum clearly show the Franz-Keldysh oscillations. The linewidth (spacing between peaks) has considerably narrowed, yielding much sharper structure of the  $E_0$  critical point.

A difficulty arose in attempting to achieve reproducible spectra following each hydrogen plasma. The peak amplitude varied by as much as 5% or more following each  $H_2$  plasma/anneal sequence. This was unacceptable for adsorption comparison studies where a low as a 2% change in PR signal after adsorption would need to be detected. Additionally, the linewidth continued to slightly narrow following each  $H_2$  plasma, and the peak amplitudes began to irreversibly degrade after more than about twenty strong intensity  $H_2$  plasmas. Performing the hydrogen plasma near the sample where the ion gauge is located or farther away from it on the electrical feedthrough (Refer to Figure 8)

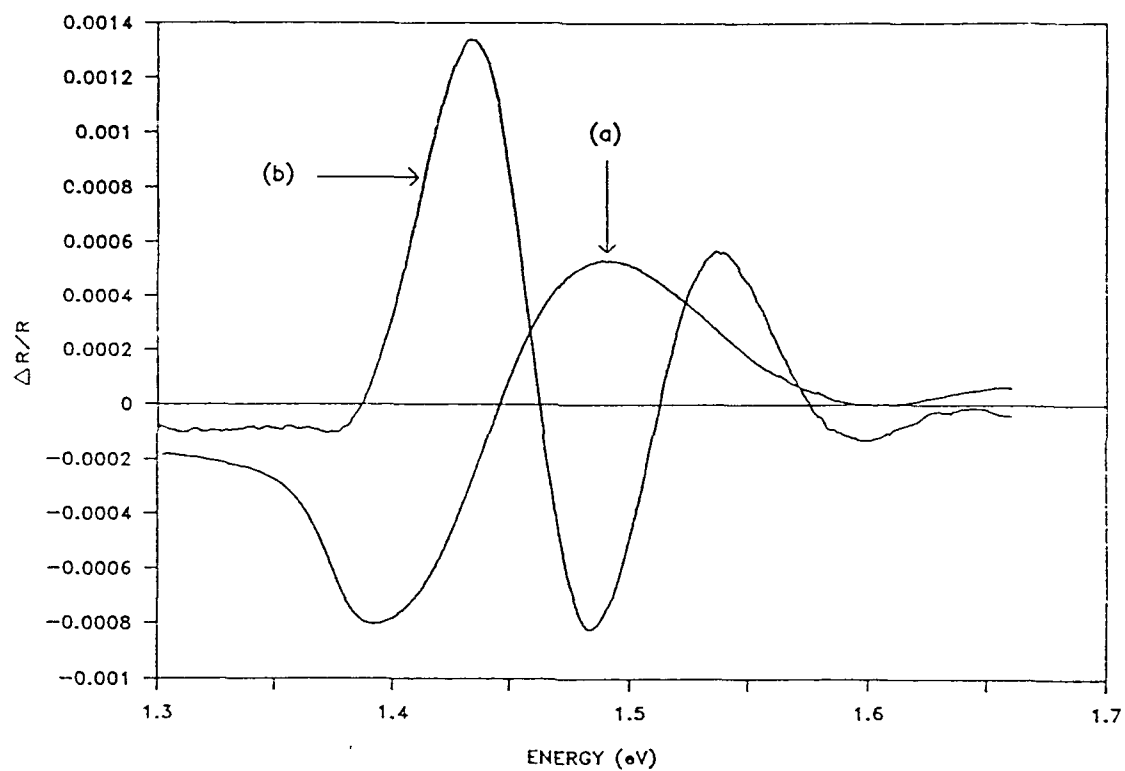


Figure 24. Effect of  $H_2$  plasma etch on sample C: before  $H_2$  plasma (a), and after  $H_2$  plasma/anneal sequence (b).

yielded similar results. The only difference was that the H<sub>2</sub> plasma conducted close to the sample caused the linewidth to narrow more rapidly, and peak degradation to begin more quickly. The intensity of the H<sub>2</sub> plasma and whether or not the sample was grounded also impacted on the  $\Delta R/R$  signal. The same results as those just stated were achieved with either a high intensity hydrogen plasma or grounding of the sample. Two examples of H<sub>2</sub> plasma effects are shown in Figure 25, where a medium intensity H<sub>2</sub> plasma is used near the sample, and Figure 26, where a low intensity plasma was performed away from the sample.

The differences between an AC hydrogen plasma from the tesla coil, and a DC hydrogen plasma using a DC power supply were also studied. Both AC and DC H<sub>2</sub> plasmas were performed next to, and away from the sample, and with varying intensities. The DC H<sub>2</sub> plasma appeared to be more uniform than the AC H<sub>2</sub> plasma. Results indicated that both types of H<sub>2</sub> plasma were unable to achieve steady-state, as a slight linewidth narrowing always occurred, and peak heights usually fluctuated by 2% or more in the PR spectra. Of interest, is the fact that each type of H<sub>2</sub> plasma yielded a slightly different signal as seen in Figure 27. This may be accounted for by the fact that the DC H<sub>2</sub> plasma appeared to cause the PR spectra to narrow much more quickly, and degradation of peak amplitudes began sooner than with the AC H<sub>2</sub> plasma. Though steady-state was never completely achieved following H<sub>2</sub> plasmaing, the PR spectra changes were eventually reduced following H<sub>2</sub> plasma sequencing to a level where

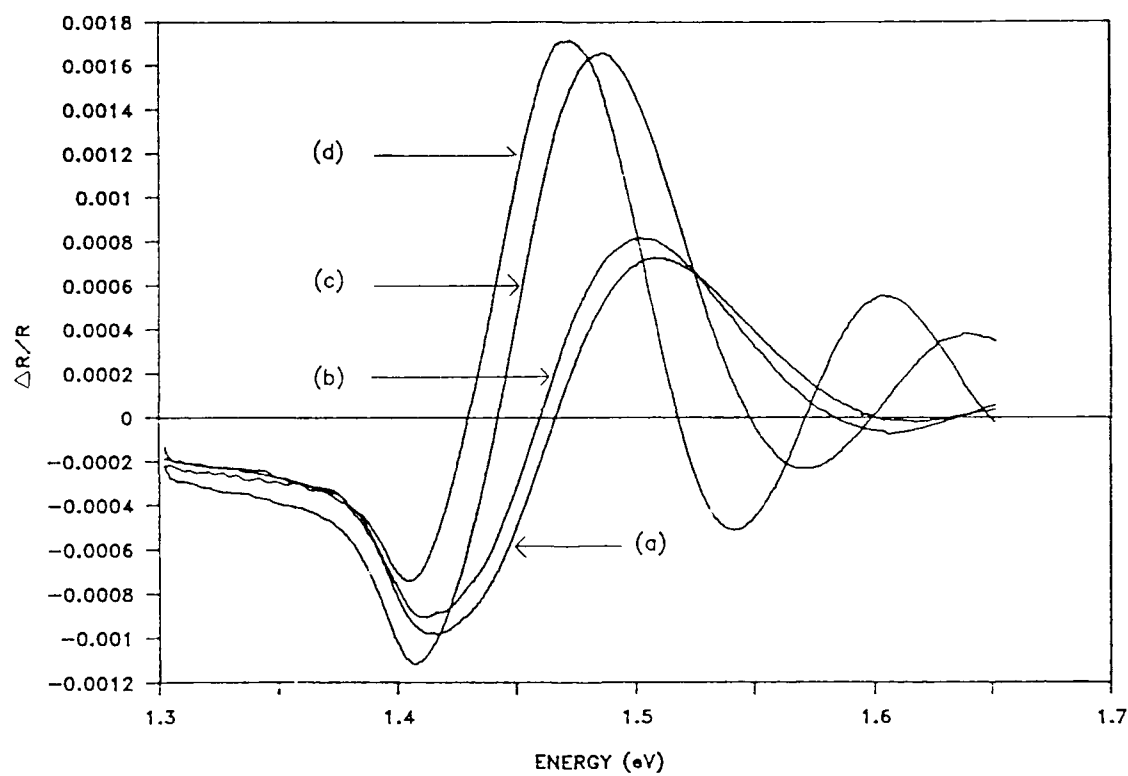


Figure 25. Medium intensity  $H_2$  plasma effect on sample C at 250K following five  $H_2$  plasma/anneal sequences: before plasma (a), after plasma #1 (b), after plasma #3 (c), and after plasma #5 (d).



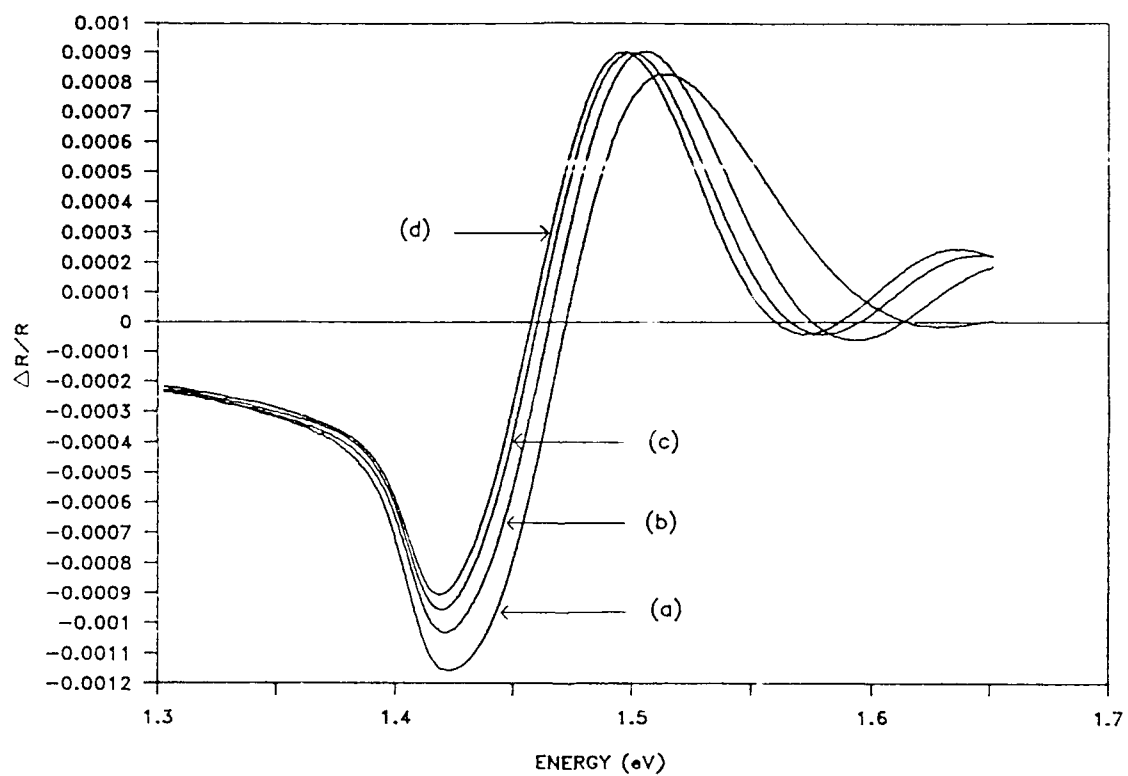


Figure 26. Low intensity  $H_2$  plasma effect on sample C at 225K after six  $H_2$  plasma/anneal sequences: before plasma (a), after plasma #1 (b), after plasma #3 (c), and after plasma #5 (d).

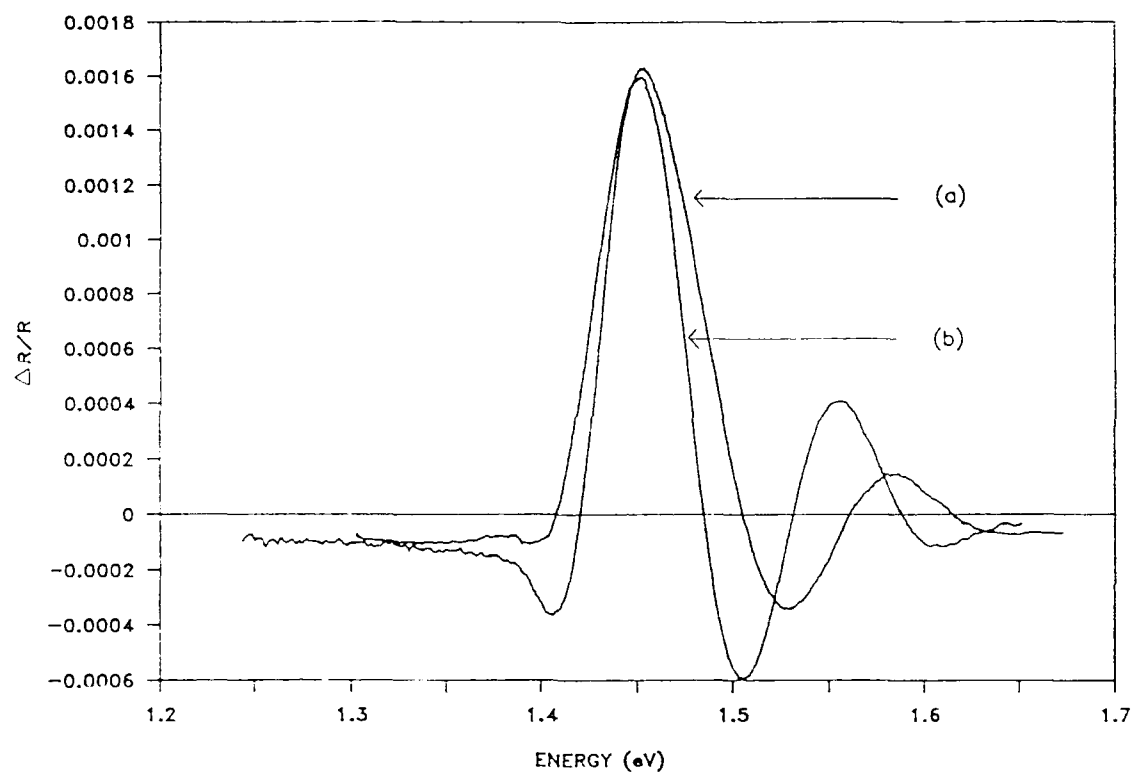


Figure 27. Comparison of AC and DC H<sub>2</sub> plasma effects on sample C at 250K: DC plasma (a), and AC plasma (b).

qualitative adsorption studies could be performed.

Temperature studies on a hydrogen plasmaed sample at 220K, 250K, and 298K yielded results consistent with those of previous work[7,13,14]. As shown in Figure 28, the 298K spectrum was slightly larger in amplitude than the 250K one, and both were about 5% larger than the 220K spectrum. The linewidth displayed broadening from lower to higher temperatures.

Prior to adsorption studies, it is important to determine how quickly the sample surface degrades with ambient contaminants following cleaning. These effects should be minimized by operating at UHV. Following a hydrogen plasma/anneal sequence cleaning, it was determined that 99.5% of the original  $\Delta R/R$  signal of sample C was reproduced after two hours.

Water adsorption studies performed on a  $H_2$  plasma cleaned sample yielded inconsistent results. Water was adsorbed at various pressures at 225K, 250K, and 275K, causing less than a 3% change in any of the PR spectra. A slight broadening was observed in those spectra where any change was recorded. An example of these slight variations in the PR spectra on the adsorption of  $10^{-6}$  torr and  $10^{-4}$  torr of  $H_2O$  at 225K is shown in Figure 29. Adsorption of  $10^{-2}$  torr of  $H_2O$  generally produced the same effect of increasing the signal amplitude only marginally at each of these temperatures. It is not clearly understood why the signal increased instead of decreased as reported by Seebauer[28]. Possibly a cleaner surface was generated since Seebauer[28] since he did

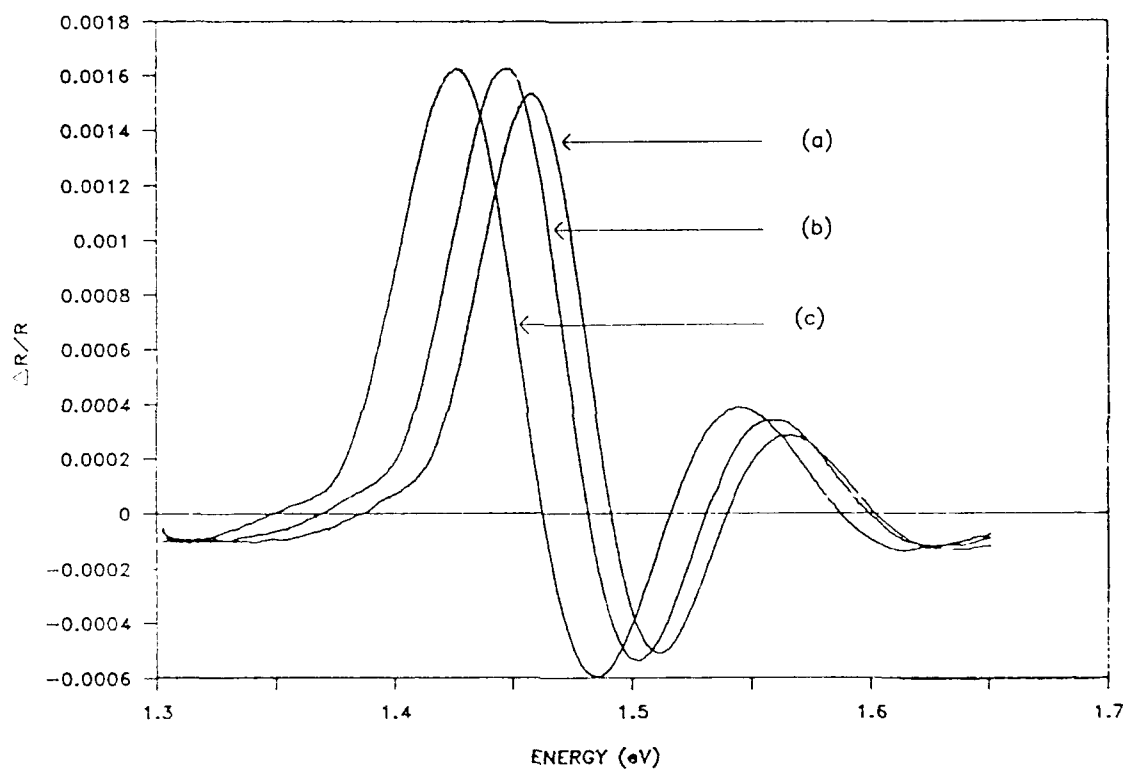


Figure 28. Sample C spectra at different temperatures following a  $H_2$  plasma/anneal sequence: 220K (a), 250K (b), and 298K (c).

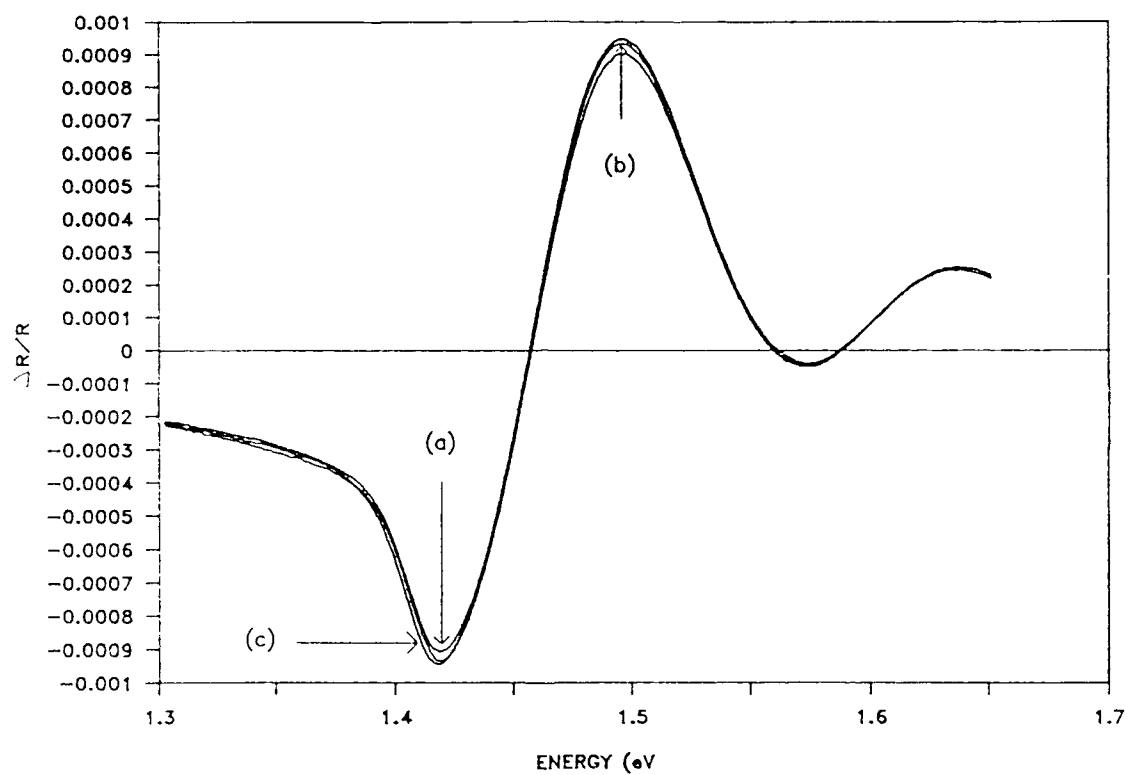


Figure 29. Water adsorption on sample C at 225 following a  $H_2$  plasma/anneal sequence: before adsorption (a), after adsorption of  $10^{-6}$  torr for 10 minutes (b), and after adsorption of  $10^{-4}$  torr for 10 minutes (c).

not use any method to remove the carbon contaminants, resulting in the water physisorbing on the GaAs surface in a manner which provided a slightly higher  $\Delta R/R$  signal. Confirmation of this is beyond the PR system capability. Another possibility, is that the density of surface states is extremely large on the sample, so the water cannot sufficiently alter them. It is important to note that the water did not appear to desorb following a return to UHV, possibly indicating that adsorbed water had somehow bound to the surface. This type of irreversibility precluded any determination of a change in the heat of adsorption. The water was desorbed though upon anneal, yielding spectra identical to the preadsorbed ones.

#### **5.1.4 PR of sample D**

The fourth sample studied was p-type, Zn doped GaAs(100), with a  $2.1 \times 10^{18} \text{ cm}^{-3}$  doping concentration. A p-type sample was chosen for study since it has the Fermi level located closer to the valence band, whereas in a n-type sample it is closer to the conduction band. It was hoped that keeping the Fermi level lower in the space charge region, would reduce the quantity of surface states that had been possibly hampering n-type water adsorption studies.

A typical PR spectrum of a new acid etched, room temperature sample is shown in Figure 30. Three extrema are present, two negative and one positive, with the second and third extrema being 15% and 20% smaller than the first negative lobe respectively. An anneal to 550°C to remove the passivation oxide layer resulted in almost a 300%

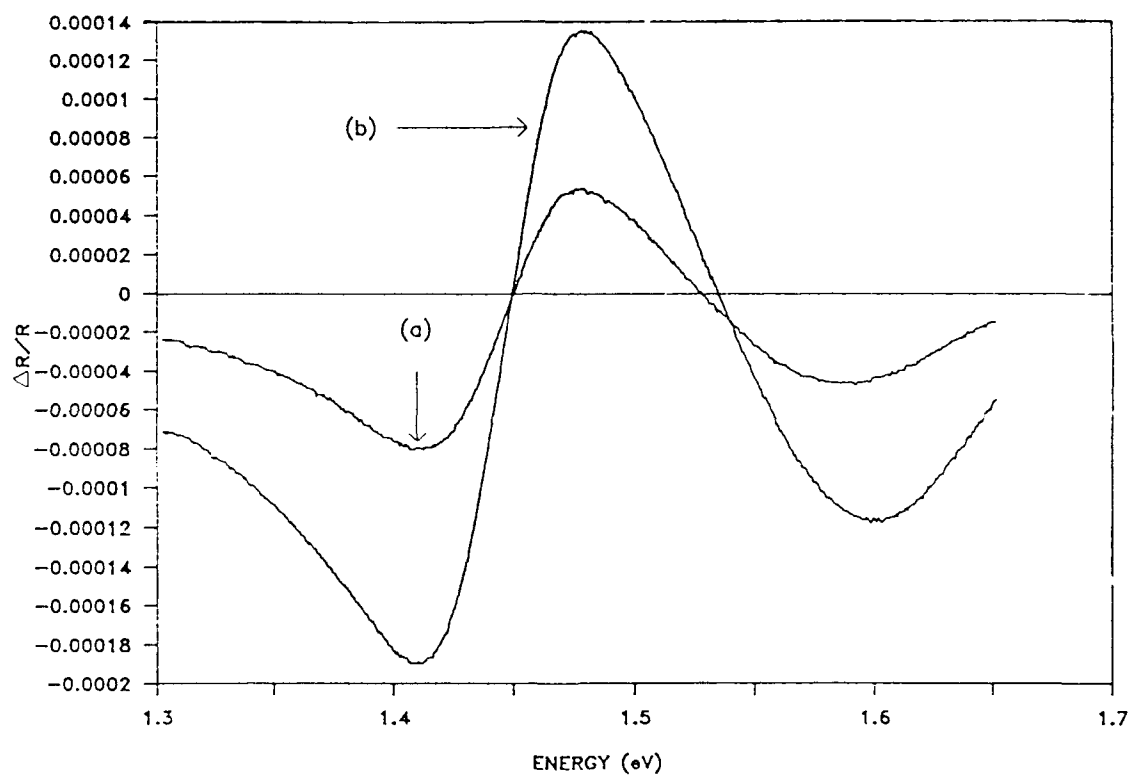


Figure 30. Typical spectra of sample D at 298K before (a) and after anneal (b).

increase in the PR signal as also seen in Figure 30. A corresponding increase in photoluminescence occurred, possibly denoting a more clean surface.

Sample D was studied over a temperature range of 135K to 395K. PR signals above 400K were too small in amplitude for adequate adsorption studies. The length of time required to cool the sample down following the H<sub>2</sub> plasma cleaning procedure precluded experiments below 135K, as it took 15 minutes to cool the sample down. Further cooling required an even longer period since cooling was performed using conduction through the electrical feedthrough in the liquid nitrogen cryostat, and it was determined that the sample surface would become too degraded to carry out quantitative PR studies. A sequence of PR spectra of sample D with thirteen different temperatures is revealed in Figures 31 and 32. These spectra were generated using an acid etched sample, which had undergone a H<sub>2</sub> plasma/anneal cleaning sequence. The  $\Delta R/R$  signal is observed to increase almost two orders of magnitude from  $3.0 \times 10^{-6}$  at 395K, to  $1.05 \times 10^{-4}$  at 135. The linewidth narrowed 15% over this temperature range, and the lineshape shifted to higher energies as the temperature decreased, in agreement with the research of others[7,13,14]. Also, the photoluminescence increased with decreasing temperature, as was expected.

The spring-loaded thermocouple at the back of the sample did not always provide the correct temperature reading. This was not a problem, however; since PR conveniently provides a method for determining accurate sample temperatures. By the method



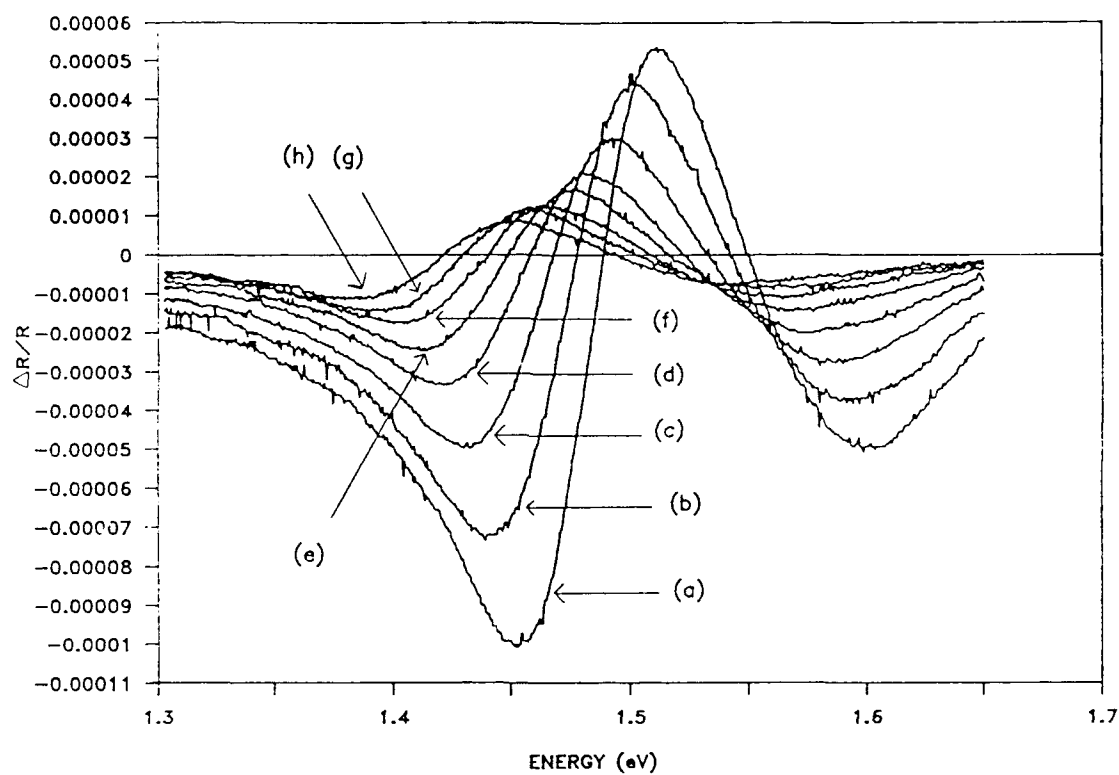


Figure 31. Acid etched,  $H_2$  plasmaed and annealed sample D spectra below room temperature: 135K (a), 165K (b), 190K (c), 215K (d), 240K (e), 260K (f), 280K (g), and 295K (h).

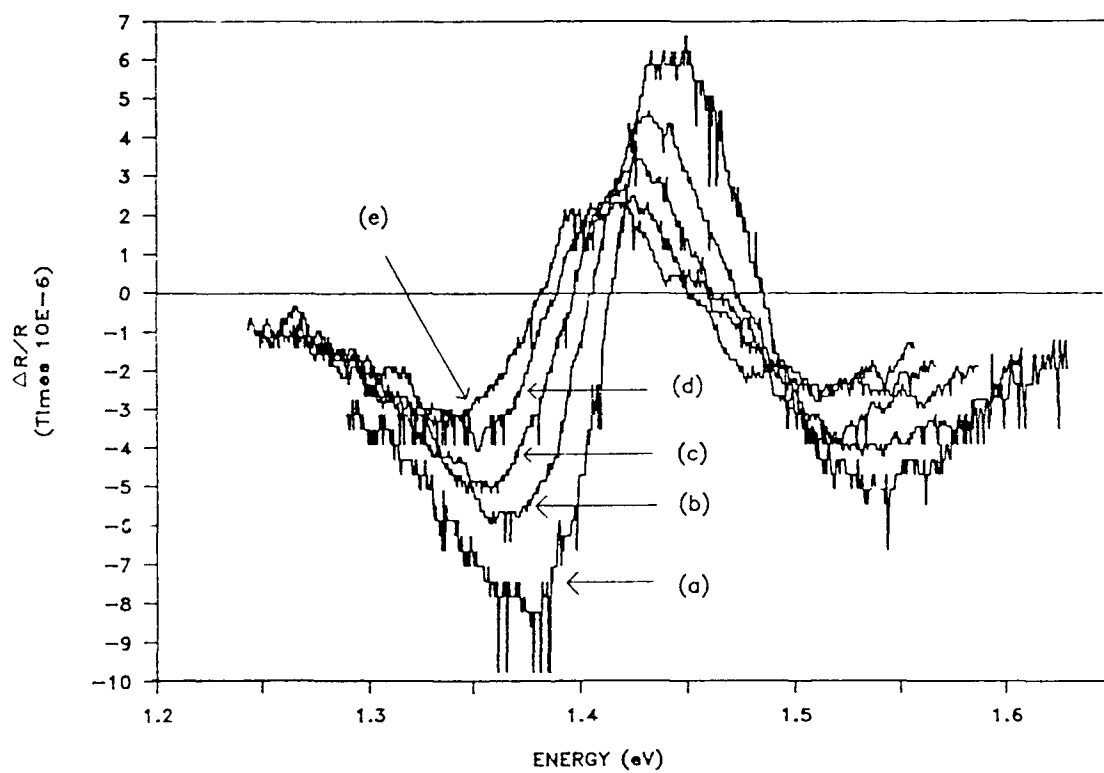


Figure 32. Acid etched,  $H_2$  plasmaed and annealed sample D spectra above room temperature: 310K (a), 325K (b), 345K (c), 370K (d), and 395K (e).

developed by Thurmond[12], the following empirical formula,

$$T(K) = \frac{1}{10.81 \times 10^{-4}} \left[ (1.519 - E_g) + [(1.519 - E_g)^2 + 0.4410(1.519 - E_g)]^{1/2} \right] \quad (45)$$

could be used. The  $E_g$  of GaAs was known as 1.424 eV at room temperature, so using a room temperature reference spectrum, the  $E_g$  of the suspect spectrum could be obtained. Placement of this fundamental band gap value in equation (45) above yielded the temperature.

For comparison purposes, adsorption studies were performed on sample D both with and without hydrogen plasma etching. In this manner, the effects of the carbon contamination left on the surface of the sample without the  $H_2$  plasma could be qualitatively observed. Following an anneal, the sample was observed to degrade less than 5% in thirty-five minutes. Water adsorption was performed at various temperatures, yielding similar results. The 220K,  $H_2O$  adsorbed spectra are displayed in Figure 33 (a). Over 95% of  $H_2O$  was found to adsorb in the first two minutes. Equilibrium was completely achieved within fifteen minutes. The  $\Delta R/R$  signal was reduced by about 35%, 55%, and 75%, with 0.1 mTorr, 1.0 mTorr, and 10 mTorr of water respectively. In Figure 33 (b), the results obtained at room temperature (298K), indicate that the PR signal is degraded by 20%, 40%, and 70% with  $10^{-4}$  torr,  $10^{-3}$  torr, and  $10^{-2}$  torr of water respectively. The linewidth narrowed slightly, and the original signal could be obtained upon reanneal, indicating surface desorption at high temperatures. The  $H_2O$  desorbed less

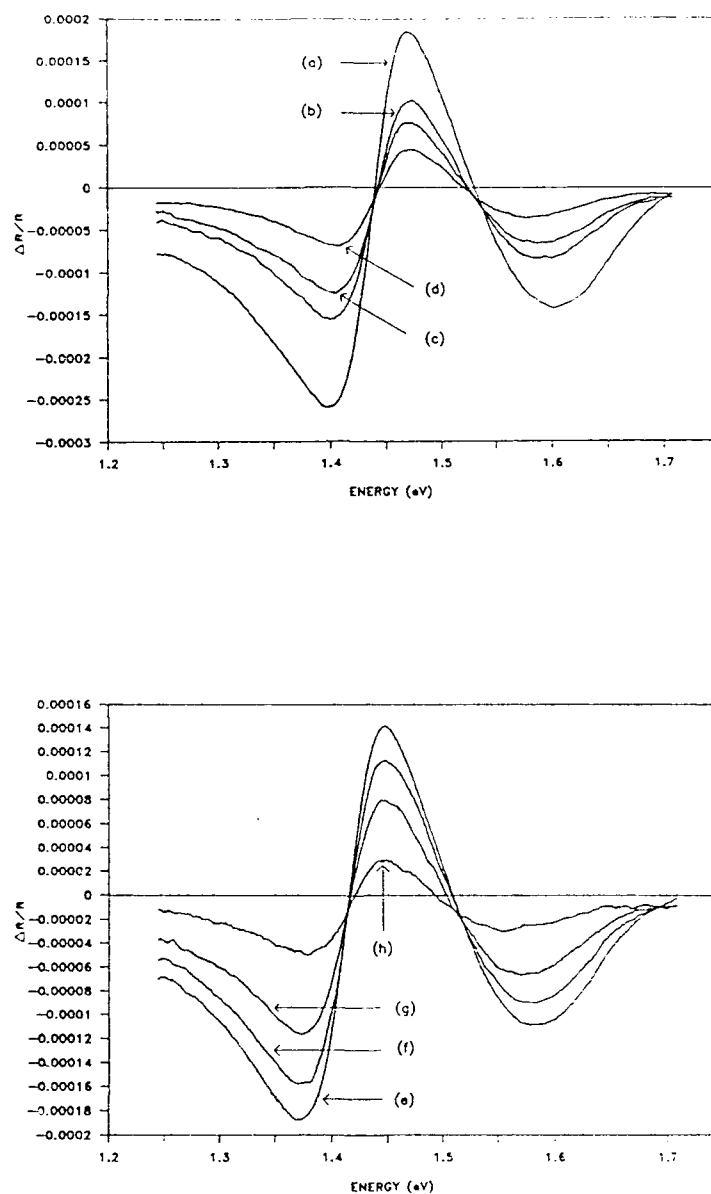


Figure 33. Water adsorption for 15 minutes on sample D (annealed only). At 220K, before adsorption (a), 0.1 mTorr adsorption (b), 1.0 mTorr adsorption (c), and 10 mTorr adsorption (d). At 298K, before adsorption (e), 0.1 mTorr adsorption (f), 1.0 mTorr adsorption (g), and 10 mTorr adsorption (h).

than 5% from the various operating pressures though when achieving UHV, which meant that the water bound tightly to the GaAs molecules. A significant reduction in signal was reported by Seebauer[28], however; he also reported reversibility of the adsorption when the sample was returned to UHV.

Hydrogen plasma studies were conducted on the sample in an effort to achieve reproducible PR spectra. Both AC and DC H<sub>2</sub> plasmas were observed. A dramatic change in lineshape was initially observed, however; it was later revealed that the lineshape change had been caused by some form of interaction with H<sub>2</sub> etched copper atoms from the copper sample mount. The sample D spectra was somehow narrowed by this procedure, other peaks appeared, and the peak amplitude tripled. Since another type of stainless steel sample mount had been used with all n-type samples, and no metallic residue was ever observed, this reasoning only pertains to the earlier p-type sample experiments. The AC hydrogen plasma caused more metallic deposits in the chamber and larger changes in the amplitude signals of the PR than the DC H<sub>2</sub> plasma. Also, grounding the sample intensified the H<sub>2</sub> etching effect creating an even greater amount of metal to be deposited. By using a low intensity AC or DC plasma from below the sample mount on the electrical feedthrough (Refer to Figure 8), nearly identical spectra were recorded. Hydrogen plasmas conducted in this manner only altered the peak amplitude and not the basic spectral lineshape. Consistent spectra to within 2% were obtained following successive H<sub>2</sub> plasmas. This had never before been achieved in the

current studies. The AC plasma was then used since it was more simplistic.

Before the water adsorption experiments, stability studies were performed. It was determined that a clean sample in the  $10^{-7}$  torr range degraded the PR signal amplitude by over 10% in under ten minutes, whereas a sample in the  $10^{-9}$  torr regime yielded over 95% of the original PR signal after ninety minutes. These effects are shown in Figure 34. These spectra underscore the importance of maintaining a low UHV pressure while conducting adsorption studies.

The effects of water adsorbed on sample D were initially studied on samples altered by the metallic deposit. These spectra provided results similar to those of the p-type samples without the  $H_2$  plasma. Figure 35 demonstrates the effects of  $10^{-4}$  torr and  $10^{-2}$  torr of water adsorption at 235K. These results were inconclusive, however; since the PR signal continued to decrease long after the period where equilibrium of the water and GaAs should have been attained. This can be seen in spectrum (d) of Figure 35. Other  $H_2O$  adsorption results indicated no change in the PR spectra.

As stated previously, nearly reproducible PR spectra were generated following a very low intensity AC  $H_2$  plasma initiated away from the sample. Hydrogen plasmas conducted in this manner, resulted in the signal decreasing by an order of magnitude, as shown in Figure 36. Additionally, the spectra linewidth narrowed somewhat. Previously, linewidth narrowing appeared to indicate a cleaner surface. Also, the photoluminescence increased after the  $H_2$  plasma then stabilized indicating a clean surface.

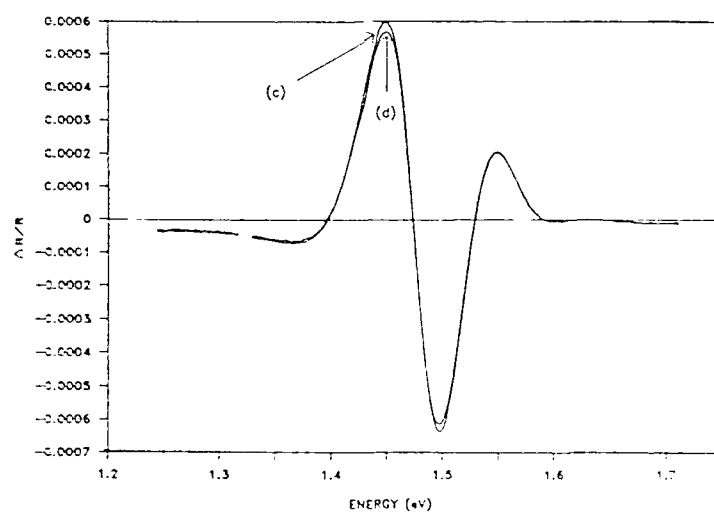
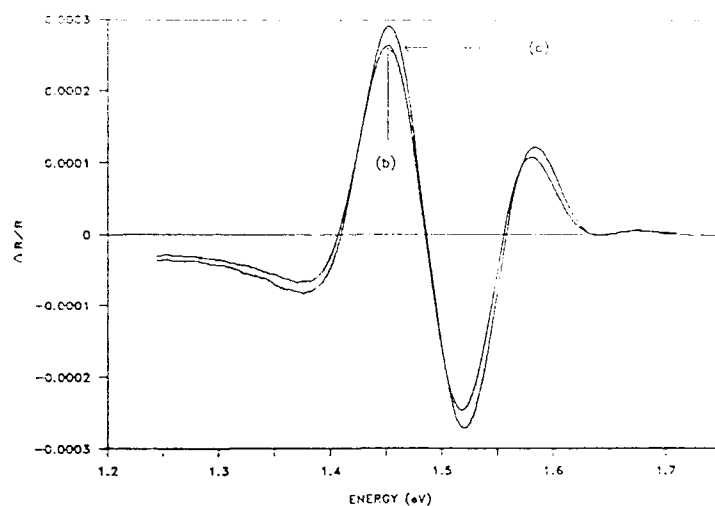


Figure 34. Sample D PR signal degradation over time. Clean sample at  $10^{-7}$  torr (a), and after 10 minutes (b). Clean sample at  $10^{-9}$  torr (c), and after 90 minutes (d).

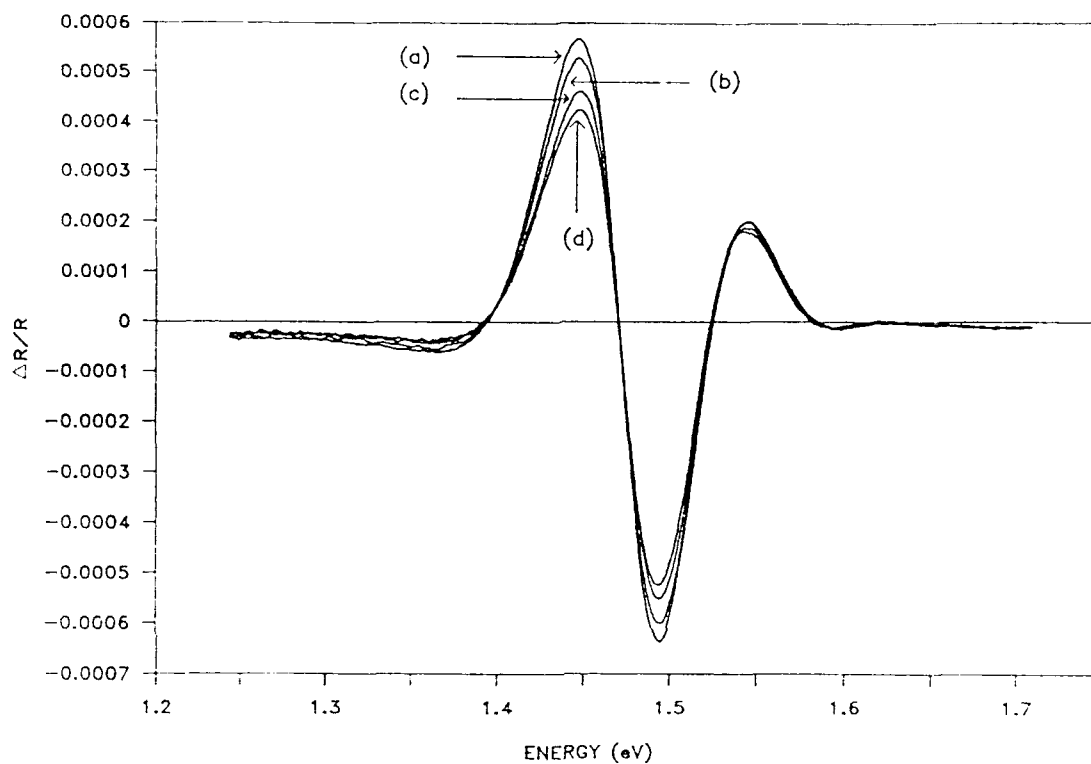


Figure 35. Water adsorption for 15 minutes on sample D at 235K following a  $H_2$  plasma/anneal sequence yielding a metallic substance: before adsorption (a), after  $10^{-4}$  torr of adsorption (b), after  $10^{-2}$  torr of adsorption (c), and continued degradation of PR signal after obtaining UHV (d).



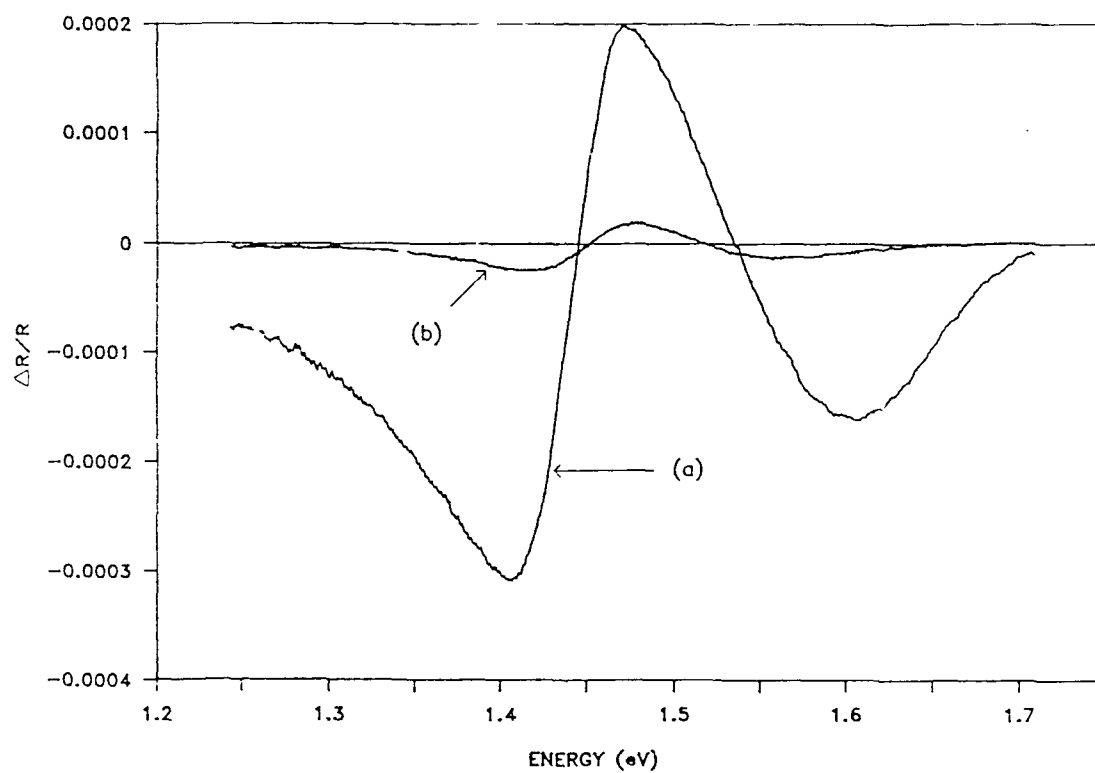


Figure 36. Effect of AC H<sub>2</sub> plasma/anneal sequence on sample D at 190K: before plasma (a), and after plasma (b).

Water adsorption studies were performed on sample D following the hydrogen plasma method where reproducible results were obtained. Water was initially adsorbed from 135K to 395K at 0.1 mTorr. It was determined that the H<sub>2</sub>O adsorbed PR signal at 240K and above was approximately the same, while the spectra at 215K, 190K, 165K and 135K were decreased by 5%, 30%, 30% and 40% respectively. These last four spectra are shown in Figure 37. Adsorption of 1.0 mTorr of water in the 135K to 295K range have the results posted in Figure 38. The spectra increased from 2% to 10% at 215K and above, then decreased 20%, 50%, and 60% at 190K, 165K, and 135K respectively. Sequential spectra of the 10<sup>-4</sup> torr and the 10<sup>-3</sup> torr H<sub>2</sub>O adsorbed spectra are shown in Figure 39. It should be noted that leaking water into the chamber when the sample was already cooled down (below 450K), produced better results than when the sample was hot (above 600K). It is unknown why this made any difference.

These qualitative water adsorption results required further analysis as there was no trend observed in how the  $\Delta R/R$  signal was changing when compared to coverage. It was expected that the adsorbed H<sub>2</sub>O would cause a decrease in the PR signal at all temperatures. It has just been demonstrated that the water adsorbed PR signal actually increased at higher temperatures. To better understand these effects, a detailed study of the change in PR and photoluminescence during the process of water adsorption was performed using a chart recorder, prior to the equilibrium PR scan.

This water adsorption experiment was conducted in the 165K to 345K temperature

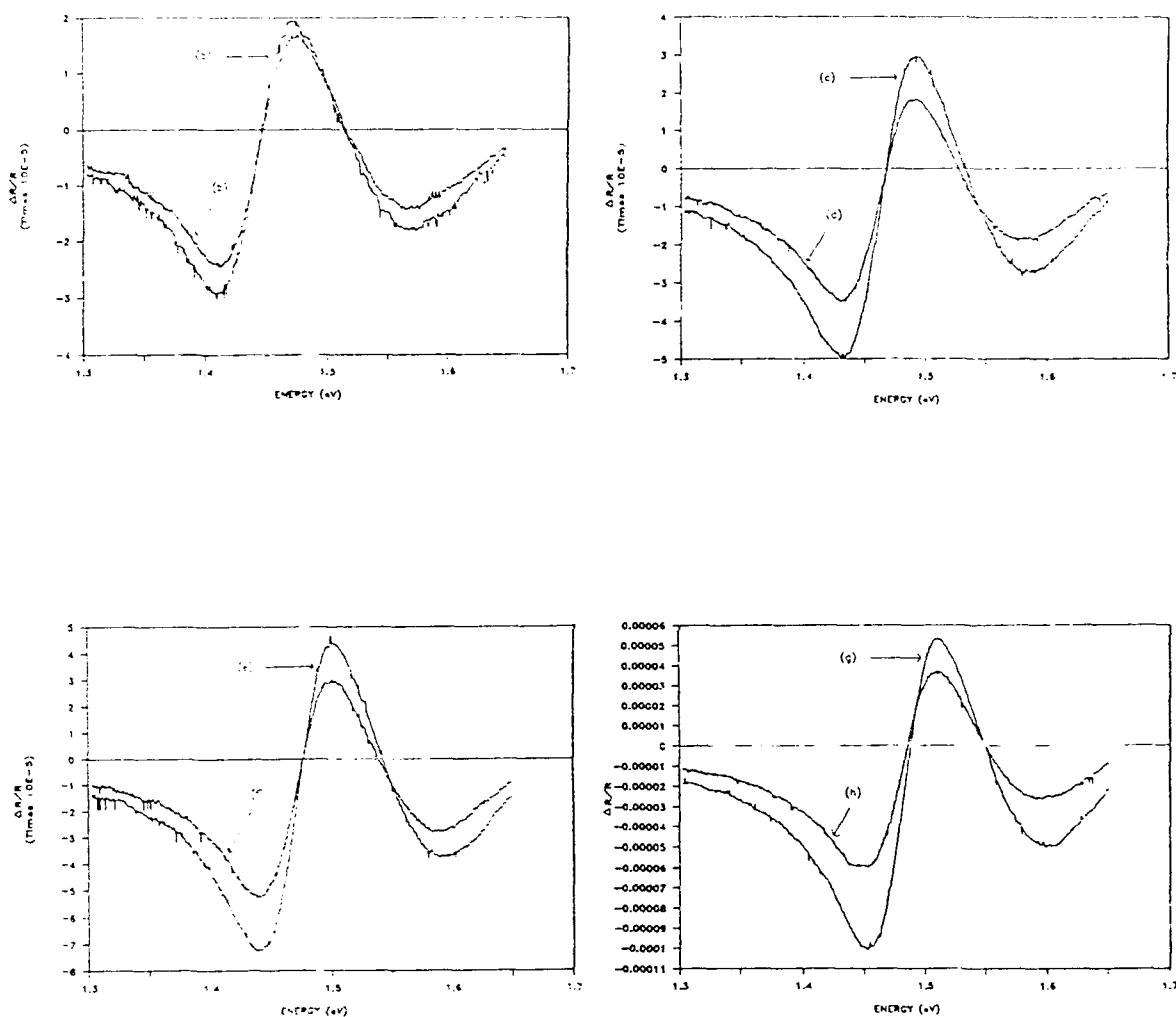


Figure 37. Water adsorption of 0.1 mTorr for fifteen minutes on sample D at various temperatures. At 215K, before (a) and after (b) adsorption; at 190K, before (c) and after (d); at 165K, before (e) and after (f); and at 135K, before (g) and after (h).

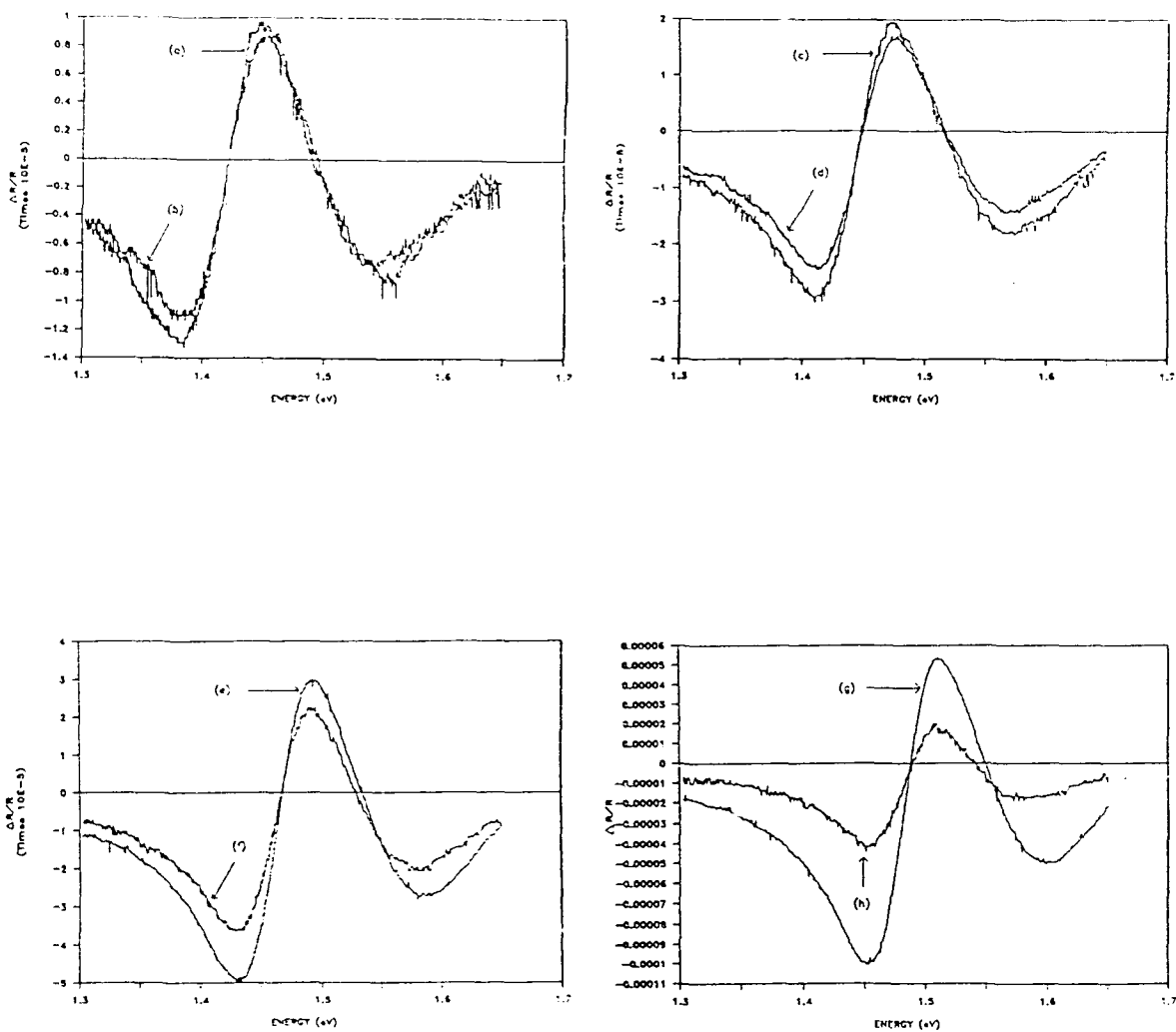


Figure 38. Water adsorption of 1.0 mTorr for fifteen minutes at different temperatures. At 295K, before (a) and after adsorption (b); at 240K, before (c) and after (d); at 190K, before (e) and after (f), and at 125K, before (g) and after (h).

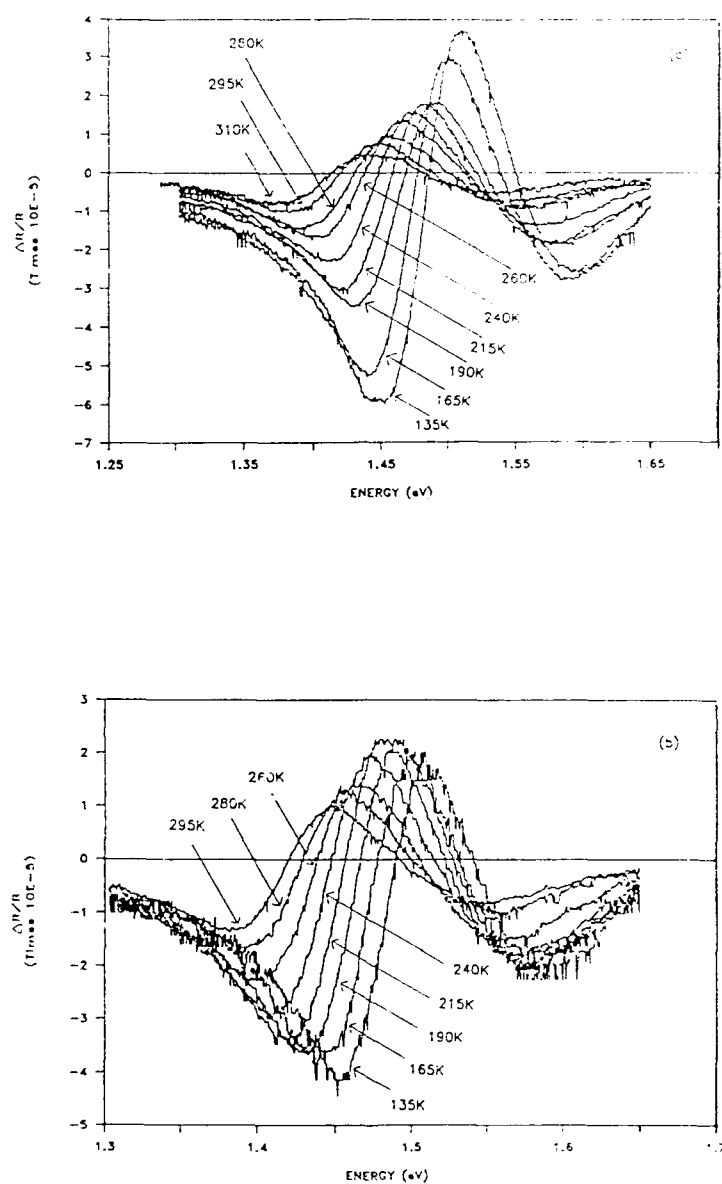


Figure 39. Sequential spectra of the water adsorbed spectra of sample D of  $10^{-4}$  torr from 310K to 135K (a), and from 295K to 135K at  $10^{-3}$  torr (b).

range, primarily with  $10^{-6}$  torr and  $10^{-4}$  torr of  $\text{H}_2\text{O}$ . It was found that 10 mTorr of  $\text{H}_2\text{O}$  created a huge ice formation on the sample mount (which was being cooled with liquid nitrogen to 77K) due to the extended experiment times. Water adsorption was observed at the first negative extremum of the PR spectrum, while photoluminescence changes were watched at 730nm (since this approximately was where  $\Delta R/R = 0$ ). It was observed that the PR signal immediately began a dramatic increase upon adsorbing the water at 10 mTorr, 0.1 mTorr and 0.001 mTorr, then the signal would decrease to a steady-state value (normally within five minutes) at temperatures 310K or below, or maintain the maximum adsorbed value at 345K. The amount of PR signal change was dependent upon the adsorption pressure used. Higher pressures of water adsorption resulted in a lower associated PR signal equilibrium spectra. The photoluminescence value decreased at the lowest temperatures (below 240K), then remained essentially constant in the center range of temperatures, and finally increased up to 3% at 280K and above.

The water adsorption effects are provided for four temperatures: 165K, 215K, 280K, and 345K. The PR signal at 165K initially increased as much as 80% upon adsorption of  $10^{-6}$  torr of  $\text{H}_2\text{O}$  as shown in Figure 40 (a), then deteriorated back to a level of about 50% of the increase, to the value yielding the PR spectrum shown in Figure 41. It also shows that the adsorption of  $10^{-4}$  torr of water yielded a 5% increase in the PR signal. The photoluminescence effect of  $10^{-6}$  torr  $\text{H}_2\text{O}$  adsorption is seen in Figure 40 (b), with its value decreasing about 5%. There was no water desorption observed from  $10^{-4}$

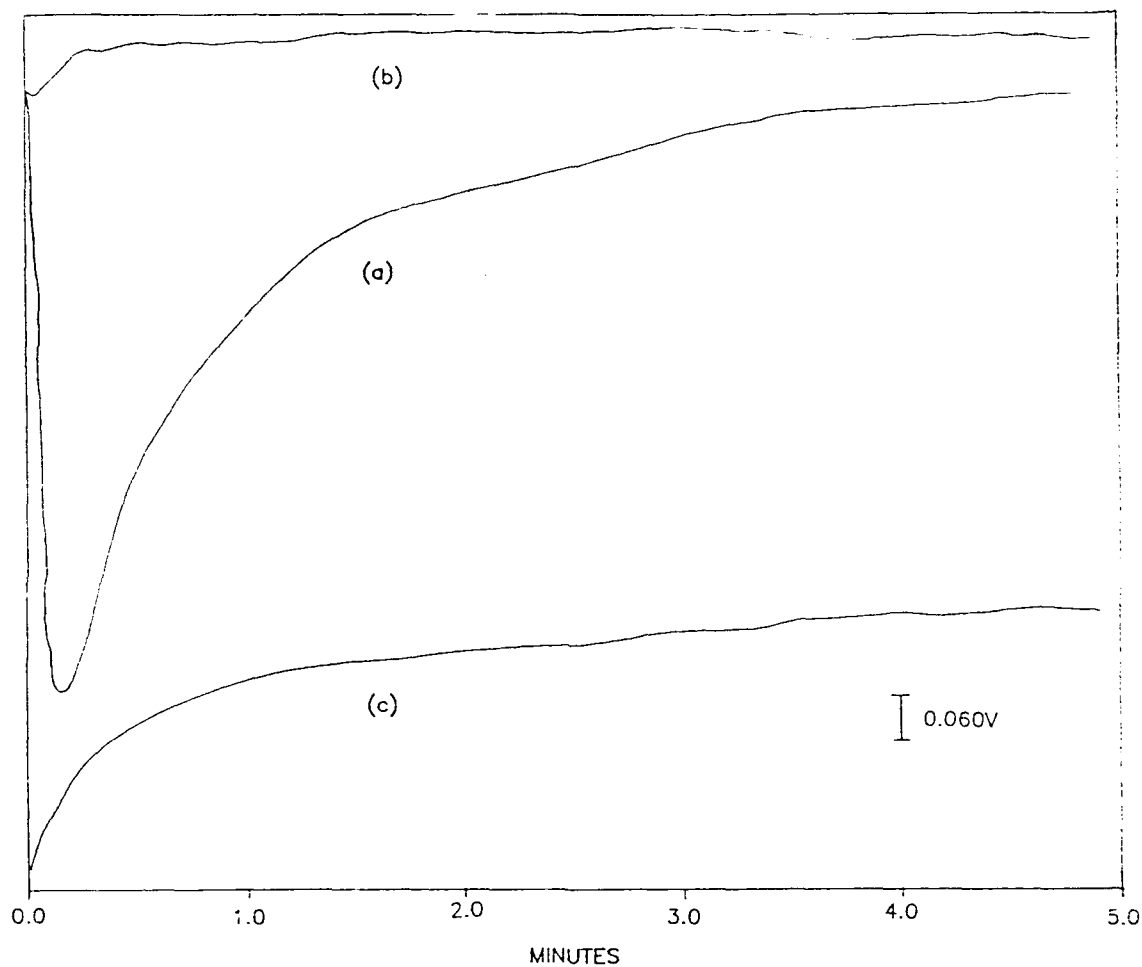


Figure 40. Water adsorption of  $10^{-6}$  torr on sample D at 165K. Change in PR signal from time zero (a), change in photoluminescence from time zero (b), and water desorption upon achieving UHV (c).

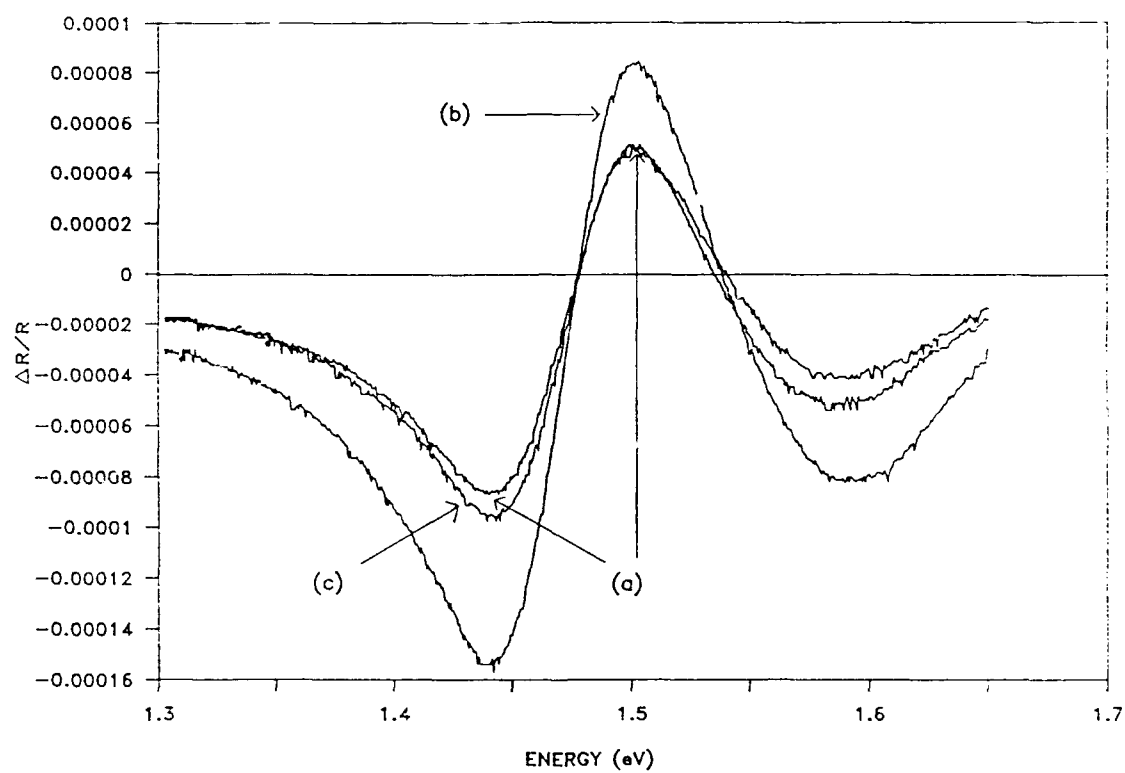


Figure 41. PR spectra of a  $\text{H}_2$  plasma/annealed sample D before (a) and after  $10^{-6}$  torr (b) and  $10^{-4}$  torr (c) of  $\text{H}_2\text{O}$  adsorption at 165K.



torr to UHV at any of the temperatures, however; at 165K the  $10^{-6}$  torr water significantly desorbed (30% of the maximum adsorption signal), indicating that the water was more weakly bound at this pressure. As depicted in Figure 40 (c), desorption equilibrium was achieved in roughly five minutes. Readsorption of  $10^{-6}$  torr of  $H_2O$  again caused the PR signal to steeply increase, then retreat to the steady-state value discussed earlier. At 215K, the adsorbed water at  $10^{-6}$  torr rapidly increased to 130% of the clean PR signal, then monotonically decreased. The associated photoluminescence decreased about 3%. There was about 20% desorption of the maximum  $10^{-6}$  torr adsorption reading, once again indicating loosely bound states in the  $10^{-6}$  torr regime. Each of these effects are pictured in Figure 42. Figure 43 contrasts the effects of  $H_2O$  adsorption at  $10^{-6}$  torr and  $10^{-4}$  torr with a clean PR spectrum. Each pressure decreases the original signal by 20% and 40% respectively. The PR signal at 280K increased almost 75% upon  $10^{-6}$  torr of water adsorption as seen in Figure 44(a), then returned to a level yielding the PR spectrum displayed in Figure 45. The photoluminescence increased around 3% as observed in Figure 44 (b), whereas previously it had decreased at 215K and 165K. The  $10^{-6}$  torr of  $H_2O$  desorbed by 15% of the maximum adsorbed value upon attaining UHV as observed in Figure 44 (c). Figure 45 displays spectral effects of the  $H_2O$  adsorption of 10 mTorr, 0.1 mTorr, and 0.001 mTorr as compared to the clean surface. These lower by 30%, 15%, and raise by 20% respectively, the PR signal. At the highest temperature observed of 345K, both the  $10^{-6}$  torr and  $10^{-4}$  torr water adsorbed signals increased the amplitude

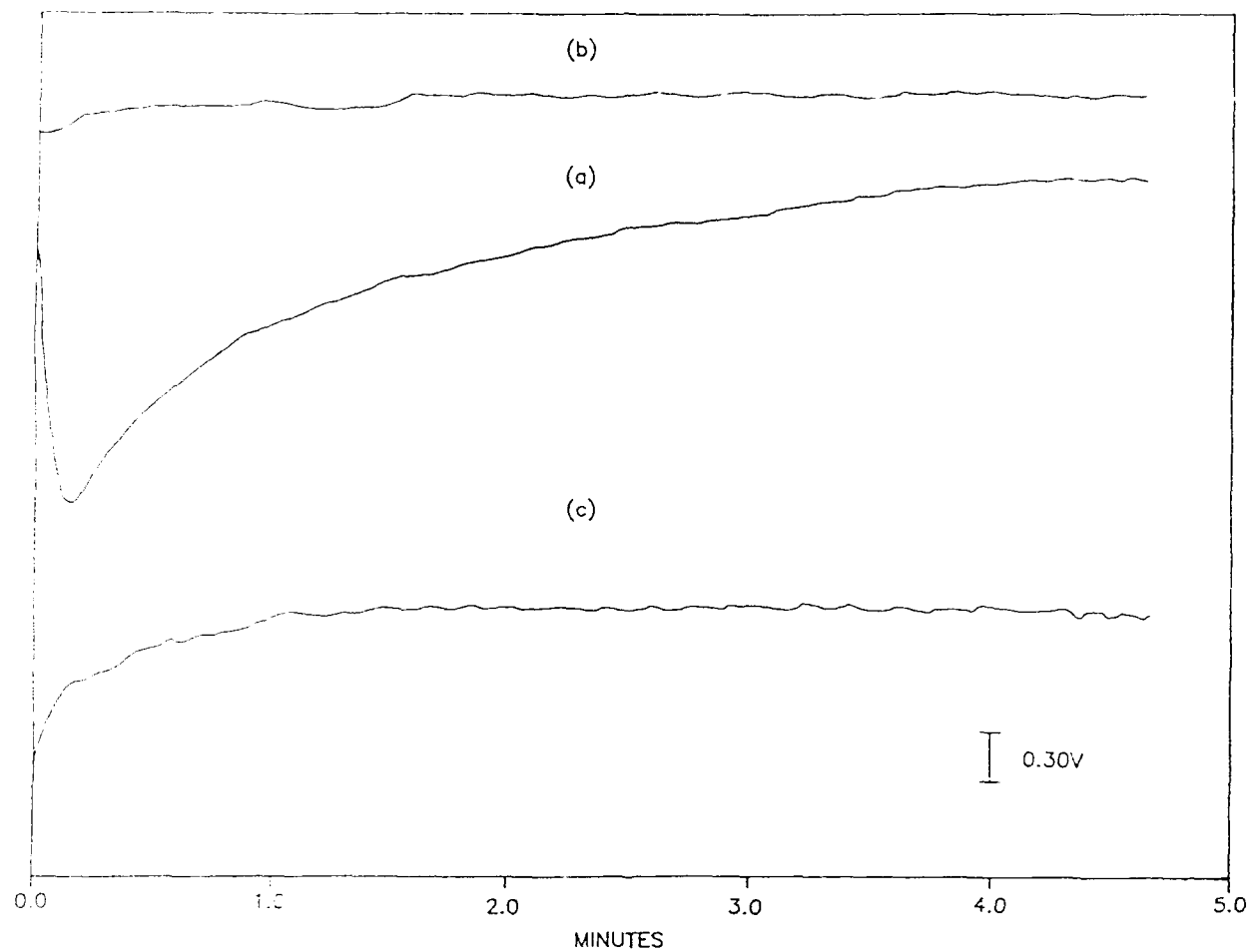


Figure 42. Water adsorption of  $10^{-6}$  torr on sample D at 215K. Change in PR signal from time zero (a), change in photoluminescence from time zero (b), and water desorption upon achieving UHV (c).

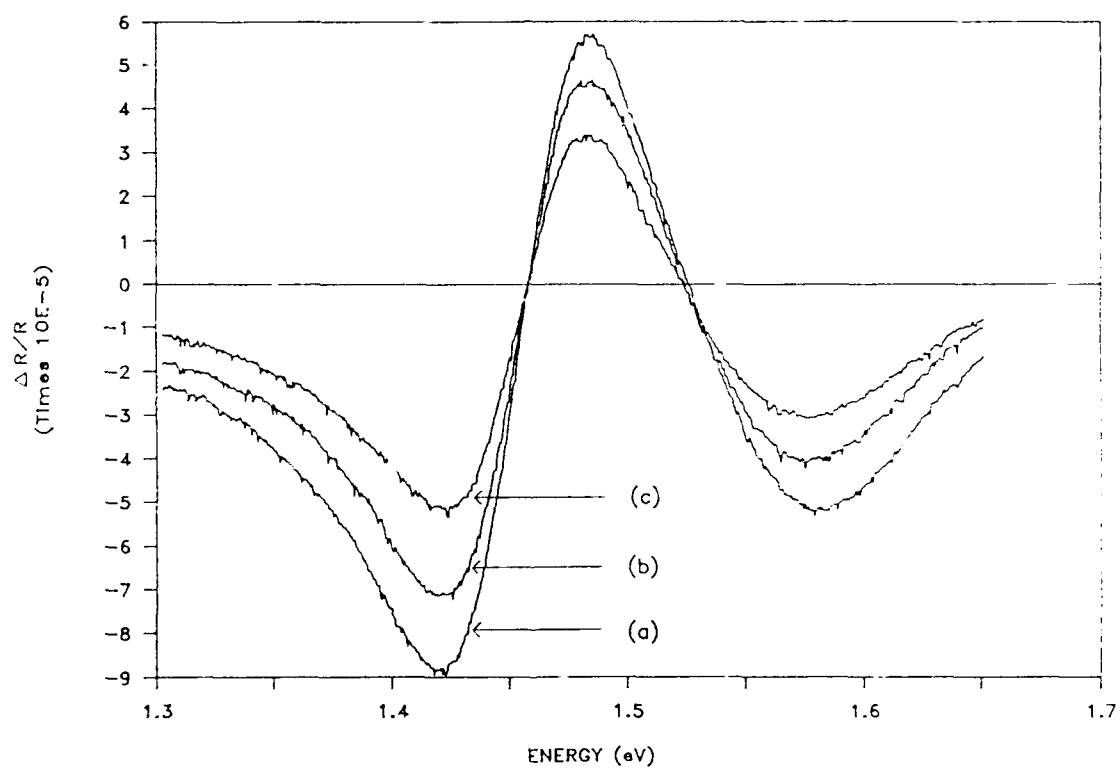


Figure 43. PR spectra of a  $H_2$  plasma/annealed sample D before (a) and after  $10^{-6}$  torr (b) and  $10^{-4}$  torr (c) of water adsorption at 215K.

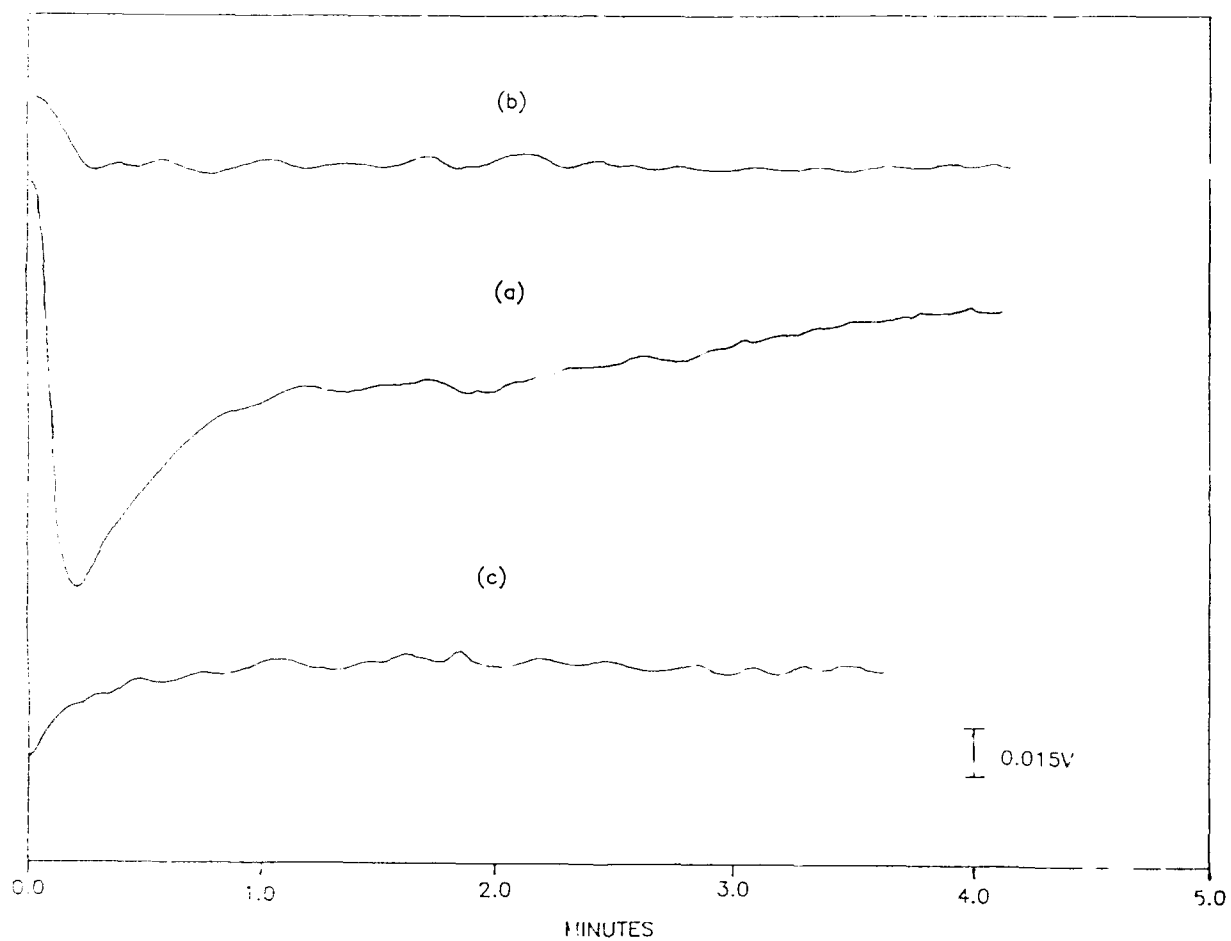


Figure 44. Water adsorption of  $10^{-6}$  torr on sample D at 280K. Change in PR signal from time zero (a), change in photoluminescence (b), and water desorption effect upon achieving UHV (c).

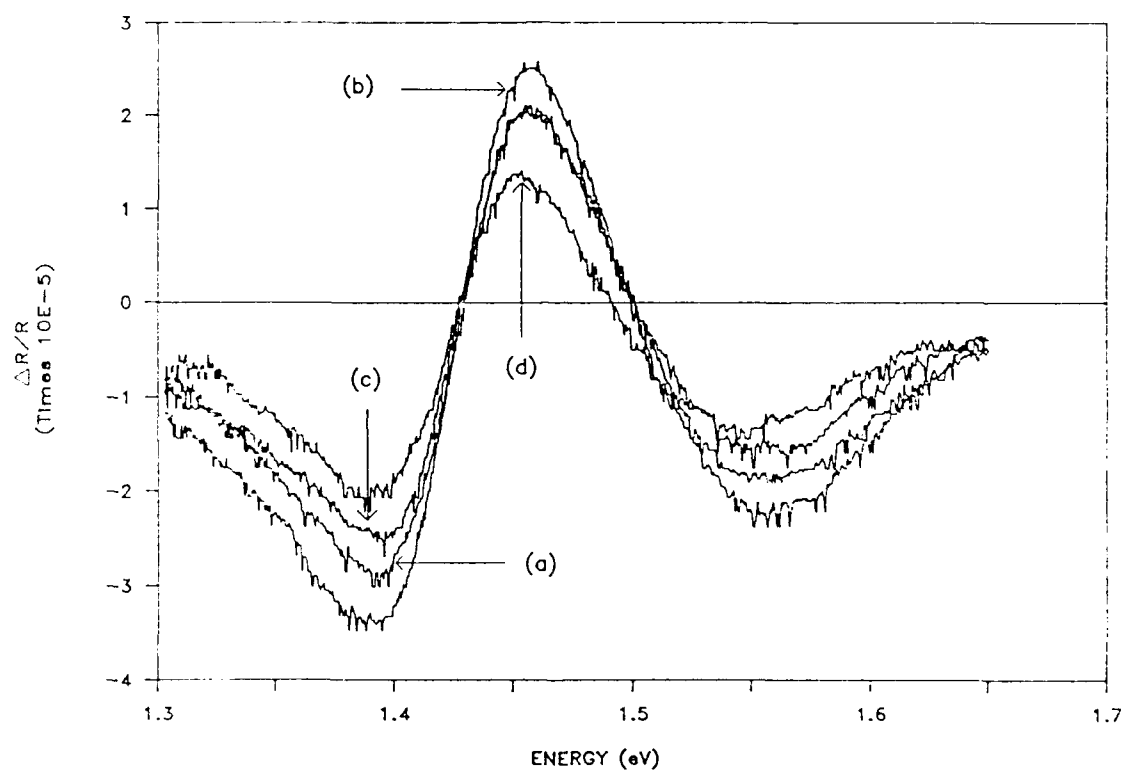


Figure 45. PR spectra of a  $H_2$  plasma/annealed sample D before (a) and after  $10^{-6}$  torr (b),  $10^{-4}$  torr (c), and  $10^{-2}$  torr (d) of water adsorption at 280K.

by roughly 20% over the original clean spectrum as seen in Figure 46. The  $10^{-6}$  torr of water adsorbed PR signal monotonically increased until achieving steady-state at a maximum value as shown in Figure 47 (a), the photoluminescence increased slightly (Figure 47 (b)), and no desorption was detected (Figure 47 (c)).

Quite different effects were noted for the annealed only, the metallically altered, hydrogen plasmaed, and the lightly hydrogen plasmaed p-type samples. The sticking coefficient appeared to be much greater for the annealed only samples, possibly due to the remaining carbon contaminants on the surface changing the characteristics of  $H_2O$  adsorption. Perhaps the metallic substance on the altered samples also served as some form of adsorption catalyst or inhibitor yielding inconsistent results. The water adsorption on the lightly  $H_2$  plasmaed p-type GaAs sample affected both the PR and photoluminescence; with the PR signal increasing at higher temperatures, and being highly dependent on the adsorbed pressure at mid-range temperatures. The water normally desorbed somewhat from the  $10^{-6}$  torr pressure, but never desorbed from the  $10^{-4}$  torr pressure.

## 5.2 Sample comparison

More insight into the characteristics of GaAs can be obtained by performing a sample comparison. The basic spectra of the four samples at room temperature are provided in Figure 48. The number of Franz-Kelysh oscillations depended upon doping concentration and sample type. The n-type spectra (samples A, B, and C) broaden with doping

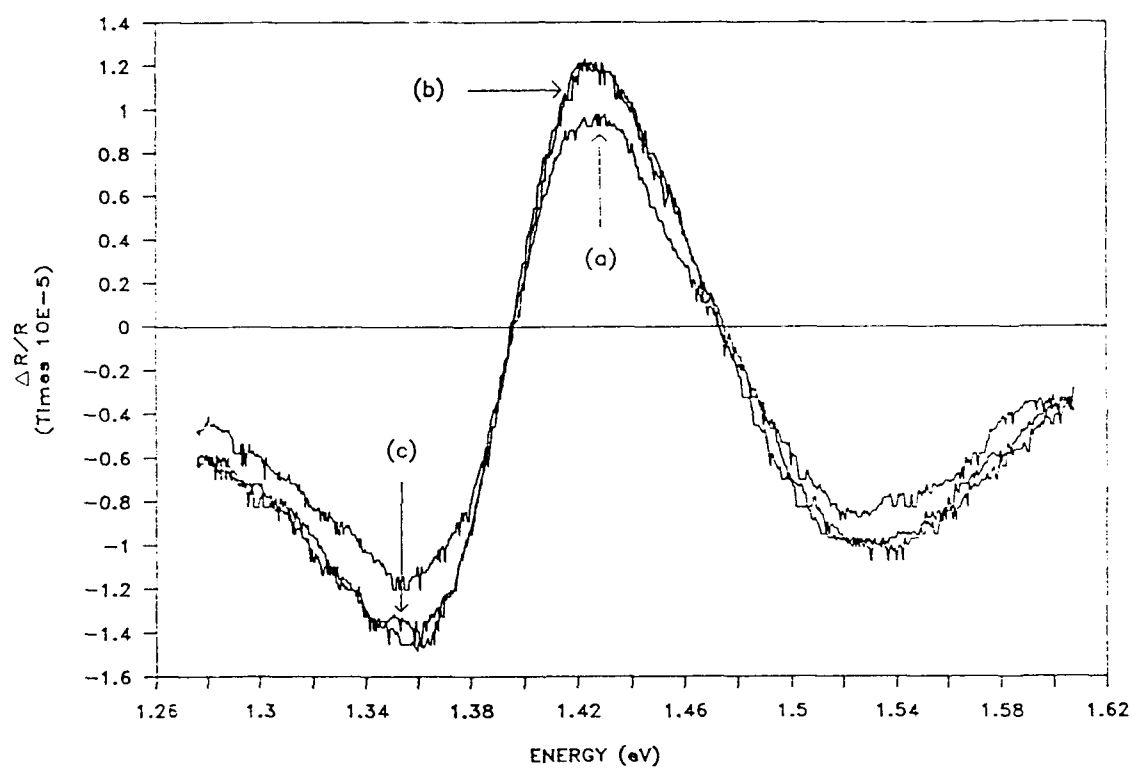


Figure 46. PR spectra of a  $H_2$  plasma/annealed sample D before (a) and after  $10^{-6}$  torr (b) and  $10^{-4}$  torr (c) of  $H_2O$  adsorption at 345K.

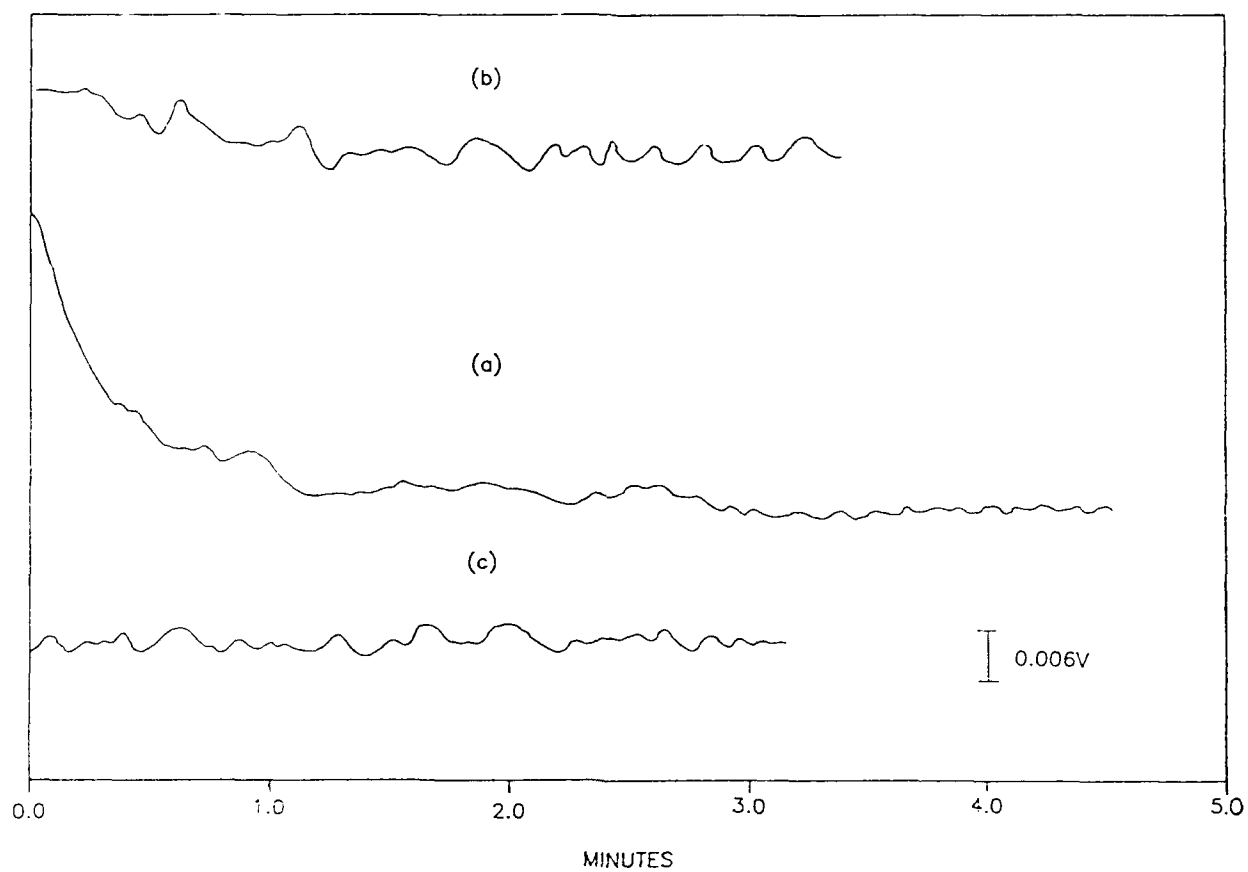


Figure 47. Water adsorption of  $10^{-6}$  torr on sample D at 280K. Change in PR signal from time zero (a), change in photoluminescence (b), and no water desorption effect (c).



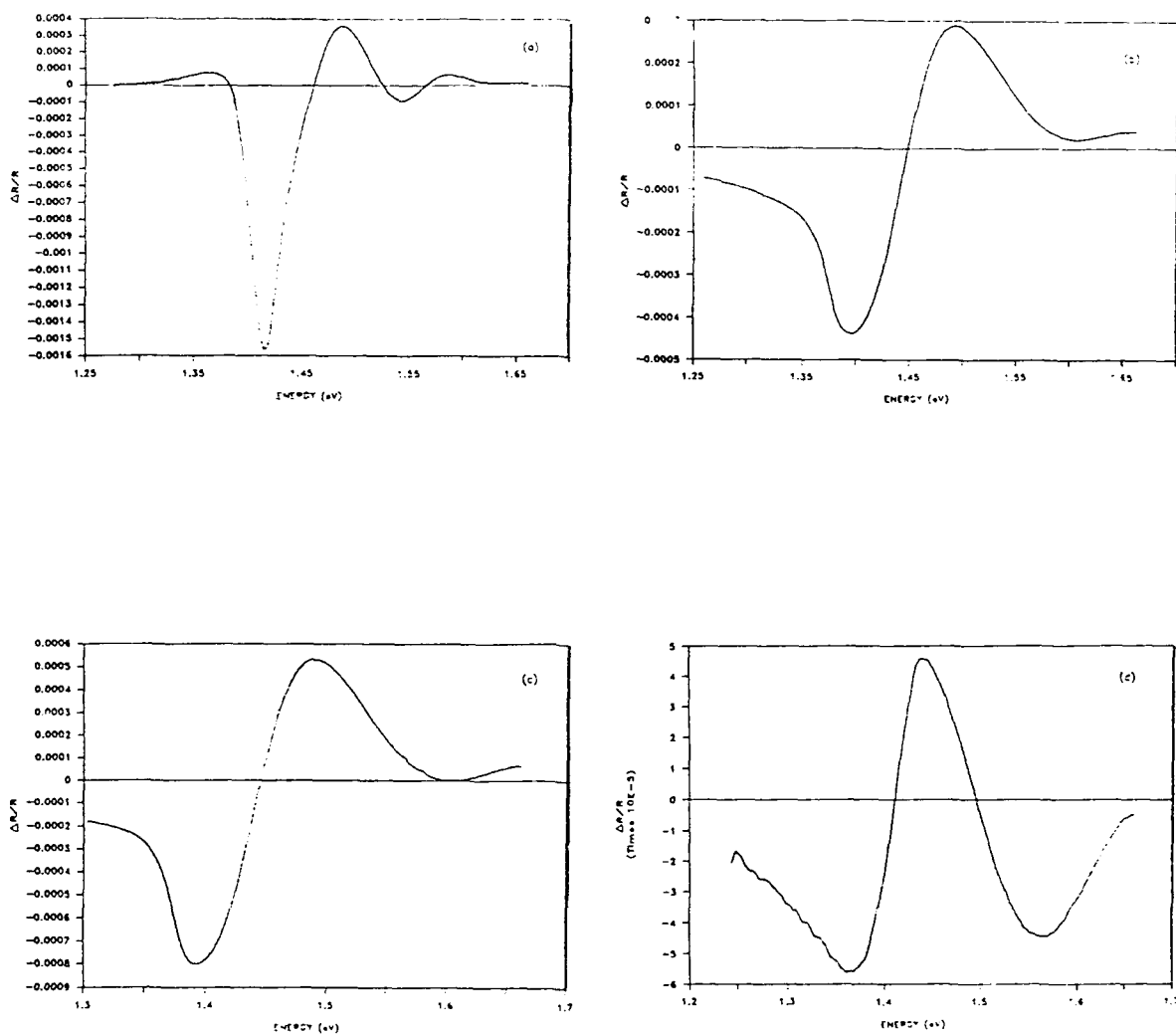


Figure 48. Room temperature PR spectra of sample A (a), sample B (b), sample C (c), and sample D (d).

concentration consistent with the results reported by others[4,7,9,10]. This broadening of the basic lineshape occurs since increasing the doping level increases the surface electric field  $\xi$ , yet decreases the depth of the space charge region (Refer to equations (37) and (38)). This in turn changes the location of  $E_0$  on the PR curve, since the Franz-Keldysh peak spacing is proportional to  $\xi^{2/3}$ .

Changing the sample temperature, corresponded to changes in the lineshape of the  $\Delta R/R$  signal in all samples. Figures 13, 16, 28, and both 31 and 32 can be referred to for samples A, B, C, and D respectively. All spectra shifted toward lower energies with increasing temperatures in agreement with other findings[7,13,14]. This shift occurs because a change in temperature changes the  $E_g$  value of the material as[12],

$$E_g(eV) = 1.519 - \frac{5.405 \times 10^{-4} T^2}{(T + 204)} \quad (46)$$

where T is in units of Kelvin. The band gap energy changes as a direct result of raising the temperature of the sample, which lowers the energy level of electron traps, making them closer to the Fermi level, and farther away from the conduction band, thereby allowing more charges to be trapped at equilibrium. Peak amplitudes varied with temperature, lowering at higher temperatures (273K and above), and then either lowered below 273K, as in samples B and C, or continued to enlarge as in sample D. The linewidth always narrowed with decreasing temperature. This was expected since lowering the temperature also decreased  $\xi$ , which again affected the Franz-Keldysh peak

spacing.

The hydrogen plasma significantly affected water adsorption on GaAs. It was extremely difficult to obtain reproducible results. The n-type samples never achieved steady-state, though relatively consistent peak amplitudes were obtained. It is not known why the signal of the n-type samples were so dramatically altered by the H<sub>2</sub> plasma. It is possible that either the Ga or As was being etched away leaving a more monolithic surface. It was beyond the scope of the PR setup to ascertain this. Also, grounding the sample greatly enhanced the etching effect, possibly damaging the surface beyond anneal repair. A low intensity plasma about eighteen inches from the sample produced the best results.

Varying effects were obtained following H<sub>2</sub>O adsorption on the sample surfaces. Sample B with the hydrogen plasma displayed a 5% or 10% increase in signal (See Figure 18) at 200K and 298K respectively. Sample C with no H<sub>2</sub> plasma yielded either no change or decreased up to 7% (Figure 23); the hydrogen plasma cleaned sample increased less than 3% (Figure 29); and sample D with no H<sub>2</sub> plasma yielded from 20% to 70% reduction in PR signal (Figure 33), the surface altered by the metallic substance produced inconsistent results, and the hydrogen plasma cleaned sample generally provided increased  $\Delta R/R$  signals above 215K and decreased signals at 215K or below (Figures 37 - 47). Most of these results were inconsistent with those of Seebauer[28] who observed substantial decreases in PR signal magnitude even at very low

coverages. Since the samples without the  $H_2$  plasma yielded somewhat similar results, it is possible that the carbon contaminants remaining on the surface of these samples allowed  $H_2O$  to physisorb more easily. Buchel and Luth reported a type of condensed water layer was found at high exposures[3]. Also, the Ga rich surface may have allowed the water to dissociate more forming the Ga-OH bonds as reported by Webb and Lichtensteiger[60]. Another possibility is that the n-type samples studied had too great a density of surface states, which the adsorbed  $H_2O$  could not sufficiently alter. So, no significant changes in the water adsorbed spectra would occur. Sample D generally followed the results of Seebauer[28] at lower temperatures. It is unclear why the PR signal actually increased upon water adsorption at temperatures around 240K and above. It can be suggested that the water dissociated more easily at higher temperatures, allowing more chemisorption of the water radicals, which in turn attracted more charge carriers to the surface, resulting in a greater  $\Delta R/R$  signal. The water was tightly bound in some manner to the Ga and As atoms, as supported by the lack of desorption that occurred following reversibility attempts. The water adsorbed pressure also significantly affected the PR signal amplitude, with higher pressures yielding lower spectra as saturation was achieved.

## 6 Conclusions

The electromodulation technique of photoreflectance was successfully used to analyze the surface characteristics of GaAs(100). Its optical, nondestructive capability and sensitive nature to surface phenomena, allowed sample characterization at UHV as low as  $10^{-9}$  torr, and as high as 100 mTorr; and at temperatures from 100K to 500K. Sample cleanliness and water adsorption effects were easily measured throughout these ranges. The ability of PR to operate with precision over such diverse ranges of pressure and temperature is critical to the studies of adsorption, desorption, and reaction of gases on semiconductors, since such interactions are normally quite weak.

A consistent cleaning procedure is essential to ensure reproducible spectra of the clean sample surface. The cleaning procedure of degreasing with trichloroethylene, rinsing with acetone and methanol, then acid etching with  $\text{H}_2\text{SO}_4:\text{H}_2\text{O}_2:\text{H}_2\text{O}$  for fifteen seconds and immediately flushing with deionized water, followed by a low intensity  $\text{H}_2$  plasma etch at 400°C and a five minute anneal at 550°C, produced the best results.

GaAs that was p-type with a carrier concentration of  $2.1 \times 10^{18}$  proved to be the best for quantitative  $\text{H}_2\text{O}$  studies at the  $E_0$  critical point. Water adsorbed much faster than it desorbed, and desorption above  $10^{-4}$  torr could not be detected. The PR signal increased in amplitude at temperatures above 240K, and usually decreased below 240K depending on the adsorbing pressure. This indicates that surface coverage increased at higher temperatures and decreased at lower temperatures.

## References

- [1] *Process Challenges in Compound Semiconductors*, National Materials Advisory Board, NMAB-446, (National Academy Press, Washington D.C., 1988).
- [2] W. Mokwa, D. Kohl and G. Heiland, *Surf. Sci.* **139**, 98 (1984).
- [3] M. Buchel and H. Luth, *Surf. Sci.* **87**, 285 (1979).
- [4] L. Peters, L. Phaneuf, L.W. Kapitan, and W.M. Theis, *J. Appl. Phys.* **62**, 4558 (1987).
- [5] H. Shen, S.H. Pan, Z. Hang, J. Leng, and F. Pollak, *Appl. Phys. Lett.* **53**, 1080 (1988).
- [6] E.Y. Wang, W.A. Albers, Jr., and C.E. Bleil, in *II-VI Semiconducting Compounds*, 1967 International Conference, edited by D.G. Thomas, (Benjamin, New York, 1967), p. 136.
- [7] J.L. Shay, *Phys. Rev. B* **2**, 803 (1970).
- [8] D.E. Aspnes and A.A. Studna, *Phys. Rev. B* **7**, 4605 (1973).
- [9] N. Bottka, D.K. Gaskill, R.S. Sillmon, R. Heny, and R. Glosser, *J. Electron. Mater.* **17**, 161 (1988).
- [10] M. Sydor, W. Mitchel, T.W. Haas, J. Angelo, and M. Yen, *J. Appl. Phys.* **66**, 156 (1989).
- [11] M. Sydor, J. Angelo, J.J. Wilson, *Phys. Rev. B* **40**, 8473 (1989).
- [12] C.D. Thurmond, *J. Electrochem. Soc.* **122**, 1133 (1975).
- [13] R.E. Nahory and J.L. Shay, *Phys. Rev. Letters* **21**, 1569 (1968).
- [14] Y. Hamakawa, and M.S. Germano, and P. Handler, *Phys. Rev.* **167**, 709 (1968).
- [15] F. Cerdeira and M. Cardona, *Solid State Commun.* **7**, 879 (1969).

- [16] O.J. Glembocki, B.V. Shanabrook, N. Bottka, W.T. Beard and J. Comas, *SPIE* **524**, 86 (1985).
- [17] H. Shen, P. Parayanthal, F.H. Pollak, M. Tomkiewicz, T.J. Drummond, and J.N. Schulman, *Appl. Phys. Lett.* **48**, 653 (1986).
- [18] O.J. Glembocki, B.V. Shanabrook, N. Bottka, W.T. Beard, and J. Comas, *Appl. Phys. Lett.* **46**, 970 (1985).
- [19] G. Ji, U.K. Reddy, D. Huang, T.S. Henderson, and H. Mardoc, *Superlattices and Microstructures* **3**, 539 (1987).
- [20] U.K. Reddy, G. Ji, D. Huang, G. Munns, and H. Morkoc, *Appl. Phys. Lett.* **50**, 1748 (1987).
- [21] X.C. Shen, H. Shen, P. Parayanthal, and F.H. Pollak, *Superlattices and Microstructures* **2**, 513 (1986).
- [22] P.M. Amirtharaj, J.H. Dinar, J.J. Kennedy, P.R. Boyd, and O.J. Glembocki, *J. Vac. Sci. Technol.* **A4**, 2028 (1986).
- [23] P.M. Amirtharaj, J.J. Kennedy, and P.R. Boyd, *J. Vac. Sci. Technol.* **A5**, 3184 (1987).
- [24] P.M. Amirtharaj and M.S. Odell, *J. Vac. Sci. Technol.* **A6**, 1421 (1988).
- [25] A. Giordana, R. Glosser, J.G. Pellegrino, S. Qadri, and E.D. Richmond, *Materials Letters* **8**, 64 (1989).
- [26] F.H. Pollak and H. Shen, *J. Electron. Mater.* **19**, 399 (1990).
- [27] P.H. Williams and I.T. McGovern, in *The Chemical Physics of Solid Surfaces and Heterogeneous Catalysis* **3**, edited by D.A. King and O.P. Woodruff (New York, Elsevier, 1984) p. 267.
- [28] E.G. Seebauer, *J. Vac. Sci. Technol.* **A7**, 3279 (1989).
- [29] E.G. Seebauer, *J. Appl. Phys.* **66**, 4963 (1989).
- [30] S. Sugata, A. Takamori, N. Takado, K. Asakawa, I. Miyauchi, and H. Hashimoto, *J. Vac. Sci. Technol.* **B6**, 1087 (1988).

- [31] A.Y. Cho and J.R. Arthur, *Progress in Solid State Chemistry* **10**, 157 (1975).
- [32] A. Saletes, J. Massies, and J.P. Contour, *Japan. J. Appl. Phys.* **25**, 48 (1986).
- [33] J.P. Contour, J. Massies, and A. Saletes, *Japan. J. Appl. Phys.* **24**, 563 (1985).
- [34] J.P. Contour, J. Massies, and A. Saletes, *Appl. Phys.* **A38**, 45 (1985).
- [35] J. Massies, and J.P. Contour, *J. Appl. Phys.* **58**, 806 (1985).
- [36] A. Ismail, J.M. Palau, and L. Lassabatere, *Applications of Surface Science* **17**, 363 (1984).
- [37] G. Laurence, F. Simondet, and P. Saget, *Appl. Phys.* **19**, 63 (1979).
- [38] J. Szuber, *Acta Physica Polonica*, **A69**, 531 (1986).
- [39] R.P.H. Chang, C.C. Chang, and S. Darack, *J. Vac. Sci. Technol.* **20**, 45 (1982).
- [40] J.P. Contour, J. Massies, and A. Saletes, *J. Vac. Sci. Technol.* **B5**, 730 (1987).
- [41] M. Hirose, S. Yokoyama, and Y. Yamakage, *J. Vac. Sci. Technol.* **B3**, 1445 (1985).
- [42] S. Ingrey, *J. Vac. Sci. Technol.* **A4**, 984 (1986).
- [43] J.G. Gay and L.T. Klauder, Jr., *Phys. Rev.* **172**, 811 (1968).
- [44] N.G. Nilsson, *Solid State Commun.* **7**, 479 (1969).
- [45] W.A. Alers, *Phys. Rev. Lett.* **23**, 410 (1969).
- [46] J.L. Shay and R.E. Nahory, *Solid State Commun.* **7**, 945 (1969).
- [47] Q.H.F. Vrehen, *J. Phys. Chem. Solids* **29**, 129 (1968).
- [48] D.E. Aspnes, *Solid State Commun.* **8**, 267 (1970).
- [49] S.P. Sheu, in *Photorefectance Studies of Adsorption on GaAs(100)*, Univ. of Illinois (Urbana, IL 1990), p. 14.



- [50] D.E. Aspnes, in *Handbook on Semiconductors*, **2**, edited by M. Balkanski, (North-Holland Publishing Co., New York, 1980).
- [51] J.R. Chelikowsky and M.L. Conen, *Phys. Rev. B* **14**, 556 (1976).
- [52] D.E. Aspnes, *Surf. Sci.* **37**, 418 (1973).
- [53] B.O. Seraphin and N. Bottka, *Phys. Rev. Lett.* **145**, 628 (1966).
- [54] R. Enderlein and R. Keiper, *Phys. State Sol.* **19**, 673 (1967).
- [55] D.E. Aspnes, *Phys. Rev. B* **10**, 4228 (1974).
- [56] D.E. Aspnes, *Phys. Rev.* **153**, 972 (1967).
- [57] D.E. Aspnes and J.E. Rowe, *Phys. Rev. Lett.* **27**, 188 (1971).
- [58] *Guide to the Data Acquisition and Control Adaptor Programming Supports*, IBM Personal Computer Software, 1984.
- [59] G. Laurence, F. Simondet, and P. Saget, *Appl. Phys.* **19**, 63 (1979).
- [60] C. Webb and M. Lichtensteiger, *Vac. Sci. Technol.* **21**, 659 (1982).

## Appendix 1: Program 1 listing

```

10  'PROGRAM FOR STARTING MONOCHROMATOR REPRODUCIBLY.
20  'REVISED 8/10/90
30  CLS
40  SPEED=.05 'UNITS OF NM/SEC
50  SCANSTEP=R 'USE 2 FOR FULL STEPS, 4 FOR HALF STEPS.
60  START=900 'THESE ARE DUMMY WAVELENGTHS.
70  FINISH=70
80  ' Define segment that the 5011 is located in.
90  DEF SEG = &HD000
100 '
110 ' Make sure the motor is not moving
120 '
130 POKE 1020,ASC("S ")
140 POKE 1021,ASC("T")
150 POKE 1023,ASC("A")
160 STEPSTART=START*SCANSTEP 'change nm to steps; 1nm =2*SCANSTEP
    steps.
170 IF STEPSTART<256 THEN GOTO 260
180 A$=HEX$(STEPSTART)
190 B$=LEFT$(A$,1)
200 C$=RIGHT$(A$,2)
210 B$="&H"+B$
220 C$="&H"+C$
230 B=VAL(B$)
240 C=VAL(C$)
250 GOTO 280
260 B=0
270 C=STEPSTART
280 POKE 789,C          'Set position of motor A
290 POKE 790,B
300 POKE 791,&H0
310 '
320 'example: Load SPEED register of both motors wt 20 for a speed of:
330 '          .0001 x 20 = .0020 sec/step => 500 steps/sec=500(2.5A)/s '
340 SPEEDCALC$=HEX$(INT(10000/SPEED*SCANSTEP))'Max range of
    HEX$=65535
350 IF LEN(SPEEDCALC$)=4 THEN SCALC1$=LEFT$(SPEEDCALC$,2) ELSE
    SCALC1$=LEFT$(SPEEDCALC$,1)

```

```

360 SCALC2$=RIGHT$(SPEEDCALC$,2)
370 SCALC1$="&H"+SCALC1$
380 SCALC2$="&H"+SCALC2$
390 SCALC1=VAL(SCALC1$)
400 SCALC2=VAL(SCALC2$)
410 POKE 768,SCALC2'Set motor speed. Second part of hex conversion appears
    here.
420 POKE 769,SCALC1'First half appears here, e.g.,2710 becomes &H10 in address
430 '          768 and &H27 in address 769. Speed is "per motion" of the
440 '          motor. The period is the same regardless of whether half
450 '          steps or full steps are used.
460 '
470 ' Load DISTANCE registers of A motor in nm '
490 STEPFIN=FINISH*SCANSTEP 'Convert to step units
500 IF STEPFIN<256 GOTO 590
510 AA$=HEX$(STEPFIN)
520 BB$=LEFT$(AA$,1)
530 CC$=RIGHT$(AA$,2)
540 BB$="&H"+BB$
550 CC$="&H"+CC$
560 BB=VAL(BB$)
570 CC=VAL(CC$)
580 GOTO 610
590 BB=0
600 CC=STEPFIN
610 POKE 781,CC
620 POKE 782,BB
630 POKE 783,0
640 '
650 ' THE EFSS AND STPFSS REGISTERS MATTER ONLY AT VERY HIGH
    SCAN RATES.
660 ' Set the EFSS registers of both motors to 100. This will set the starting
670 speed of the motors to  $100 \times .0001 = .01$  sec/step => 100 steps/sec
680 '
690 POKE 794,100 'Set EFSS of motor A
700 POKE 795,0
710 POKE 796,0
720 ' Set the STPFSS register of the motor to 50. This will set the ramp
730 ' length to 50 steps.
740 '

```

```

750 POKE 798,50          'Set ramp length of motor A
760 '
780 '
790 SCANHOLD$=HEX$(CINT(SCANSTEP/2-1))
800 SCANHOLD$="&H"+SCANHOLD$
810 SCANHOLD=VAL(SCANHOLD$)
820 POKE 801,SCANHOLD 'Set stepping mode; 1=half step, 0=full step.
830 INPUT "Press return to begin moving.  ";DUMMY
840 PRINT "Moving... press F1 to stop."
850 POKE 1020,ASC("M") 'BEGIN MONOCHROMATOR MOTION
860 POKE 1021,ASC("A")
870 POKE 1023,ASC("A")
880 KEY(1) ON
890 ON KEY(1) GOSUB 930 'for stopping the motion of the motor'
900 FOR I=1 TO 100000! 'THIS LOOP MARKS TIME WHILE THE
    MONOCHROMATOR SCANS.
910 J=I+1
920 NEXT I
930 KEY (1) OFF
940 DEF SEG=&HD000
950 POKE 1020, ASC("S")
960 POKE 1021, ASC("T")
970 POKE 1023, ASC("A")
980 IF PEEK (1023) = ASC ("A") GOTO 980
990 PRINT "SCANNING ABORTED."
1000 END

```

## Appendix 2: Program 2 listing

```
10  'PROGRAM FOR TAKING PHOTOREFLECTANCE DATA AT A SCAN RATE
    =2.0 NM/SEC.
20  CLS
30  INPUT "Input the output filename (path:file.pm)";FILE$
40  PRINT
50  INPUT "Input Signal Level setting on PAR lock-in";SENSI
60  PRINT
80  AMP=1
90  Q=0
100 PRINT "The default scan speed is 1.0 nm/sec using half steps.  If you want"
110 PRINT "a different scan speed or want to use full steps, type 1."
120 INPUT "Press return to use the defaults.      ";Q
130 SPEED=1!
140 SCANSTEP=4 'Use 2 for full steps, 4 for half steps.
150 IF Q=0 GOTO 190
160 PRINT "Type desired scan speed (nm/sec).  Use speed > .0763 nm/sec for full"
170 INPUT "steps, .0382 nm/sec for half steps.  ";SPEED
180 INPUT "Type 4 if you want half steps; type 2 for full steps.  ";SCANSTEP
190 PRINT
210 PRINT "Input the starting and ending wavelengths (nm), with the"
220 PRINT "starting > finishing (scanning down)."
```

```

400 '
410 ' Set position of motor A in nm
420 IF START > 600 THEN CALI=1 'BLAZE-750nm WAVELENGTH CALI-
    BRATION
430     ELSE CALI=2 'BLAZE-400nm WAVELENGTH CALIBRATION'
440 IF START <100 OR START >1080 GOTO 2540
450 STEPSTART=START*SCANSTEP 'change nm to steps; 1nm =2*SCANSTEP
    steps.
460 IF STEPSTART<256 THEN GOTO 550
470 A$=HEX$(STEPSTART)
480 B$=LEFT$(A$,1)
490 C$=RIGHT$(A$,2)
500 B$="&H"+B$
510 C$="&H"+C$
520 B=VAL(B$)
530 C=VAL(C$)
540 GOTO 570
550 B=0
560 C=STEPSTART
570 POKE 789,C 'Set position of motor A
580 POKE 790,B
590 POKE 791,&H0
600 '
610 'example: Load SPEED register of both motors wt 20 for a speed of:
620 ' .0001 × 20 = .0020 sec/step => 500 steps/sec=500(2.5A)/s '
630 SPEEDCALC$=HEX$(INT(10000/SPEED*SCANSTEP)))'Max range of
    HEX$=65535
640 IF LEN(SPEEDCALC$)=4 THEN SCALC1$=LEFT$(SPEEDCALC$,2) ELSE
    SCALC1$=LEFT$(SPEEDCALC$,1)
650 SCALC2$=RIGHT$(SPEEDCALC$,2)
660 SCALC1$="&H"+SCALC1$
670 SCALC2$="&H"+SCALC2$
680 SCALC1=VAL(SCALC1$)
690 SCALC2=VAL(SCALC2$)
700 POKE 768,SCALC2'Set motor speed. Second part of hex conversion appears
    here.
710 POKE 769,SCALC1'First half appears here, e.g.,2710 becomes &H10 in address
720 ' 768 and &H27 in address 769. Speed is "per motion" of the
730 ' motor. The period is the same regardless of whether half
740 ' steps or full steps are used.

```

```

750 '
760 ' Load DISTANCE registers of A motor in nm '
770 IF FINISH <100 OR FINISH > 1080 GOTO 2540
780 STEPFIN=FINISH*SCANSTEP 'Convert to step units
790 IF STEPFIN<256 GOTO 590
800 AA$=HEX$(STEPFIN)
810 BB$=LEFT$(AA$,1)
820 CC$=RIGHT$(AA$,2)
830 BB$="&H"+BB$
840 CC$="&H"+CC$
850 BB=VAL(BB$)
860 CC=VAL(CC$)
870 GOTO 900
880 BB=0
890 CC=STEPFIN
900 POKE 781,CC
910 POKE 782,BB
920 POKE 783,0
930 '
940 ' THE EFSS AND STPFSS REGISTERS MATTER ONLY AT VERY HIGH
SCAN RATES.
950 ' Set the EFSS registers of both motors to 100. This will set the starting
960 speed of the motors to  $100 \times .0001 = .01$  sec/step => 100 steps/sec
970 '
980 POKE 794,100 'Set EFSS of motor A
990 POKE 795,0
1000 POKE 796,0
1010 ' Set the STPFSS register of the motor to 50. This will set the ramp
1020 ' length to 50 steps.
1030 '
1040 POKE 798,50 'Set ramp length of motor A
1050 '
1070 '
1080 SCANHOLD$=HEX$(CINT(SCANSTEP/2-1))
1090 SCANHOLD$="&H"+SCANHOLD$
1100 SCANHOLD=VAL(SCANHOLD$)
1110 POKE 801,SCANHOLD 'Set stepping mode; 1=half step, 0=full step.
1190 '
1200 THE FOLLOWING PROGRAM IS FOR IBM DATA ACQUISITION BOARD
1210 '

```

```

1220 '
1230 'LOAD HEADER FOR IBM DATA ACQUISITION CARD
1240 '
1250 '
1260 'NAME: Data Adquisition And Control (DAAC)
1270 '      HEADER for BASICA
1280 '
1290 'FILE NAME: DACHDR.BAS
1300 '
1310 'DOS DEVICE NAME: DAAC1
1320 '
1330 'RESERVED FUNCTION NAMES:
1340 '      AINM, AINS, AINSC, AOUM, AOUS,
1350 '      BINM, BINS, BITINS, BITOUS, BOUM, BOUS,
1360 '      CINM, CINS, CSET, DELAY
1370 'RESERVED DEF SEG VALUE NAME: DSEG
1380 '
1390 'NAMES DEFINED AND USED BY HEADER:
1400 '      ADAPT%, AI, cOUNT, FOUND%,
1410 '      HNAME$, SG%, STAT%
1420 '
1430 '
1440 'When using the BASICA Interpreter, this header
1450 'must be executed before any function calls are
1460 'made that access the DAAC adapter. It initializes
1470 'a number of variables for each function call. These
1480 'variables are reserved and should not be used except
1490 'to access the DAAC adapter. This routine also does a
1500 'DEF SEG to the segment where the DAAC Device Driver
1510 '(DAC.COM) is loaded. If you execute a DEF SEG to
1520 'access other hardware, you must DEF SEG to the segment
1530 'of the DAAC Device Driver before any subsequent
1540 'calls to access the DAAC adapter.
1550 '
1560 '
1570 FOUND% = 0
1580 SG% = &H2E
1590 'Start searching the interrupt vectors until you find
1600 'one that points to the DAAC device driver.
1610 'Do a DEF SEG to that segment.

```



```

1620 WHILE ((SG% <= &H3E) AND (FOUND% = 0))
1630     DEF SEG = 0
1640     DSEG = PEEK(SG%) + PEEK(SG% + 1) * 256
1650     DEF SEG = DSEG
1660     HNAME$=""
1670     FOR AI=10 TO 17
1680         HNAME$ = HNAME$ + CHR$(PEEK(AI))
1690     NEXT AI
1700     IF HNAME$ = "DAAC  " AND PEEK(18) + PEEK(19) <> 0 THEN
FOUND% = 1
1710         SG% = SG% + 4
1720     WEND
1730 IF FOUND% = 0 THEN PRINT "ERROR: DEVICE DRIVER DAC.COM NOT
FOUND" : END
1740 'Now initialize all function name variables for calls
1750 'to access the device driver.
1760 AINM      = PEEK(&H13) * 256 + PEEK(&H12)
1770 AINS      = PEEK(&H15) * 256 + PEEK(&H14)
1780 AINSC     = PEEK(&H17) * 256 + PEEK(&H16)
1790 AOUM      = PEEK(&H19) * 256 + PEEK(&H18)
1800 AOUS      = PEEK(&H1B) * 256 + PEEK(&H1A)
1810 BINM      = PEEK(&H1D) * 256 + PEEK(&H1C)
1820 BINS      = PEEK(&H1F) * 256 + PEEK(&H1E)
1830 BITINS    = PEEK(&H21) * 256 + PEEK(&H20)
1840 BITOUS    = PEEK(&H23) * 256 + PEEK(&H22)
1850 BOUM      = PEEK(&H25) * 256 + PEEK(&H24)
1860 BOUS      = PEEK(&H27) * 256 + PEEK(&H26)
1870 CINM      = PEEK(&H29) * 256 + PEEK(&H28)
1880 CINS      = PEEK(&H2B) * 256 + PEEK(&H2A)
1890 CSET      = PEEK(&H2D) * 256 + PEEK(&H2C)
1900 DELAY     = PEEK(&H2F) * 256 + PEEK(&H2E)
1910 'Finally, execute any call to re-initialize the
1920 'device driver from any former invocation of BASIC.
1930 ADAPT% = 0
1940 COUNT = 1
1950 STAT% = 0
1960 CALL DELAY (ADAPT%, COUNT, STAT%)
1970 '
1980 'End of DAAC BASICA Header
1990 '

```

```

2000 'initialize global variables used in all sections
2010 'adapter number 0
2020 ADAPT% = 0
2030 'use on-board analog I/O device
2040 DEVICE% = 9
2100 '*****
2110 'this program takes samples from
2120 'channel 3 of the on-board analog input device
2130 'and stores them in a one-dimensional array
2140 '
2150 'assign values to the arguments of AINM
2160 CHANNEL% = 3
2170 CTRL% = 0
2180 MODE% = 0
2190 STOR% = 0
2200 STAT% = 0
2210 '
2220 INPUT "Press return to begin moving. ";DUMMY
2230 PRINT
2240 PRINT "Scanning... press F1 to abort."
2250 DEF SEG = &HD000
2260 POKE 1020,ASC("M")
2270 POKE 1021,ASC("A")
2280 POKE 1023,ASC("A")
2290 DEF SEG = DSEG
2300 KEY(1) ON
2310 ON KEY(1) GOSUB 2570 'for stopping the motion of the motor'
2320 INITTIME = TIMER
2330 FOR I= 1 TO NUMPTS
2340 CALL AINS (ADAPT%, DEVICE%, CHANNEL%, CTRL%, RAWDATA%,
STAT%)
2350 'if status non-zero, set line and go to error handler
2360 IF STAT% <> 0 THEN LNUM% = 2360 : GOTO 2500
2370 RDATA%(I)=RAWDATA%
2380 T(I)=TIMER-INITTIME
2390 CALL DELAY(ADAPT%,SAMPERIOD,STAT%)
2400 IF STAT% <> 0 THEN LNUM% = 2400 : GOTO 2500
2410 NEXT I
2415 BEEP
2420 PRINT

```

```

2430 PRINT "SCAN COMPLETE."
2440 '
2450 GOTO 2650
2460 '
2470 '***** Error handler begins here *****
2480 '
2490 'on status error, print message, error number, and exit
2500 PRINT "Execution Error # ";STAT%; "in line number "; LNUM%
2510 PRINT "Program Terminated"
2520 end
2530 '
2540 PRINT "EXCEED UPPER OR LOWER LIMIT , 100-1080 NM"
2550 GOTO 210
2560 '
2570 KEY (1) OFF
2580 DEF SEG=&HD000
2590 POKE 1020, ASC("S")
2600 POKE 1021, ASC("T")
2610 POKE 1023, ASC("A")
2620 IF PEEK (1023) = ASC ("A") GOTO 2620
2630 PRINT "SCANNING ABORTED."
2640 GOTO 2750
2650 'LOOP FOR CONVERTING DIGITAL VALUE TO MILLIVOLT'
2660 OPEN FILE$ FOR OUTPUT AS #1
2670 FOR I=1 TO NUMPTS
2680 VOLT=(20/4096*RDAT% (I)-10)*.000016/SENSI*AMP
2690 WAVE=START-T(I)*SPEED
2700 IF CALI=1 THEN WAVE=1.00265*WAVE-.876 'BLAZE-750 CALABRATION
2710 ELSE WAVE=1.00121*WAVE+6.31 'BLAZE-400 CALABRATION
2720 ENG=1239.5/WAVE
2730 PRINT#1,USING"##.#####^" ";ENG,VOLT
2740 NEXT I
2742 BEEP
2744 BEEP
2750 CLOSE#1
2760 END

```